

**Processing-Microstructure-Property Relationship in the High Strength Dual-Phase Steels**

by

**Yingjie Wu**

Bachelor of Science, Nanchang Hangkong University, China, 2014

Master of Science, University of Pittsburgh, 2017

Submitted to the Graduate Faculty of the  
Swanson School of Engineering in partial fulfillment  
of the requirements for the degree of  
Doctor of Philosophy

University of Pittsburgh

2021

UNIVERSITY OF PITTSBURGH  
SWANSON SCHOOL OF ENGINEERING

This dissertation was presented

by

**Yingjie Wu**

It was defended on

December 2, 2020

and approved by

Scott Mao, Ph.D., Professor, Department of Mechanical Engineering and Materials Science

Patrick Smolinski, Ph.D., Associate Professor, Department of Mechanical Engineering and  
Materials Science

John Oyler, Ph.D., Associate Professor, Department of Civil and Environmental Engineering

Dissertation Director: Anthony J. DeArdo, Ph.D., Professor, Department of Mechanical  
Engineering and Materials Science

Dissertation Co-director: Brian Gleeson, Ph.D., Professor, Department of Mechanical  
Engineering and Materials Science

Copyright © by Yingjie Wu

2021

# **Processing-Microstructure-Property Relationship in the High Strength Dual-Phase Steels**

Yingjie Wu, PhD

University of Pittsburgh, 2021

The goal of this thesis was to study how to further increase the ultimate tensile strength (UTS) of dual-phase (DP) steels, while not severely sacrificing global ductility (total elongation (TE)) and local ductility (hole expansion ratio (HER)). Candidate steels with 0.15 wt.% C, 0.04/0.4/0.8 wt.% Al and 0.06/0.12 wt.% V were designed and melted. The pre-annealing conditions studied included two coiling temperatures of 580°C and 677°C and one cold reduction of 60%. Two annealing continuous galvanizing line (CGL) simulations (the conventional standard galvanizing (GI) treatment and a new process called the supercooling process (SC)) were selected for this study. The results indicated that the highest UTS of 1181.4 MPa can be obtained for the steel condition of 0.04 wt.% Al, 0.12 wt.% V, a low coiling temperature of 580°C and the GI anneal with the microstructures characterized by a large amount of fresh martensite, and fine-grained ferrite which itself is strengthened by fine vanadium carbides precipitates.

Three methods, based on electron backscattered diffraction (EBSD) technologies, i.e., the sub-grain, image quality and kernel average misorientation techniques, were used to evaluate the stored energy for DP steels with different pre-annealing conditions. The results indicated that the steels with the combination of low coiling temperature and cold reduction had the highest stored energy, providing more initial driving force for ferrite recrystallization and austenite formation during the subsequent intercritical annealing.

Finally, with the purpose of better understanding improvements in the hole expansion performances of high-strength DP steels, HER values of different steel conditions were determined,

and the defects formed during hole punching and their growth during hole expansion were examined. The results implied that coiling temperatures and CGL simulations played a significant role in influencing HER values. Also, micro-voids or micro-cracks were introduced in the initial hole inner surfaces and sheared edges during hole punching. Punching-induced pre-strains were not uniform, since they varied with the distance from the sheared edges. These damages caused by hole punching later strongly influenced performance during hole expansion. Microstructures beneficial to HER retard the growth of the defects accompanying hole punching, leading to high values of HER.

## Table of Contents

Acknowledgements.....	xxii
List of abbreviations .....	xxiii
1.0 Introduction.....	1
2.0 Background.....	4
2.1 Origin and Need for High Strength Steels in Automobiles.....	4
2.2 Metallurgical Knowledge .....	5
2.2.1 Intercritical Annealing Technology .....	5
2.2.1.1 Ferrite Recrystallization and Austenite Formation in the Two-Phase Region.....	6
2.2.1.2 Austenite Decomposition during Continuous Cooling from the Intercritical Annealing Temperatures.....	9
2.2.1.3 Retained Austenite in the Final Microstructures after CGL.....	11
2.2.2 Chemical Compositions .....	12
2.2.2.1 Carbon.....	13
2.2.2.2 Manganese .....	15
2.2.2.3 Aluminum .....	17
2.2.2.4 Chromium .....	19
2.2.2.5 Vanadium.....	20
2.2.3 Strengthening Mechanisms .....	21
2.2.3.1 Rule of Mixtures (Banded Martensite) .....	22
2.2.3.2 Grain Refinement.....	23

2.2.3.3 Dislocation Strengthening .....	23
2.2.3.4 Precipitation Hardening .....	25
2.3 Other Considerations .....	27
2.3.1 Stored Energy .....	27
2.3.2 Stretch-Flangeability .....	29
3.0 Motivation and Objectives .....	34
4.0 Operating Hypotheses .....	35
5.0 Experimental Procedures .....	36
5.1 Materials and Processing .....	36
5.2 Stored Energy Evaluation .....	40
5.2.1 Material Characterizations .....	40
5.2.2 Vickers Hardness Measurements .....	41
5.2.3 Stored Energy Evaluation Methods with EBSD Technology .....	41
5.3 Austenite Formation Studies with Al Contents .....	45
5.3.1 Annealing Stimulations .....	45
5.3.2 Material Characterizations .....	46
5.4 Microstructure – Property Relationship Study .....	47
5.4.1 Mechanical Testing .....	47
5.5 Stretch-Flangeability Investigation .....	47
5.5.1 Hole Expansion Testing .....	47
5.5.2 Microstructural Observation after Hole Punching .....	49
5.5.3 Local Internal Plastic Strains Study .....	50
5.5.4 Micro-Fracture Mechanism Study .....	52

6.0 Stored Energy Evaluation .....	53
6.1 Results .....	53
6.1.1 The Microstructures of the Starting Conditions.....	53
6.1.2 Microstructural Analysis with EBSD Technology .....	56
6.1.3 Vickers Hardness Measurements .....	60
6.1.4 The Assessment of Stored Energy with Three Methods Based on EBSD Technology.....	61
6.1.4.1 Sub-Grain Method .....	61
6.1.4.2 IQ Method.....	63
6.1.4.3 KAM Method.....	65
6.1.4.4 HAGB Energy .....	66
6.2 Discussion.....	67
6.2.1 The Comparison among Three Stored Energy Assessment Approaches.....	67
6.2.2 The Effects of Pre-Annealing Conditions on Stored Energy .....	71
6.3 Conclusions .....	73
7.0 Austenite Formation Studies with Al Contents .....	75
7.1 Results .....	75
7.1.1 Fe-Fe <sub>3</sub> C Phase Diagram .....	75
7.1.2 CCT Diagram .....	77
7.1.3 Microstructural Observation of Austenite Formation for Candidate DP Steels with Al Contents .....	80
7.1.4 Determination of the Kinetics Model of Intercritically Annealed Austenite Formation.....	86

7.2 Discussion.....	90
7.2.1 Effect of Al Contents on Austenite Formation during Intercritical Annealing....	90
7.3 Conclusions .....	93
8.0 Microstructure - Property Relationship Study .....	95
8.1 Results .....	95
8.1.1 Final Microstructures after Full CGL Simulations <sup>4</sup> .....	95
8.1.2 Tensile Properties.....	103
8.2 Discussion.....	108
8.2.1 Effects of Pre-Annealing Conditions on Ferrite Grain Sizes .....	108
8.2.2 Influences of Pre-Annealing Conditions and Annealing Paths on the Fraction of Hard Constituents.....	109
8.2.3 Consequences of Pre-Annealing Conditions and Annealing Paths on Strength	111
8.2.4 Significance of V Additions and Annealing Path Conditions on Work Hardening Behavior .....	114
8.2.5 Strength - Ductility Considerations of DP Steels.....	118
8.3 Conclusions .....	120
9.0 Investigation of Hole Expansion Performance .....	122
9.1 Results .....	122
9.1.1 Hole Expansion Results .....	122
9.1.2 Microstructure and Damage Evolutions during the Whole HET Process .....	125
9.1.3 The Determination of Punching-Induced Pre-Strains .....	134
9.1.4 Observation of the Deformed Microstructures near the Final Hole Sheared Edges after Incomplete Hole Expansion Tests .....	141

9.2 Discussion.....	143
9.2.1 Effect of Coiling Temperature on HER .....	143
9.2.2 Effect of CGL Simulations on HER .....	144
9.2.3 The Relationship between HER and the Characteristics of Initial Hole Internal Surface.....	145
9.2.4 Crack Initiation Caused by Hole Punching and Micro-Mechanism for Hole Expansion.....	149
9.3 Conclusions .....	151
10.0 Future Work .....	153
Bibliology .....	155

## List of Tables

Table 5.1 Measured chemical compositions (wt. %) and IDs of candidate DP steels.....	36
Table 5.2 Martensite volume fraction (%) of DP steels with different Al levels at distinct IATs in DP steels fully processed in CGL simulations.....	39
Table 6.1 Microstructural features (i.e., ferrite grain size ( $d_{\alpha}$ ), ferrite volume fraction ( $f_{V(\alpha)}$ ) and pearlite volume fraction ( $f_{V(P)}$ ) of hot rolled steels .....	55
Table 6.2 The Vickers hardness (VHN 300) values for the hot band coils (HB) and cold rolled steel sheets (CR).....	61
Table 6.3 $SE_d$ for hot band coils (HB) and cold rolled steels (CR) based on sub-grain method ..	62
Table 6.4 The results of KAM and calculated values of $\rho_{GND}$ and $SE_d$ for both hot rolled and cold rolled steels with pre-annealing conditions based on KAM method .....	65
Table 6.5 $SE_{HAGB}$ for hot band coils (HB) and cold rolled steels (CR) .....	66
Table 7.1 Effects of Al and V on critical temperatures $A_1$ and $A_3$ .....	76
Table 7.2 Effects of Al and V on transformation temperatures of austenite decomposition products from full austenite temperature (FRT = 920°C) at a cooling rate of 15°C s <sup>-1</sup> .....	79
Table 7.3 Equilibrium fraction of austenite ( $f_{\gamma(eq)}$ ) of candidate DP steels with different Al contents .....	88
Table 7.4 Avrami exponent (n), pre-exponential factor ( $k_0$ , s <sup>-1</sup> ) and activation energy (Q, kJ mol <sup>-1</sup> ) of candidate DP steels with different Al contents .....	88
Table 8.1 The microstructural features (ferrite grain sizes ( $d_{(\alpha)}$ ) and volume percentages of ferrite ( $f_{V(\alpha)}$ ), bainite ( $f_{V(B)}$ ) and fresh martensite ( $f_{V(M)}$ )) of GI annealed samples with different pre-annealing conditions. ....	101

Table 8.2 The microstructural features (ferrite grain sizes ( $d_{(\alpha)}$ ) and volume percentages of ferrite ( $f_{V(\alpha)}$ ), bainite ( $f_{V(B)}$ ), fresh martensite ( $f_{V(M)}$ ) and tempered martensite ( $f_{V(TM)}$ ) of SC annealed samples with different pre-annealing conditions. ....	102
Table 8.3 Tensile properties (yield strength (YS), ultimate tensile strength (UTS), yield to tensile strength ratio (YS/UTS), uniform elongation (UE), total elongation (TE), post uniform elongation (Post UE), reduction in area (RA), and product of UTS $\times$ TE) of the fully annealed DP steels with the GI anneal. ....	105
Table 8.4 Tensile properties (yield strength (YS), ultimate tensile strength (UTS), yield to tensile strength ratio (YS/UTS), uniform elongation (UE), total elongation (TE), post uniform elongation (Post UE), reduction in area (RA), and product of UTS $\times$ TE) of the fully annealed DP steels with the SC anneal .....	106
Table 8.5 Calculated strain hardening exponents from the true flow curves of the fully annealed DP steels with both GI and SC anneals.....	118
Table 9.1 Hole expansion ratios of fully annealed DP steels with GI and SC anneals .....	122
Table 9.2 The relationships between KAM values and the distances from the sheared edges in different positions of steel conditions of LLL (0.04Al-0.06V-CT580°C) GI and LLL SC.....	135
Table 9.3 Measured nanohardness values of four tested positions.....	140
Table 9.4 The area fractions of rollover ( $f_{V(R)}$ ), burnished ( $f_{V(B)}$ ) and fracture ( $f_{V(Fx)}$ ) zones in the initial hole surfaces of fully annealed DP steels. ....	148

## List of Figures

Figure 2.1 The effects of IATs on austenite volume fraction, austenite carbon content and martensite start temperature [21]. .....	10
Figure 2.2 The CCT diagram of a C-Mn-Cr-Mo-Si DP steels intercritically annealed at 780°C at a heating rate of 10 °C s <sup>-1</sup> and isothermally held for 120 s. A variety of cooling rates intersecting the CCT diagram determine the transformation temperatures of different austenite decomposition products (i.e., polygonal ferrite (PF), bainitic or acicular ferrite (BF), bainite (B) and martensite (M)) [58]. .....	11
Figure 2.3 Effects of microalloying elements on eutectoid transformation temperatures and eutctoid carbon contents in the Fe-C phase diagram [14]......	16
Figure 2.4 The relationship between the volume percentages of intercritically formed austenite and annealing temperatures of DP steels with different Al levels [20]. .....	17
Figure 2.5 UTS vs TE of DP steels with different Al contents after full CGL simulations [20].	18
Figure 2.6 The CCT diagrams of a 0.15C-2.0Mn-0.006Nb DP steel (a) without Nb and (b) with Nb additions [22]. .....	20
Figure 2.7 The relations between ferrite and (a) strength, (b) uniform elongation (UE), (c) post uniform elongation (Post UE) and (d) TE of steels with or without V addition [78].	21
Figure 2.8 The measured average dislocation density in ferrite as a function of martensite percentage for the as quenched and air cooled DP steels (a) without plastic deformation (b) with 7% cold deformation [86]. .....	24

Figure 2.9 (a) HER vs UTS, (b) HER vs Post UE and (c) HER vs R for a variety of steel grades, data from Sadagopan’s experimental works [124] and BAMPRI unpublished research results. ....	30
Figure 2.10 The schematic illustration of punching process. The formation of (a) rollover zone, (b) burnished zone, (c) fracture zone and (d) shear burr [129]......	31
Figure 5.1 Schematic illustration of thermomechanical processing and heat treatments used in this dissertation .....	37
Figure 5.2 The volume fractions of martensite for steels with different Al levels at distinct IATs. The selection of IAT for each Al content resulting in 80-90 Vol % fresh martensite. ....	39
Figure 5.3 The schematic illustration of austenite formation studies of steels with different Al contents .....	46
Figure 5.4 The schematic process of hole expanding (a) before hole punching, (b) after hole punching, (c) before shearing and (d) after shearing [151]......	49
Figure 5.5 Positions for SEM characterization .....	50
Figure 5.6 Positions for the examination of internal plastic strains casued by hole punching with (a) EBSD-KAM and (b) nanoindentation technologies .....	50
Figure 5.7 The schematic illustration of final hole surface (highlighted in orange color) after hole expanding. ....	52
Figure 6.1 The OM micrographs of the hot rolled steels of steel condtions: (a) LLL HB (0.04Al-0.06V-CT580°C) and (b) LLH HB (0.04Al-0.06V-CT677°C). ....	54
Figure 6.2 Effects of Al and V additons and coiling temperatures on ferrite grain sizes of hot band coils .....	55

Figure 6.3 OM micrographs of cold rolled steel sheets of steel conditions: (a) LLL CR (0.04Al-0.06V-CT580°C) and (b) LLH CR (0.04Al-0.06V-CT677°C). .....	56
Figure 6.4 EBSD mappings: HLL (0.8%Al-0.06%V-CT580°C) HB (a) IQ, (e) IPF, (i)KAM and (m) SE <sub>d</sub> sub-grain; HLL CR (b) IQ, (f) IPF, (j)KAM and (n) SE <sub>d</sub> sub-grain; HLH (0.8%Al-0.06%V-CT677°C) HB (c) IQ, (g) IPF, (k) KAM and (o) SE <sub>d</sub> sub-grain; and HLH CR (d) IQ, (h) IPF, (l) KAM and (p) SE <sub>d</sub> sub-grain.....	59
Figure 6.5 The distributions of reconstructed IQ values for selected steel conditions with hot band coils of (a) HLL (0.8%Al-0.06%V-CT580°C) and (c) HLH (0.8%Al-0.06%V-CT677°C) and cold rolled steel sheets of (b) HLL and (d) HLH.....	64
Figure 6.6 The comparison in stored energy determined by the application of sub-grain (SE <sub>d</sub> (sub-grain)) and KAM (SE <sub>d</sub> (KAM)) methods of (a) hot rolled and (b) cold rolled DP steels with different pre-annealing conditions. ....	69
Figure 6.7 The correlations of (a) VHN vs SE <sub>d</sub> (sub-grain) or VHN vs SE <sub>d</sub> (KAM) and (b) VHN vs SE <sub>tot</sub> (sub-grain) or VHN vs SE <sub>tot</sub> (KAM).....	70
Figure 6.8 The comparison in stored energy determined by the application of sub-grain (SE <sub>d</sub> (sub-grain)) for hot rolled and (b) cold rolled steels with two different coiling temperatures (580°C and 677°C). ....	71
Figure 6.9 The total stored energy evaluation based on the sub-grain method (SE <sub>tot</sub> (sub-grain)) for steels with and without 60% cold reduction. ....	72
Figure 7.1 The Fe-C phase diagrams for candidate DP steels, illustrating effects of Al and V contents on Fe-C phase diagram (critical temperatures were estimated by JMatPro) .	76

Figure 7.2 The CCT diagrams estimated by JMatPro from full austenite region for candiadte DP steels with conditions of (a) LL (0.04Al-0.06V), (b) LH (0.04Al-0.12V), (c) ML (0.4Al-0.06V), (d) MH (0.4Al-0.12V) and (e) HL (0.8Al-0.06V). ..... 78

Figure 7.3 SEM micrographs of steel condition MLL (0.4Al-0.06V-CT580°C) annealed at 770°C for (a) 0s, (b) 5s, (c) 15s, (d) 30s and (e) 60s. Note: ferrite is indicated by F, pearlite by P and martensite by M. Water-quenched martensite represents intercritically formed austenite..... 81

Figure 7.4 SEM micrograph of steel condition MLL (0.4Al-0.06V-CT580°C) annealed at 740°C for 60s. Note: ferrite is indicated by F, pearlite by P and martensite by M. Water-quenched martensite represents intercritically formed austenite. .... 82

Figure 7.5 SEM micrographs of steel condition LLL (0.04Al-0.06V-CT580°C) annealed at 740°C for 0s, illustrating austenite nucleation sites: (a) interfaces between cementite/pearlitic ferrite within pearlite colonies, (b) interface between ferrite/pearlite, (c) recrystallized ferrite/ferrite grain boundaries or triple points and (d) within ferrite grains. Note: ferrite is indicated by F, pearlite by P and martensite by M. Water-quenched martensite represents intercritically formed austenite. .... 83

Figure 7.6 SEM micrograph of steel condition LLL (0.04Al-0.06V-CT580°C) annealed at 740°C for 5s. Note: ferrite is indicated by F, pearlite by P and martensite by M. Water-quenched martensite represents intercritically formed austenite. .... 84

Figure 7.7 The plots of volume fraction of intercritically formed austente as a function of annealing time at different intercritical annealing temperatures for steel conditions of (a) LLL (0.04 wt.% Al), (b) MLL (0.04 wt.% Al), and (c) HLL (0.8 wt.% Al). ..... 85

Figure 7.8 SEM micrographs of steel condition LLL (0.04Al-0.06V-CT580°C) annealed at (a) 740°C, (b) 770°C and (c) 800°C for 3600s. Note: ferrite is indicated by F and martensite by M. Water-quenched martensite represents intercritically formed austenite..... 85

Figure 7.9 SEM micrographs of steel conditions (a) LLL (0.04Al-0.06V-CT580°C), (b) MLL (0.4Al-0.06V-CT580°C) and (c) HLL (0.8Al-0.06V-CT580°C) annealed at 800°C for 3600s. Note: ferrite is indicated by F and martensite by M. Water-quenched martensite represents intercritically formed austenite. .... 86

Figure 7.10 Predictions based on kinetics modeling and experimental results of austenite volume percentages of steel conditions of (a) LLL (0.04 wt.% Al), (b) MLL (0.4 wt.%) and (c) HLL (0.8 wt.% Al). Data points shown as symbols while theory shown as continuous lines. .... 89

Figure 7.11 Schematic illustration of microstructural evolution of candidate DP steels during intercritical annealing..... 91

Figure 8.1 The SEM micrographs of steel conditions LLL (0.04Al-0.06V-CT580°C) with (a) GI anneal and (b) SC anneal and LLH (0.04Al-0.06V-CT677°C) with (c) GI anneal and (d) SC anneal. Note: Ferrite is labeled by F, bainite by B, fresh martensite by M and tempered martensite by TM. .... 96

Figure 8.2 The SEM micrographs of steel conditions LHL (0.04Al-0.12V-CT580°C) with (a) GI anneal and (b) SC anneal and LHH (0.04Al-0.12V-CT677°C) with (c) GI anneal and (d) SC anneal. Note: Ferrite is labeled by F, bainite by B, fresh martensite by M and tempered martensite by TM. .... 99

Figure 8.3 The SEM micrographs of steel conditions MLL (0.4Al-0.06V-CT580°C) with (a) GI anneal and (b) SC anneal and MLH (0.04Al-0.06V-CT677°C) with (c) GI anneal and

(d) SC anneal. Note: Ferrite is labeled by F, bainite by B, fresh martensite by M and tempered martensite by TM. ....	99
Figure 8.4 The SEM micrographs of steel conditions MHL (0.4Al-0.12V-CT580°C) with (a) GI anneal and (b) SC anneal and MHH (0.04Al-0.12V-CT677°C) with (c) GI anneal and (d) SC anneal. Note: Ferrite is labeled by F, bainite by B, fresh martensite by M and tempered martensite by TM. ....	100
Figure 8.5 The SEM micrographs of steel conditions HLL (0.8Al-0.06V-CT580°C) with (a) GI anneal and (b) SC anneal and HLH (0.8Al-0.06V-CT677°C) with (c) GI anneal and (d) SC anneal. Note: Ferrite is labeled by F, bainite by B, fresh martensite by M and tempered martensite by TM. ....	100
Figure 8.6 Engineering vs engineering strain flow curves and comparisons of major tensile properties (yield strength, ultimate tensile strength and total elongation) for fully annealed DP steels with both GI and SC anneals. ....	107
Figure 8.7 Effects of pre-annealing conditions on average ferrite grain sizes of the fully annealed DP steels with both (a) GI and (b) SC anneals. ....	108
Figure 8.8 Effects of pre-annealing conditions and annealing paths on the amount of hard constituents of the fully annealed DP steels with both (a) GI and (b) SC anneals. ...	110
Figure 8.9 The linear relationship between strength and martensite volume fraction based on the data from Davies' work [5] and Tables 8.1 & 8.3. ....	113
Figure 8.10 The relationship between strength and volume percentages of hard constituents of the fully annealed DP steels with GI anneals.....	114
Figure 8.11 $\ln\sigma - \ln\epsilon$ curves of steel conditions of (a) LLL, GI vs LHL, GI and (b) MHL, GI vs MHL, SC.....	116

Figure 8.12 The plots of (a) UE vs  $n_2$  ( $\epsilon=0.05$ ) based on data from Tables 8.3–8.5 and (b) UE vs UTS from the results in Davies’ work [5] and Tables 8.3–8.5..... 119

Figure 8.13 Ultimate tensile strength (UTS) vs total elongation (TS) curves of automotive steels ..... 120

Figure 9.1 The relations between tensile properties and measured HER values of the fully annealed DP steels: (a) YS vs HER, (b) UTS vs HER, (c) UE vs HER, (d) TE vs HER, (e) Post UE vs HER, (f) RA vs HER, (g)  $n_1$  vs HER, and (h)  $n_2$  vs HER..... 124

Figure 9.2 Schematic illustration of hole expansion process consisting of hole punching and hole expanding as well as the microstructure evolutions during the whole HET process. 125

Figure 9.3 The undeformed microstructures of steel condition LLL (0.04Al-0.06V-CT580°C) GI, consisting of ferrite (labeled by F), bainite (B) and fresh martensite (M), with (a) low magnification and (b) high magnification..... 126

Figure 9.4 The undeformed microstructures of steel condition LLL (0.04Al-0.06V-CT580°C) SC, containing ferrite (labeled by F), bainite (B), fresh martensite (M) and tempered martensite (TM), with (a) low magnification and (b) high magnification..... 127

Figure 9.5 (a) The observation direction of (b) the initial hole surface of steel condition LLL (0.04Al-0.06V-CT580°C) GI, in the wake of hole punching, with cracks and shearing dimples found in (c) burnished zone and (d), (e) fracture zone. .... 128

Figure 9.6 (a) The observation direction of (b) the initial hole surface of steel condition LLL (0.04Al-0.06V-CT580°C) SC, in the wake of hole punching, with cracks and shearing dimples found in (c) burnished zone and (d), (e) fracture zone. .... 128

Figure 9.7 (a) The sheared edge and shear affected zone (SAZ) of steel condition LLL (0.04Al-0.06V-CT580°C) GI, after hole punching, with miro-voids or micro-cracks found in (b) burnished and fracture transition zone, (c), (d) fracutre zone, and (e) shear burr..... 130

Figure 9.8 (a) The sheared edge and shear affected zone (SAZ) of steel condition LLL (0.04Al-0.06V-CT580°C) SC, after hole punching, with miro-voids or micro-cracks found in (b) rollover zone, (d) burnished and fracutre transition zone, (e), (f) fracutre zone and (h) shear burr as well as (c), (g) the EDX analyses of cracks in (b) and (f), respectively. .... 131

Figure 9.9 The OM micrographs of final holes of steel conditons of (a) LLL (0.04Al-0.06V-CT580°C) GI and (c) LLL SC as well as (b), (d) the closer observations of thorough-thickness cracks in (a) and (c), respectively. .... 132

Figure 9.10 (a) The sheared edge and shear affected zone (SAZ) of steel condition LLL (0.04Al-0.06V-CT580°C) GI, in the wake of hole expansion, with voids or cracks found in (b), (c) and (d) different areas of the sheared edge. .... 133

Figure 9.11 (a) The sheared edge and shear affected zone (SAZ) of steel condition LLL (0.04Al-0.06V-CT580°C) SC, in the wake of hole expansion, with voids or cracks found in (b), (c) and (d) different areas of the sheared edge as well as (e) the closer observation of a crack in (d). .... 133

Figure 9.12 The relationships between KAM and the distance from the sheared edge of steel conditions of (a) LLL (0.04Al-0.06V-CT580°C) GI and (b) LLL SC, and the relations of the calculated  $\varepsilon_{eq}$  and the distance from the sheared edge of steel conditions of (c) LLL (0.04Al-0.06V-CT580°C) GI and (b) LLL SC. .... 136

Figure 9.13 (a) The initial hole sheared edge and shear affected zone (SAZ) of steel condition LLL (0.04Al-0.06V-CT580°C) GI, after hole punching, with nanoindents in Positions (b) A, (c) B, (d) C and (e) D. ....	138
Figure 9.14 (a) The initial hole sheared edge and shear affected zone (SAZ) of steel condition LLL (0.04Al-0.06V-CT580°C) SC, after hole punching, with nanoindents in Positions (b) A, (c) B, (d) C and (e) D. ....	138
Figure 9.15 The final hole surfaces of steel condition MHL (0.4Al-0.12V-CT580°C) SC with the HER values of (a) 0%, (b) (c) 5%, (d) (e) 10%, (f) (g) (h) 15% and (i) (j) (k) 25%..	142
Figure 9.16 The relationships between HER results and ferrite grain sizes ( $d_\alpha$ ) of steel conditions of LLL (0.04Al-0.06V-CT580°C) and LLH (0.04Al-0.06V-CT677°C) with both GI and SC anneals.....	144
Figure 9.17 The initial hole surfaces of steel conditions of (a) LLL GI and (b) LLL SC .....	146
Figure 9.18 The relationship between HER and the characteristics of initial hole surface .....	149
Figure 9.19 The schematic illustration of the micro-fracture mechanism in terms of hole expansion for fully annealed DP steels. (a) Incipient cracks or voids caused by hole punching, (b) crack propagation or void growth by void enlargement and (c) the major crack crossing section of the tested sample.....	150

## Acknowledgements

First and foremost, the heartfelt thanks go to my dissertation advisor, Prof. Anthony J. DeArdo, for his continuous advice, patience, guidance, encouragement and reassurance throughout the duration of this project.

Secondly, I would like to express my gratitude to the rest of my PhD dissertation committee members, Prof. Brian Gleeson, Prof. Scott Mao, Prof. Patrick Smolinski and Prof. John Oyler, for their insightful comments and suggestions on my dissertation.

In particular, I am grateful to Mr. Juha Uusitalo from University of OULU for supervising the experimental portion, especially the Gleeble CGL simulations for this project. Also, I wish to give a special thank you to my fellow labmates in BAMPRI: Dr. Mingjian Hua, Mrs. Qiongshu Wang, Dr. Bing Ma, Dr. Yu Gong, Junyu Duan, Petch Janbanjong, Aaron Stein, Rami Almatani and Xinchu Feng for invaluable assistance with facilities training and sample preparations.

I also want to thank Drs. Dennis Haezebrouck & Todd Link and the United States Steel Corporation Research and Technology Center, Munhall, PA, for their generous support including providing helpful discussions, lab heats and other in-kind contributions.

Last but not least, I want to extend my thanks to my family for endless love and unwavering support throughout my life.

## List of abbreviations

Abbreviations	Meaning
AHSS	Advanced high strength steel
AKDQ	Aluminum killed drawing quality
BH	Bake hardening
CGL	Continuous galvanizing line
CR	Cold rolling
CT	Coiling temperature
DP	Dual phase
DSC	Differential scanning calorimetry
EBS	Electron backscatter diffraction
EDM	Electric discharge machining
EDX	Energy dispersive spectroscopy
FRT	Finish rolling temperature
GI	Standard galvanizing
GND	Geometrically necessary dislocation
HAGB	High angle grain boundary
HB	Hot band coil
HER	Hole expansion ratio
HSLA	High strength low alloy
IAT	Intercritical annealing temperature

Abbreviations	Meaning
IF	Interstitial free
IPF	Inverse pole figure
IQ	Image quality
JMA	Johnson-Mehl-Avrami
JMAK	Johnson-Mehl-Avrami with Kolmogorov modification
KAM	Kernel average misorientation
LAGB	Low angle grain boundary
LEDS	Low energy dislocation structure
ND	Normal direction
OM	Optical microscopy
Post UE	Post uniform elongation
Q&P	Quench and partitioning
RA	Reduction in area
RD	Rolling direction
SAZ	Sheared affected zone
SC	Supercooling process
SE	Stored energy
SEM	Scanning electron microscopy
SSD	Statistically stored dislocation
TD	Transverse direction
TE	Total elongation
TMP	Thermomechanical processing

---

Abbreviations	Meaning
TRIP	Transformation induced plasticity
TWIP	Twinning induced plasticity
UE	Uniform elongation
UTS	Ultimate tensile strength
WQRT	Water quench to room temperature
YPE	Yield point elongation
YS	Yield strength
YS/UTS	Yield to tensile strength ratio

---

## 1.0 Introduction

Advanced high-strength steels (AHSSs) have gained rapidly growing attention in the automotive industry, since they are the optimum choice of manufacturing vehicle body structures [1,2]. AHSSs share a good combination of ultra-high strength and superior formability/ ductility, favoring passenger safety, mass reduction and greenhouse gas emissions reduction. For example, in the case of weight-saving, the application of AHSSs, with much higher strength, allows for reduced gage components to replace the earlier versions made from lower strength carbon or conventional high-strength low alloy (HSLA) steels, while maintaining the same or improved mechanical properties [3]. The strength-formability-crashworthiness balance of vehicles provide an intense driving force for the numerous AHSS development programs carried out by metallurgists and materials scientists. The innovations in both microstructures and mechanical properties of AHSSs enable automakers and parts manufacturers to use less materials, achieving the goal of automotive weight reduction.

Dual-phase (DP) steels represents the metallurgical breakthrough in the AHSS family, since they were the first, among other alloy systems, to be employed for the purpose of vehicle weight lightening [4]. DP steels are characterized by a ferrite-martensite microstructure [5–12]. In order to obtain this two-phase mixture, effects of alloying or microalloying elements were assessed and some basic understanding were established, i.e., Mn increases austenite hardenability and solid-solution strengthening [13–15], Cr and Mo suppress pearlite and bainite formation [16–18], Si and Al promote ferrite transformation [19–21], and Ti, Nb and V serve to promote microstructure refinement and precipitation hardening [5,22–24]. In addition to ferrite and martensite, pearlite, upper bainite, cementite, retained austenite or tempered martensite in the final

microstructures of DP steels have been also reported in other studies [9,20,25–29]. Also, the mechanical properties of DP steels have been shown to exhibit as follows, continuous yielding, low yield strength (YS), low yield to tensile strength ratio (YS/UTS), high ultimate tensile strength (UTS), high initial strain hardening rate, high fatigue resistance and superior ductility [4,23,30–34].

Since the 1970s, numerous studies have been conducted on the approaches of producing thinner high-strength DP steels. Japanese researchers [35,36] first developed continuous annealing and later continuous galvanizing lines (CGL) for efficiently and economically producing DP steels in industries. In the 1990s, DP 590 steels (DP steels with a UTS of 590 MPa) were established [21], while automakers still searched for higher strength DP steels to enable more weight reduction, at the same time keeping a good ductility or formability (both total elongation (TE) and shear-edge ductility). The so-called DP 590 steels were followed by the stronger steels DP 780 and DP 980 steels [37,38]. These improvements were achieved based on the results of research into the physical and mechanical metallurgy of these steels. It was found that different strengthening mechanisms contribute to increasing the strength of DP steels. From Davies' early studies [5–8], it was concluded that the microstructure of DP steels with the best strength was comprised of high volume percentages of fresh martensite and stronger ferrite strengthened by ferrite grain refinement and fine carbonitride precipitates in ferrite matrix.

Concerning ductility, from the middle of the 1970s, many metallurgists and materials scientists have investigated the effects of microstructural features, i.e., grain sizes, ferrite volume fraction and inclusions, on total elongation (TE). Shear-edge ductility or hole expansion ratio (HER) is another aspect of ductility. The key elements controlling HER are not yet fully understood. The fracture related to the ductility based on TE and HER is associated with the

cracking that occurs inside the (1) ferrite/ martensite boundaries, (2) ferrite/ cementite interfaces and (3) martensite itself [39]. In addition, recent literature [21,40–43] showed that retained austenite may play a critical role in governing both TE and HER, which was due to transformation-induced plasticity (TRIP) effect. So, TRIP steels [44], and quench and partitioning (Q&P) steels [45] were subsequently developed.

The main purpose of this dissertation was to determine how and to what extent the strength of DP steels could be enhanced, while not severely sacrificing TE or HER. Also, in order to obtain ultra-high strength and superior ductility, conforming to the properties of Generation III steels (defined by the product of UTS  $\times$  TE greater than 22,000 MPa  $\times$  %) [34,46], DP steels with 0.15 wt.% C, 0.04/0.4/0.8 wt.% Al and 0.06/0.12 wt.% V have been designed and melted. The pre-annealing conditions studied included two coiling temperatures: 580°C (bainitic ferrite as the starting structures) and 677°C (polygonal ferrite and pearlite as the initial structures) and one cold reduction of 60%. Furthermore, two annealing continuous galvanizing line (CGL) simulations were selected for this study. The first annealing simulation was the standard galvanizing (GI) treatment and the second one was the supercooling (SC) process which are described in the following chapters.

## **2.0 Background**

### **2.1 Origin and Need for High Strength Steels in Automobiles**

The need for high-strength steels in automotive applications came about in the 1970s. First, the oil embargo came from Middle East, and second were the passenger safety issues stemming from the US Transportation Department [47]. These two issues can be improved by automotive weight reduction through the use of high strength steels.

Before the 1970s, there were essentially two types of automotive steels: low strength hot-rolled or cold rolled and annealed steels with a UTS of ~300 MPa, such as aluminum-killed drawing quality (AKDQ) ferrite-pearlite steels, for automotive panels and structures, and quench and tempered medium-carbon martensitic steels for gear, suspensions and transmission parts. When the oil crisis occurred in 1975, automakers were suddenly asked to produce vehicles which could conserve oil and CO<sub>2</sub> emissions, by substituting higher strength steels. A few years later, they were further asked to make the cars safer for crash worthiness or occupant safety, by again substituting higher strength steels. All these disruptions forced automakers to find the approaches of producing higher strength, thinner steels. Since then, numerous publications have focused on the thinner high strength steels for automotive applications.

DP steels are the typical representative of low carbon high strength steels used as automotive structural materials, since they have high strength combined with decent ductility and good spot weldability. One of the first papers on DP steels was written by Hayami and Furukawa [48] in 1975, followed by the works done by Davies [5–8], Speich [9,10] and Rashid [11,12] from 1978 to the early 1980s. At the same time, Japanese researchers [35,36] were developing the

processing lines for continuous annealing of cold-rolled sheet steels and later followed by hot-dip galvanizing lines involving intercritical annealing. These two processes are now common in modern sheet steel production.

There are three purposes of hot-dip galvanizing lines: (i) relieving the high strain introduced by hot and cold rolling, thereby making them more formable for automotive applications, (ii) intercritical annealing permits the formation of the dual-phase structures to occur after rapid cooling from the intercritical annealing temperature (IAT, near 790°C to the zinc pot temperature (near 460°C) and then further to room temperature), and (iii) providing the thinner high strength annealed steels with corrosion resisting Zn coatings to minimize corrosion from halide-rich, anti-icing road treatments. So, CGL processing includes (i) reheating the cold-rolled sheet steels to an IAT, (ii) short-time isothermal holding at an IAT, (iii) cooling from an IAT to the zinc pot temperature of 460°C, (iv) short-time isothermal holding at 460°C and (v) cooling from 460°C to room temperature.

When combining all these technologies, the result is the platform leading to today's production of DP steels for weight reduction.

## **2.2 Metallurgical Knowledge**

### **2.2.1 Intercritical Annealing Technology**

From the early 1970s through the mid 1980s, researchers conducted some fundamental studies of DP steels, since they did not know how to produce these steels or microstructures. In order to obtain a good combination of strength and ductility, the final microstructures of DP steels

comprise ferrite and dispersed martensite islands. One common processing route for DP steels includes reheating the initial microstructures in the intercritical regime ( $\alpha + \gamma$ ) with a short holding time, followed by continuous cooling to the room temperature [4,11,12,27,28,49,50]. The intercritically formed austenite can transform into fresh martensite after rapid continuous cooling. This procedure is called intercritical annealing in a continuous annealing line. In addition, the other approach is full annealing, in which the steels are reheated above the  $A_{C3}$  temperature (full austenite regime), followed by controlled accelerated cooling to room temperature [4,12]. The adjusted accelerated cooling rate of full annealing is critical, since it enables most of the austenite to transform into ferrite and the rest to transform into martensite. Finally, two-phase microstructures can be formed in a CGL by cooling from the IAT to the zinc pot temperature followed by cooling to room temperature.

### **2.2.1.1 Ferrite Recrystallization and Austenite Formation in the Two-Phase Region**

Ferrite recrystallization of the cold rolled ferrite starting material, and austenite formation (nucleation and growth) occur during heating and isothermal holding at IATs, depending on starting microstructures, heating rates and intercritical annealing time and temperatures.

Ferrite recrystallization does not occur for the DP steels with the initial microstructures of hot-rolled ferrite plus pearlite, and it only exists for the cold rolled steels during annealing. Garcia and DeArdo [51] reported that ferrite recrystallization was complete prior to austenite formation for the DP steels with the starting microstructures of cold-rolled ferrite-pearlite segregates and at a low heating rate. Later, Yang et al. [52] also made intercritical annealing studies of cold rolled DP steels. Unlike Garcia and DeArdo's research results [51], Yang et al. [52] found that at a higher heating rate, austenite nucleated, accompanied by ferrite recrystallization and pearlite spheroidization, and that the time required for ferrite recrystallization or pearlite spheroidization

decreased as cold reduction and annealing temperature increased. This was the first proof that the stored energy of the starting conditions could influence the kinetics of intercritical annealing. These cases also showed that the heating rate has a critical effect on ferrite recrystallization. In summary, ferrite recrystallization normally completes during reheating at a low heating rate, while ferrite recrystallization is delayed to the austenite nucleation start temperature at a high heating rate [53].

Speich et al. [9] concluded three stages in which austenite formation occurred during intercritical annealing for high Mn hot rolled ferrite pearlite steels. The first stage included austenite nucleation in the ferrite/pearlite interface boundaries, followed by the growth of austenite into pearlite, consuming the undissolved cementite in the prior pearlite colonies. The second stage was the transformation of austenite into ferrite during cooling, controlled by the carbon diffusion in austenite at a high IAT or dominated by the manganese diffusion in ferrite at a low IAT. The last one was the austenite and ferrite equilibrium governed by manganese diffusion in ferrite.

Garcia and DeArdo [51] studied the formation of austenite during intercritical annealing in terms of the Mn steels with different starting microstructures, but using slow heating rates. They concluded that austenite always nucleated associated with the cementite existing in the ferrite/ferrite grain boundaries. Barbier et al. [50] found that austenite nucleation preferred to occur at cementite particles located in the high Mn segregation bands, since Mn is the austenite stabilizer.

The amount of the intercritically formed austenite during intercritical annealing depends on the IAT and carbon content. For a given carbon content, increasing the IAT leads to a larger amount of austenite, from the level rule. At a given IAT, higher carbon contents increase the volume fraction of austenite.

Also, the heating rate can have an influence on the morphology and distribution of intercritically formed austenite. Huang et al. [53] investigated the effects of heating rates on the austenite formation of steels with initially hot rolled and cold rolled ferrite + pearlite microstructures. For hot band coils at a low heating rate, austenite first nucleated at the pearlite lamellar cementite-ferrite interfaces until all the cementite in pearlite was completely dissolved. Later, some austenite nucleated at the ferrite/ferrite grain boundaries associated with cementite in competition with the austenite growth in the prior pearlite location. The low heating rate enables the sufficient growth of pearlite-nucleated austenite, compared with the ferrite/ ferrite boundary-nucleated austenite. In terms of steels with a starting microstructure of hot rolled ferrite + pearlite at a high heating rate, pearlite-nucleated austenite coexisted with ferrite/ ferrite boundary-nucleated austenite, and as a result, there was no growth competition between pearlite-nucleated austenite and boundary-nucleated austenite, during subsequent soaking. With regard to the cold rolled steels at a low heating rate, the distribution of intercritically formed austenite was similar to that of austenite formed from hot rolled steels at a low heating rate, since ferrite recrystallization completed prior to austenite nucleation. However, the morphology of pearlite-nucleated austenite was different, since prior pearlite was deformed and elongated due to cold rolling. For the cold rolled structures at a high heating rate, the high heating rate retards the ferrite recrystallization, so ferrite recrystallization coexisted with austenite formation during holding at the IAT. Ferrite/ferrite grain boundaries were moving and there were no austenite nucleation sites associated with ferrite grain boundaries. So, austenite only nucleated and grew at the prior pearlite areas and there was absence of ferrite/ferrite boundary-nucleated austenite.

## **2.2.1.2 Austenite Decomposition during Continuous Cooling from the Intercritical**

### **Annealing Temperatures**

Intercritical annealing temperature determines the volume fraction, grain size and carbon content of austenite, governing the hardenability of intercritically formed austenite. Hardenability is a crucial factor which controls the austenite decomposition products after cooling. Fig. 2.1 shows effects of IATs on austenite volume fraction, austenite carbon content and martensite start temperature [21]. It is apparent that increasing the IAT increases the volume percentage of austenite and reduces the carbon content in austenite, thereby lowering the hardenability of austenite and making it unstable. Unlike martensite, some other austenite decomposition products may be formed even at a reasonably high cooling rate. Furthermore, the morphologies and microstructures of martensite transformed from intercritically formed austenite are also affected by IATs. The martensite structures can vary from lath martensite of typical austenite in low carbon steels to twinned martensite of typical austenite in high carbon steels [10]. The differences in morphologies are attributed to the effects of carbon content of austenite formed at the different annealing temperatures.

Garcia and DeArdo [26] investigated the effect of carbide dissolution on the amount of intercritically formed austenite and subsequent phase transformation after fast cooling. Carbide dissolution increased the carbon content and hardenability of austenite during intercritical annealing. As a result, a higher percentage of austenite transforms into fresh martensite after accelerated cooling. Thus, determining the carbide dissolution temperature of a specific DP steel is an essential step to obtain the desirable volume fraction of fresh martensite in the final microstructure of DP steels.

In addition, alloying elements like Mn [13,54], Cr [27,34,55] Mo [27,34,55] and V [56,57] can also increase the hardenability of austenite, suppressing the formation of proeutectoid ferrite, pearlite and bainite after rapid cooling. It has been found that Mn, Cr and Mo also lower the critical cooling rate for the transformation of austenite into fresh martensite [13].

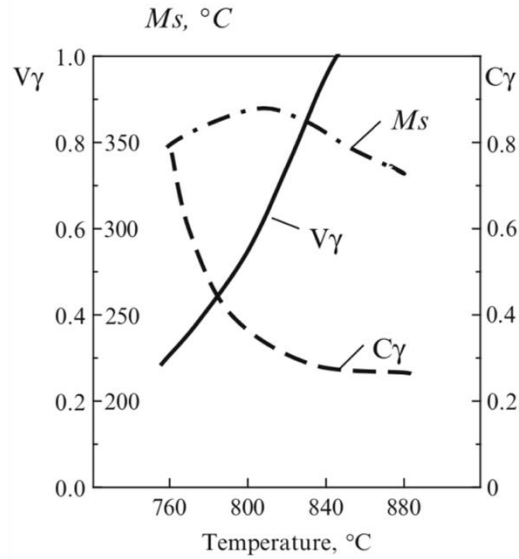


**Figure 2.1** The effects of IATs on austenite volume fraction, austenite carbon content and martensite start temperature [21].

The intersection of the cooling rate curves with the CCT diagram of the intercritically formed austenite determined by the chemical composition of DP steels predict the austenite decomposition products in the final microstructure after continuous cooling (seen in Fig 2.2 [58]). In Fig. 2.2, when the cooling rate exceeds  $187^\circ\text{C s}^{-1}$ , all of the austenite transforms into martensite. Reducing the cooling rate causes the formation of ferritic microstructures or bainite to replace the fresh martensite. So, it is vital to find the critical cooling rate for martensite transformed from intercritically formed austenite. Tanaka et al. [59] put forward the critical cooling rate equation dependent on Mn, Si, Cr and Mo contents (seen in Eqs. 2.1 to 2.2).

$$\text{Mn}_{\text{eq}}\% = \text{Mn}\% + 0.26 \times \text{Si}\% + 3.5 \times \text{P}\% + 1.3 \times \text{Cr}\% + 2.67 \times \text{Mo}\% \quad (2.1)$$

$$\log \text{CR} \geq -1.73 \times \text{Mn}_{\text{eq}}\% + 3.95 \quad (2.2)$$

where,  $\text{Mn}_{\text{eq}}\%$  is the Mn equivalent content in weight percent and CR denotes the critical cooling rate.

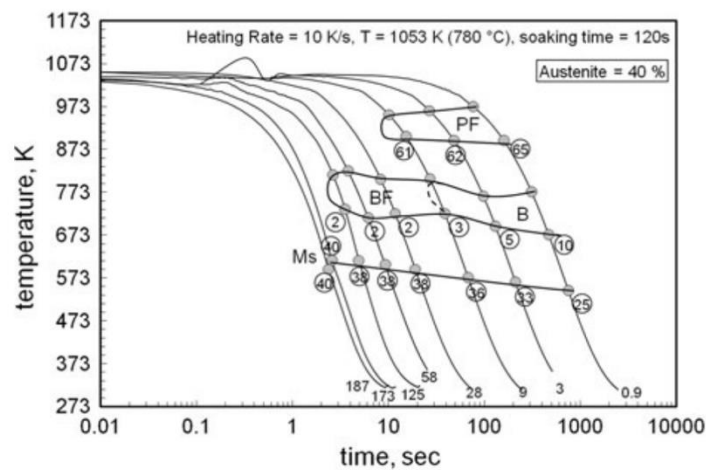


**Figure 2.2** The CCT diagram of a C-Mn-Cr-Mo-Si DP steels intercritically annealed at 780°C at a heating rate of 10 °C s<sup>-1</sup> and isothermally held for 120 s. A variety of cooling rates intersecting the CCT diagram determine the transformation temperatures of different austenite decomposition products (i.e., polygonal ferrite (PF), bainitic or acicular ferrite (BF), bainite (B) and martensite (M)) [58].

### 2.2.1.3 Retained Austenite in the Final Microstructures after CGL

Previous literatures [19,30,41–43,60–63] showed that retained austenite was found in the final microstructures of DP steels. The amount of retained austenite can be controlled by chemical compositions, cooling rates, IATs and hot-dip galvanizing isothermal holding time. The volume fraction of retained austenite can be increase by adding higher amounts of C [10,41] Mn [19,42], and Si [19,42,61]. For instance, in Saleh’s research [61], he found that the amount of retained

austenite increased with increasing Si contents. During the isothermal holding at the bainite transformation temperature of about 400°C, Si can effectively suppress the formation of cementite and delay bainite transformation, and thus carbon enrichment stabilizes the austenite [41,61,64]. As a result, a larger amount of austenite is retained in the final microstructures during fast cooling from the bainite transformation temperature to room temperature. Eggbauer et al. [63] found that high cooling rates resulted in higher volume fractions of retained austenite, which means that larger volume percentages of retained austenite can be obtained in the air-cooled steels than those in the water-quenched steels [10]. In addition, Matsumura et al. [41,64] concluded that the amount of retained austenite decreased with extending isothermal holding time as well as lowering the austempering temperatures.

Retained austenite affects both the strength and ductility of DP steels [41]. During the deformation of DP steels, retained austenite transforms into martensite. The TRIP effect improves the ductility, and meanwhile, the martensite transformed from retained austenite improves the tensile strength. In addition, retained austenite also has a critical impact on the shear-edge ductility [65], which will be discussed in the following section.

### **2.2.2 Chemical Compositions**

The compositions used in DP steels influence (i) the  $A_{C1}$  and  $A_{C3}$  critical temperatures and the  $\alpha + \gamma$  two phase region in the Fe-C phase diagram; (ii) the kinetics of ferrite recrystallization and austenite formation during reheating to the desired IAT and soaking; (iii) the amount and morphology of the intercritically formed austenite at given IAT and holding time; (iv) the hardenability of the intercritically formed austenite during cooling from the desired IATs to the room temperature; (v)  $B_s$  and  $M_s$  temperatures along with the critical cooling rate in the CCT

diagram; (vi) the volume percentages and morphologies of different austenite decomposition products at controlled cooling rates; and (vii) the strength contribution due to precipitation hardening in terms of the newly formed ferrite, i.e., beyond that of the ferrite inherited from the cold rolled hot band.

### 2.2.2.1 Carbon

The variations in carbon contents influence the amount of intercritically formed austenite during reheating cold rolled DP steels from room temperature to the desired IATs. This effect can be expressed as an austenite formation rate (the volume percentage of austenite per second ( $fv_{(\gamma)} \text{ } ^\circ\text{C}^{-1}$ )), which is dependent on the width of the intercritical or two-phase ( $\alpha + \gamma$ ) range in the Fe-C diagram, from the lever rule. Decreasing C contents results in a wider intercritical or two-phase ( $\alpha + \gamma$ ) range, hence reducing the austenite formation rate ( $fv_{(\gamma)} \text{ } ^\circ\text{C}^{-1}$ ) during heating. For example, Fonstein [21] reported that reducing the C levels from 0.18 wt.% to 0.07 wt. % in a Cr-Mn-Si-B steel caused the decrease in austenite formation rates ( $fv_{(\gamma)} \text{ } ^\circ\text{C}^{-1}$ ) from 6%  $^\circ\text{C}^{-1}$  to 2.3%  $^\circ\text{C}^{-1}$ .

In addition to the amount of intercritically formed austenite, carbon contents also have an impact on the austenite growth kinetics in the intercritical or two-phase ( $\alpha + \gamma$ ) range. From the previous studies [53,66], it is found that austenite nucleated at the interfaces between pearlitic ferrite and cementite within pearlite colonies, and at the ferrite/ferrite grain boundaries associated cementite particles. Also, subsequent austenite growth is mainly governed by carbon diffusion. For example, the interface velocity can be expressed by Eq. 2.3 [67,68],

$$v_{\alpha\gamma} = M_0^{\alpha\gamma} e^{(-Q_{\alpha\gamma}/RT)} \Delta G \quad (2.3)$$

where,  $v_{\alpha\gamma}$  is interface velocity,  $M_0^{\alpha\gamma}$  the material factor controlling the interface mobility,  $Q_{\alpha\gamma}$  the activation energy of boundary motion and  $\Delta G$  the chemical driving force. Also,  $\Delta G$  varies with two discrete austenite nucleation sites. The chemical driving force ( $\Delta G_I$ ) of the austenite growth within the pearlite colonies can be expressed by using Eq. 2.4 [69].

$$\Delta G_I = \chi_{(T)} (x^{\gamma/\alpha} - x^\gamma) \quad (2.4)$$

where,  $\chi_{(T)}$  is the proportional factor,  $x^{\gamma/\alpha}$  is the carbon concentration of moving the interface of  $\gamma/\alpha$  and  $x^\gamma$  is the concentration of carbon at equilibrium in austenite at a given temperature. In terms of the austenite generated from ferrite/ferrite grain boundaries, the chemical driving force ( $\Delta G_{II}$ ) for austenite growth is shown in Eq. 2.5 [66].

$$\Delta G_{II} = \chi_{(T)} (x^{\alpha/\gamma} - x^\alpha) \quad (2.5)$$

where,  $x^{\alpha/\gamma}$  is the carbon concentration in ferrite to move the  $\gamma/\alpha$  interface and  $x^\alpha$  the carbon concentration at equilibrium in ferrite at a given temperature. From Eqs. 2.3–2.5, it is obvious that the austenitization rate is strongly controlled by the carbon differences in  $\gamma/\alpha$  interface,  $\gamma$ - and  $\alpha$ -phases.

Also, hardenability is the ability of a steel to be hardened by obtaining some volume percentage of martensite transformed from austenite after quenching at a given depth, which can be measured by a standard Jominy end-quench test [70,71]. Hardenability strongly relies on chemical compositions and it is a critical factor controlling the austenite stability and its decomposition products after cooling from the intercritical or two-phase ( $\alpha + \gamma$ ) range. The carbon contents associated with intercritical annealing temperatures (IATs) importantly influence the

hardenability of austenite in DP steels. A high intercritical annealing temperature, from the lever rule in a Fe-C diagram, results in a larger amount of intercritically formed austenite with low carbon content and hardenability, thus making austenite unstable. On the contrary, when the cold rolled DP steels are intercritically annealed at a low temperature, a smaller amount of austenite containing high carbon content will be obtained, giving a rise to the high hardenability and stability of the intercritically formed austenite [10].

### **2.2.2.2 Manganese**

Manganese is a critical alloying element dominating the final microstructures and mechanical properties of DP steels. The Mn additions have effects on the Fe-C phase diagram. Calcagnotto et al. [13] investigated the influences of Mn in 0.15C-0.8Mn-0.3Si and 0.15C-1.6Mn-0.3Si DP steels and they found that increasing Mn levels lowered both  $A_{C1}$  and  $A_{C3}$  temperatures from 733°C to 721°C and from 845°C to 835°C, respectively, which was due to the carbon diffusion retardation cause by Mn additions. Hence, the intercritically formed austenite volume percentages of the DP steels with Mn additions should be higher than those of DP steels without Mn at the similar intercritical annealing temperatures. Also, Mn additions lower the eutectoid temperatures (shown in Fig. 2.3 (a)) and reduce eutectoid carbon contents (Fig. 2.3 (b)) [14]. Figs. 2.3 (a) and (b) show the effects of microalloying elements on the transformation temperature and carbon content in the eutectoid point in a Fe-C phase diagram, respectively. So, the volume fraction of intercritically formed austenite can be raised as Mn levels increase. Moreover, Toji et al. [15] concluded that the low diffusivity of Mn resulted in low Mn partitioning in the intercritically formed austenite at the early stage of austenite formation and a longer intercritical annealing time needed to enhance austenite stability and reach a maximum austenite volume percentages at a given IAT. Furthermore, Mn additions are beneficial to a finer distribution of cementite in the

starting microstructures of DP steels before annealing, which results in providing a stronger Zener pinning effects on grain boundaries and retarding subsequent austenite grain growth in an intercritical or two-phase ( $\alpha + \gamma$ ) range [13].

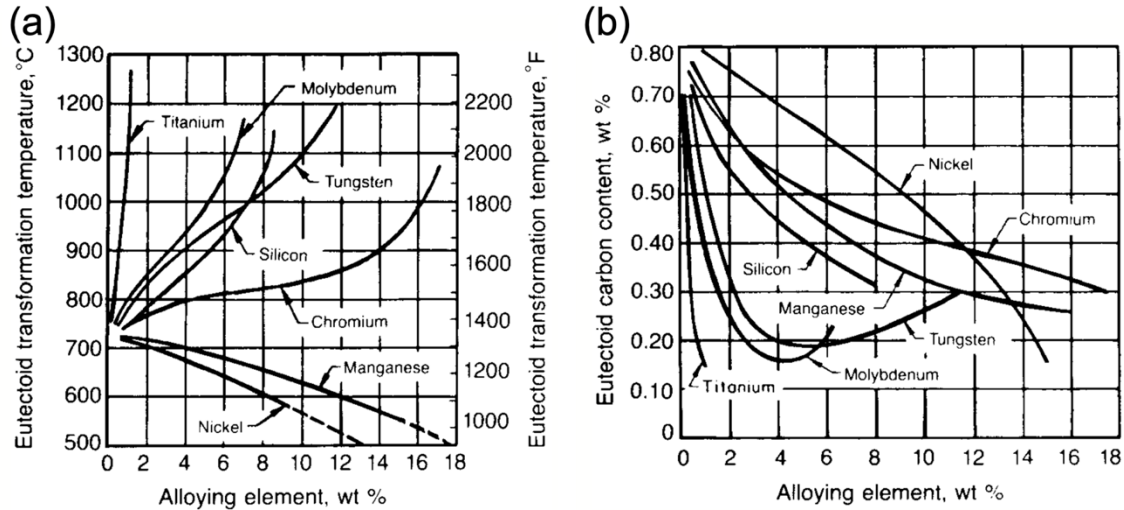


**Figure 2.3 Effects of microalloying elements on eutectoid transformation temperatures and eutectoid carbon contents in the Fe-C phase diagram [14].**

In addition to austenite nucleation and growth, ferrite recrystallization occurs during heating and isothermal holding in an intercritical or two-phase ( $\alpha + \gamma$ ) range, since the initial microstructures of DP steels, prior to continuous annealing, often consist of cold rolled ferrite and pearlite. Mn additions also can have influences on ferrite recrystallization behaviors. For instance, Pradhan [72] reported that, both recrystallization start and finish temperatures increased with increasing Mn levels in a 0.05C-0.06P-0.04Nb-0.085V steel,. In previous research [50,53,73,74], the competition between ferrite recrystallization and austenite growth occurred during reheating at a high heating rate and subsequent isothermal holding in an intercritical or two-phase ( $\alpha + \gamma$ ) range. Thus, the effect of Mn additions on ferrite recrystallization behaviors will also indirectly benefit the amount of intercritically formed austenite.

Moreover, Mn additions enhance the hardenability of austenite, since Mn prefers to partition in austenite and increases carbon solubility in austenite [13]. And as a result, the increase in Mn levels suppresses the formation of ferrite, pearlite and bainite and reduces the critical cooling rates for the transformation from austenite to martensite [17,21].

### 2.2.2.3 Aluminum

Aluminum is one of the ferrite stabilizer elements, which can increase  $A_{C1}$  and  $A_{C3}$  temperatures and enlarge both the ferrite field and the  $\alpha+\gamma$  regime in the Fe-C phase diagram. Therefore, higher IATs must be used in the DP steels with higher Al contents (seen in Fig. 2.4) for DP steels to obtain enough initial austenite during heating and holding as well as fresh martensite after full CGL process. Girina and Fonstein [20] studied effects of Al on the microstructures and mechanical properties of DP steels. In their research, Al contents varied from 0.04 wt.% to 1.1 wt.% and the temperature range ( $A_{C3} - A_{C1}$ ) varied from 135°C to 255°C.

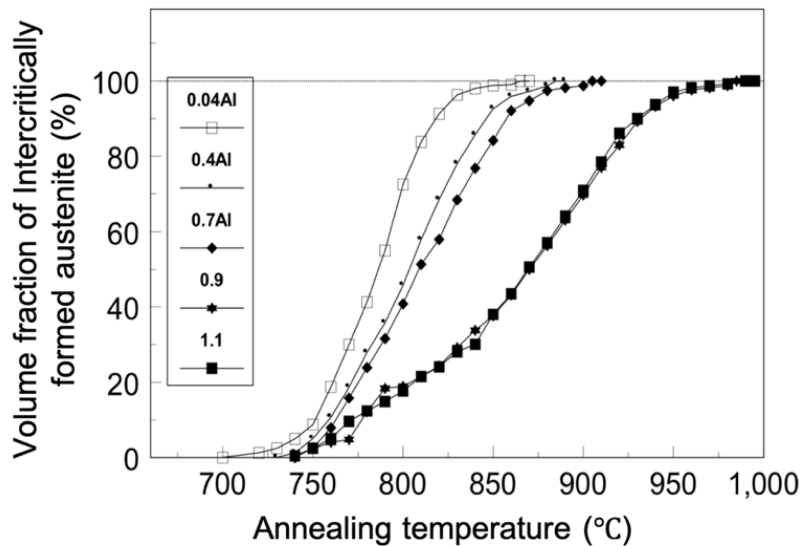


Figure 2.4 The relationship between the volume percentages of intercritically formed austenite and annealing temperatures of DP steels with different Al levels [20].

In addition, increasing the Al contents decreases the carbon content and hardenability of the intercritically formed austenite. So, higher critical cooling rates are needed for the DP steels with the high content of Al [21]. It is inevitable that, with respect to steels with high Al level, a high-volume-fraction of new ferrite will form even after fast cooling from the intercritical temperature range. Also, effects of Al on the mechanical properties of DP steels are shown in Fig. 2.5 [20]. Fig. 2.5 shows the UTS vs TE of DP steels with different Al contents after full CGL simulations. It is apparent that the addition of Al causes the sacrifice in tensile strength, however, the ductility, like TE or  $TS \times TE$  can improve remarkably as Al content increases [75]. Al increases the diffusion coefficients of everything in ferrite including the self-diffusion of Fe causing more ferrite recrystallization and softer ferrite [76]. This is good for ductility but bad for strength. Kang et al. [77] investigated the effect of Al on the ferrite recrystallization behavior in high strength interstitial free (IF) steels. They found that increasing Al contents increased the ferrite recrystallization rate and thus improved the ductility of ferritic steels.

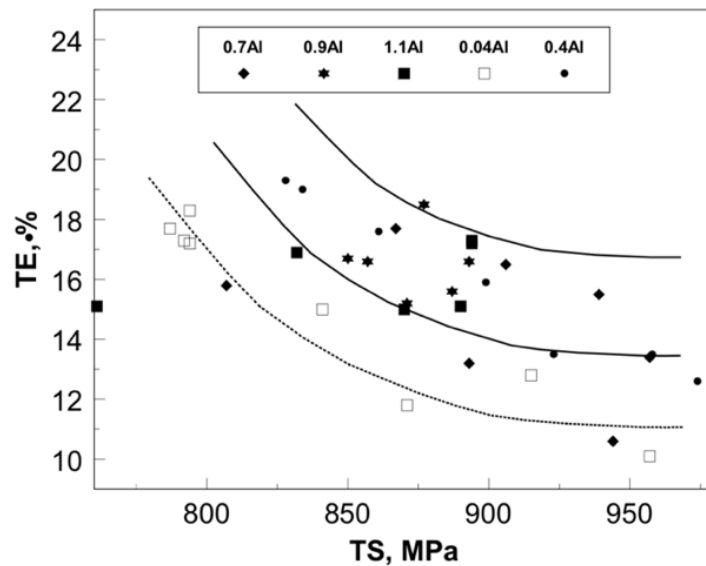


Figure 2.5 UTS vs TE of DP steels with different Al contents after full CGL simulations [20].

#### 2.2.2.4 Chromium

Cr is the alloying element often used in DP steels. Kong [16] and et al. studied the transformation kinetics from pearlite to austenite in 0.1 wt.% C - (2.0/4.0/6.0/8.0) Cr steels. They found that increasing Cr levels reduced the pearlite interlamellar spacing in the initial microstructures prior to annealing, which provided more austenite nucleation sites, since austenite prefers to nucleate at the interfaces of ferrite/cementite within pearlite colonies [53,66]. Additionally, Cr is one of the carbide forming elements [17]. So, more chromium carbide formation is led by Cr additions and these chromium carbides serve as austenite nucleation sites. In terms of austenite growth, which is dominated by the mobility of  $\alpha/\gamma$  interfaces and carbon diffusivity in austenite [21]. Cr additions refined pearlite structures, so the smaller pearlite interlamellar spacing reduces the carbon diffusion distance. In addition, the long distance diffusion of Cr from pearlitic cementite to the  $\alpha/\gamma$  interfaces can also accelerate the austenite growth rate [16].

In terms of the transformation from the intercritical formed austenite to austenite decomposition products, Cr additions improve the hardenability of austenite, affecting the transformation kinetics of new ferrite, pearlite and bainite (seen in Fig. 2.6). Figs. 2.6 (a) and (b) show the CCT diagram of a 0.15 wt.% C-2.0Mn-0.006Nb DP steel without and with Nb additions, respectively, studied by Girina et al. [22]. Increasing Cr levels retarded the formation of new ferrite, since Cr additions moved the ferrite formation to the lower cooling rates. Additionally, the increase in Cr contents resulted in lowering bainite start temperature ( $B_s$ ) and extending the bainite transformation time, regarding the critical process of zinc coating or hot-dip galvanizing, so that bainitic constituents can be minimized in the final microstructures of the Zn-coated DP steels.

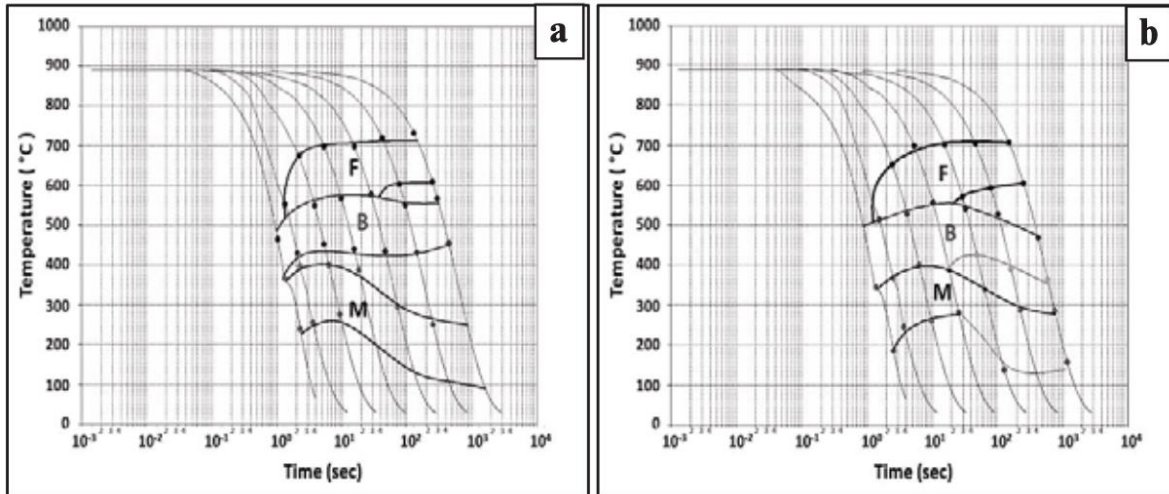


Figure 2.6 The CCT diagrams of a 0.15C-2.0Mn-0.006Nb DP steel (a) without Nb and (b) with Nb additions [22].

### 2.2.2.5 Vanadium

The structure-property relationships of DP steels have been investigated by a variety of researchers [5,7,11,24,31,32]. The high strength of DP steels relies on a high-volume-fraction of fresh martensite, refined ferrite grain sizes and possibly fine carbonitride precipitates in the ferrite matrix (seen in Fig. 2.7 (a)). The total strength of a dual phase can be expressed by the combination of ferrite strength and fresh martensite strength with the application of rule of mixtures. V is a common carbonitride forming element, so fine vanadium carbonitride precipitates formed in ferrite matrix can improve the ferrite and total strength of dual phase steels [23]. Also, V has a considerable effect on refining structures, contributing to high UTS of DP steels [24].

In addition to strength, Davies [5] found that V also played a critical role in controlling ductility and initial strain hardening rate of DP steels. In order to develop work hardening behavior and ductility, both carbonitride precipitates and interstitial content of ferrite needed to be minimized (seen in Figs. 2.7 (b)–(d)). The V content needs to be near the solubility limit of VCN

in ferrite especially in the 600°C ~ 400°C temperature range to keep the VCN volume fraction small and lower the carbon content in ferrite matrix.

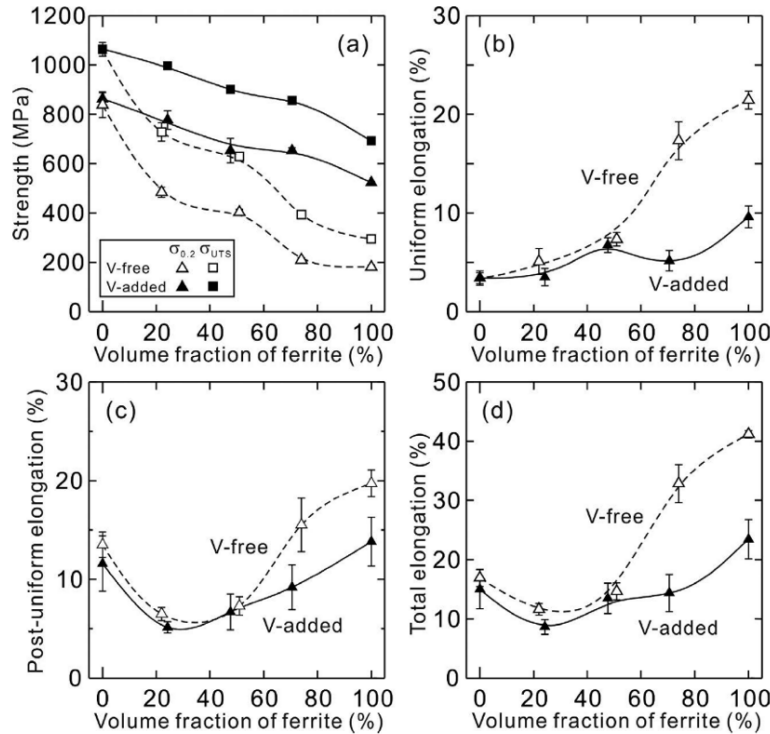


Figure 2.7 The relations between ferrite and (a) strength, (b) uniform elongation (UE), (c) post uniform elongation (Post UE) and (d) TE of steels with or without V addition [78].

### 2.2.3 Strengthening Mechanisms

In order to increase the total strength, the final microstructures of DP steels should comprise higher percentages of fresh martensite and stronger ferrite strengthened by ferrite grain refinement, carbonitride precipitates in ferrite matrix and high dislocation density in the vicinity of ferrite/martensite interfaces.

### 2.2.3.1 Rule of Mixtures (Banded Martensite)

In 1965, Kelly and Tyson [79] put forward a basic theory for the strength of fiber-reinforced composites, which was later explained and developed by Mileiko [80] and Garmomg and Thompson [81]. This theory can be expressed by Eq. 2.6 [79].

$$\sigma_C = \sigma_f V_f + \sigma_m (1 - V_f) \quad (2.6)$$

where,  $\sigma_C$ ,  $\sigma_f$  and  $\sigma_m$  are the strengths of composite, fiber and matrix, respectively and  $V_f$  is the volume percentage of fiber.

Prior to continuous annealing, the initial cold-rolled microstructure of DP steels consists of banded ferrite and pearlite, which are elongated along the rolling direction. The majority of intercritically formed austenite are pearlite-nucleated austenite lying in the prior dissolving pearlite areas during intercritical annealing, followed by the transformation of austenite into banded martensite after continuous cooling. In addition, experimental data in Davies' researches [5–8] showed that both YS and UTS of DP steels had a linear positive relation with the volume percentage of fresh martensite. These banded martensitic microstructures can be considered as the discontinuous fiber in the composite, and thus the rule of mixtures for strength can be applied to explain the relationship between the strength of DP steels and the volume fraction of fresh martensite. So, Eq. 2.6 can be rewritten in the form of Eq. 2.7.

$$\sigma_Y = \sigma_{\alpha'} V_{\alpha'} + \sigma_{\alpha} (1 - V_{\alpha'}) \quad (2.7)$$

where,  $\sigma_{UTS}$ ,  $\sigma_{\alpha'}$  and  $\sigma_{\alpha}$  are the strengths of DP steels, martensite and ferrite, respectively and  $V_{\alpha'}$  is the volume fraction of fresh martensite. From this rule of mixtures, both YS and UTS increase with the increase of the volume percentage of fresh martensite.

### 2.2.3.2 Grain Refinement

The Hall-Petch relation [82,83] was proposed in the beginning of the 1950s and later applied to various polycrystalline metals and alloys. This relation can be written as Eq. 2.8,

$$\sigma_Y = \sigma_0 + k_1 d_{GB}^{-1/2} \quad (2.8)$$

where,  $\sigma_Y$  is yield strength;  $\sigma_0$  is Peierls-Nabarro stress;  $k_1$  is material constant and  $d_{GB}$  is the ferrite grain size bounded by high angle boundaries. In the dislocation theory, dislocation pileups and stress concentration occur near the grain boundary regions, since grain boundaries work as the potential barriers for the motion of dislocations. The shear stress at the pile-up tip should be large enough to cross the grain boundary and move to another grain [84]. Thus, the applied stress for a dislocation moving through the grain boundary area is higher, compared with that for dislocation displacements in the grain center. So, the smaller grain sizes, the more grain boundaries, the more dislocation movement barriers, and the more strength contribution to yield strength.

### 2.2.3.3 Dislocation Strengthening

However, Hall-Petch relation is not the only model which can explain the effects of grain boundaries on the strength of polycrystalline metals and alloys. In the Hall-Petch relation, the dislocation are generated from grain centers or related to the operation of Frank-Read sources [84]; while in Li's [85] study, he proposed that dislocations came from grain boundaries. So, concerning

the relationship between work hardening and dislocation density, the grain-size dependent yield stress equation can be rewritten as Eq. 2.9,

$$\sigma_Y = \sigma_0 + \alpha b G \rho^{-1/2} \quad (2.9)$$

where,  $\sigma_Y$  is the yield strength;  $\sigma_0$  is the Peierls-Nabarro stress;  $\alpha$  is material constant,  $b$  is the Burgers vector,  $G$  is the shear modulus and  $\rho$  is the dislocation density.

Sherman et al. [86] found that the measured average dislocation densities in ferrite were related to the volume fraction of fresh martensite for the as quenched and air cooled DP steels in two conditions: without plastic deformation (seen in Fig. 2.8 (a)) and with 7% cold worked (seen in Fig. 2.8 (b)). The dislocation density in ferrite increases with increasing the amount of fresh martensite.

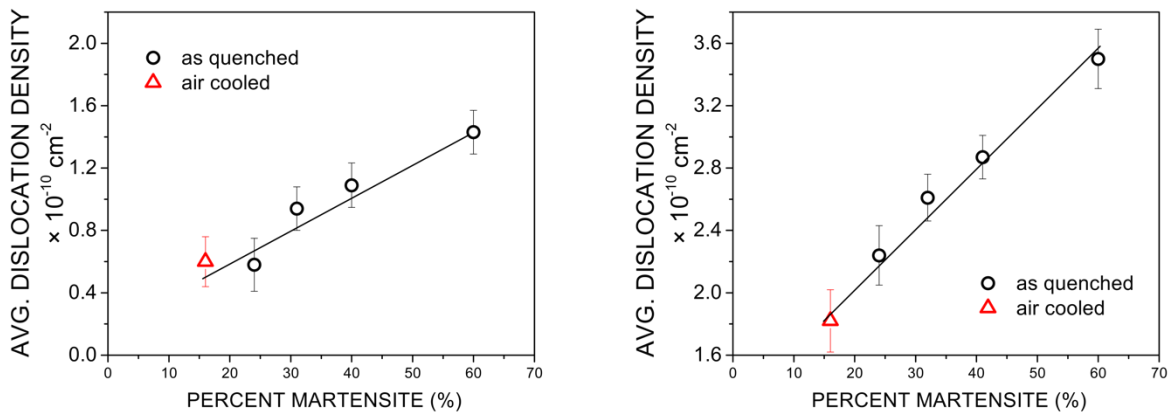


**Figure 2.8** The measured average dislocation density in ferrite as a function of martensite percentage for the as quenched and air cooled DP steels (a) without plastic deformation (b) with 7% cold deformation [86].

Prior to plastic deformation, the dislocations in ferrite are transformation induced dislocations resulting from the austenite-martensite transformation. For DP steels, intercritically formed austenite transforms into fresh martensite after rapid cooling, causing the volume

expansion. and dislocations associated with the reconstructive  $\gamma$ - $\alpha$  transformation. Therefore, there are two contributions to the pre-deformation dislocation density: (i) to accommodate the volume expansion and (ii) to permit the shear transformation to occur. Thus, both a high dislocation density and residual stresses are generated in the vicinity of ferrite/martensite interfaces [10]. This explains why there is often no yield point in DP steels, since the yield point is not likely in high dislocation density ferrite.

In addition, during tensile testing, the formation of dislocation cell structures starts with dislocation tangles at a small tensile strain ( $\sim 0.05\%$ ) and the structure consists of dislocation cell walls with high dislocation density at a higher tensile strain [87]. So the yield strength increases due to (1) the interaction of dislocation stress fields, (2) the interaction generating sessile locks and (3) the dislocation intersections of one slip system and another forming dislocation jogs [88].

#### **2.2.3.4 Precipitation Hardening**

A lean amount of microalloying elements such as Ti, Nb and V is widely used in modern steels, like HSLA steels or DP steels. The strengthening effects of these microalloying elements can be classified as (i) grain refinement, (ii) precipitation (or dispersion) strengthening at high transformation temperatures or (iii) dislocation/transformation strengthening at low transformation temperatures through hardenability. The precise behavior of microalloying elements in a given steel is the result of the solubility of their carbonitrides in austenite or ferrite and the thermomechanical processing (TMP) used in their production [89]. In order to achieve the goal of the grain refinement, prior to phase transformation from austenite to ferrite, the microalloying element carbonitrides should be either undissolved in austenite to pin boundaries during reheating or precipitated in austenite during hot deformation. Also, with respect to dispersion strengthening, the microalloying element carbonitrides are supposed to precipitate in ferrite during or after the

phase transformation, especially at high transformation temperatures, i.e., as in polygonal ferrite [28]. Obviously, for precipitation to occur in ferrite, the microalloying elements must have sufficient atomic mobility, and this requires higher transformation temperatures. Only the precipitation strengthening mechanism will be discussed in this section.

The effect of precipitation strengthening on yield strength is dependent on the nature of precipitate particles (deformable or undeformable), particle sizes, particle volume fractions and the interaction between particles and dislocations (particle shearing in the Friedel Process or particle bypass in the Orowan Process) [90]. For modern steels, TiN, TiC, Nb(C, N) and V(C, N) particles often play significant roles in increasing strengths. These are hard or undeformable particles, and dislocations bypass these particles, forming Orowan dislocation loops. So, the Ashby-Orowan [91,92] model was adapted, and it can be expressed by Eq. 2.10 [90],

$$\Delta\sigma_Y = (0.538Gb\sqrt{f}/X) \ln(X/2b) \quad (2.10)$$

where,  $\Delta\sigma_Y$  is the contribution of precipitation strengthening to yield strength;  $G$  is the shear modulus of the matrix;  $b$  is the Burgers vector of dislocations;  $f$  is the particle volume fraction and  $X$  is the average particle size. It is apparent that the increase in yield strength due to precipitate particles depends on the particle volume fraction and particle sizes. So, the contribution of precipitation strengthening to yield strength can be increased by reducing particle sizes by lowering the formation temperature or increasing particle volume percentages by increasing the amount of solute dissolved in austenite before transformation.

## 2.3 Other Considerations

### 2.3.1 Stored Energy

Stored energy in AHSSs, is generated from phase transformation from austenite to austenitic decomposition products (i.e., ferrite, bainite or martensite) [93] and following plastic deformation in the process of cold work [94–98], This stored energy is consumed by forming dislocation structures, i.e., shear bands, cell walls and cells [99] and can be later released by recovery, recrystallization and heat during annealing. So, the annealing performance is influenced by the amount and distribution of stored energy [100].

Previous studies attempted to investigate the methods of determining stored energy. Bever and Ticknor [94] first calorimetrically determined the stored energy of cold worked Au-Ag alloys. After Watson and O’Neil invented differential microcalorimeters [101], the application of differential scanning calorimetry (DSC) to the measurement of stored energy was studied in various metal and alloys, i.e., cold rolled Al-Fe alloy [102], Ni polycrystalline [103] and interstitial free (IF) steels [104]. In this method, internal plastic strain energy caused by cold work is released as heat and directly measured during annealing [102–104].

X-ray line broadening is another way of estimating the stored energy of deformed materials, since the lattice imperfection caused by plastic deformation gives rise to broadening of diffracting peaks of planes in Debye Scherrer X-ray patterns [105]. Paterson [96] used the X-ray line broadening method to evaluate the stored energy of deformed calcite, with the assumption that broadening was caused completely due to internal plastic strains. Later, a new X-ray line broadening approach was developed by Kallend and Huang to determine the orientation-dependent stored energy of 50% cold rolled copper [106]. Then, Rajmohan et al. [107] introduced a new

neutron diffraction line broadening method, which helped to determine a more accurate stored energy value of 80% cold rolled IF steels, since neutron diffraction can provide a deeper penetration into materials studied compared with X-ray diffraction.

In the 1960s, the study of Dillamore et al. [98] revealed that the orientation-dependent stored energy, following Shockley-Read low angle grain boundary (LAGB) energy formula [108,109], could be expressed by a function of sub-grain boundary misorientation. Based on this relationship between stored energy and sub-grain boundary misorientation, Choi et al. [99] utilized electron backscatter diffraction (EBSD) technology to calculate the average internal plastic strain energy stored in the sub-grain boundaries of 50% cold deformed IF steels. Subsequently, Fang et al. [100] investigated the determination of stored energy of Nb- or Ti- bearing high strength low alloy (HSLA) steels and they reported that, after cold rolling, the internal plastic strain energy was consumed by forming sub-grain boundaries within ferrite grains and causing the changes in ferrite grain shape, which means that the stored energy was supposed to be the sum of sub-grain boundary energy within ferrite and extra high angle grain boundary (HAGB) energy of elongated ferrite. Kernel average misorientation (KAM) is also another approach for characterizing the local misorientation of deformed crystalline lattices. It is defined as the average misorientation of a single point with regard to its neighbors within a kernel [110]. During the plastic deformation, statistically stored dislocations (SSDs) accumulate by random trapping, whereas geometrically necessary dislocations (GNDs) are stored, allowing for the compatible deformations, which are related to the gradients of deformations [111]. Calcagnotto et al. [112] showed that geometrically necessary dislocation density ( $\rho_{\text{GND}}$ ) could be calculated from KAM values. Therefore, stored energy can be expressed as the dislocation energy [113] with respect to EBSD-KAM.

### 2.3.2 Stretch-Flangeability

High strength DP steels have been widely used as vehicle body structures and anti-collision impact energy absorbing components, playing a crucial role in vehicle weight lightening. However, one important concern related to DP steels has arisen that increasing UTS of DP steels is considerably detrimental to sheet metal forming, i.e., stretch-flangeability or local ductility [114]. Stretch-flangeability normally is estimated by hole expansion testing [115], where a 100 mm × 100 mm sheet is cold punched with a 10 mm diameter hole, subsequently expanded by a conical punch at a constant rate, and the test is considered complete and final hole diameter measured when a through-thickness edge crack is observed. HER values are determined by the ratio of the difference between the final inner hole diameter (after hole expanding) and the initial inner hole diameter (before hole expanding) to the original inner hole diameter [115–118].

Many previous studies in the literature exist regarding the relationships between HER and uniaxial tensile properties (Fig. 2.9), such as YS [119], UTS [119,120], YS/UTS [116], strain hardening ratio ( $n$ ) [121], Post UE [119,120,122], normal anisotropy ( $\bar{R}$ ) [119,123], and reduction in area (RA) [27,29]. These correlations were often converted into linear or nonlinear regression equations to permit the prediction of HER values without actually conducting HETs. Figs. 2.9 (a)–(c) show the correlations between HER and UTS, Post UE as well as  $\bar{R}$ , based on Sadagopan's experimental works [124] and Basic Metal Processing Research Institute (BAMPRI) unpublished researches. Although the relationships between HER and tensile properties are apparent for some specific steels (i.e., the single phase ferritic steels or low strength steels), these relations are limited with respect to DP steels [120,125]. Therefore, other mechanical properties which might be related

to HER were studied. For example, Yoon et al. [125] found that fracture toughness played a crucial role in governing the stretch-flangeability of sheet metals.

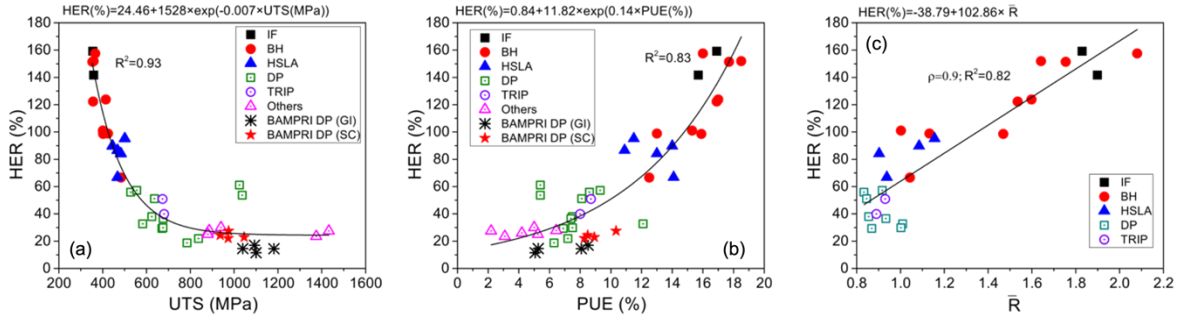


**Figure 2.9 (a) HER vs UTS, (b) HER vs Post UE and (c) HER vs  $\bar{R}$  for a variety of steel grades, data from Sadagopan’s experimental works [124] and BAMPRI unpublished research results.**

In addition, microstructural features have been reported to be related with HER. Gwon et al. [126] showed that grain refinement improved hole expansion behaviors of twinning induced plasticity (TWIP) steels. In the research of Kim et al. [127], it is reported that the a large amount of fresh martensite had a side effect on HER. Hasegawa et al. [128] pointed out that the hole expansion performance of DP 980 was dominated by the hardness difference between ferrite and fresh martensite. However, the limitation of their investigation was that the hardness values of different phases were calculated by experimental equations. Later, this finding was verified by Taylor et al. [33], who used nanoindentation technology to achieve the replacement of theoretical Vickers hardness by experimental nanohardness of both soft and hard phases.

Furthermore, the hole forming methods also have an influence on hole expansion performances of DP steels. Fig. 2.10 concludes four major steps of hole punching [129,130]: (1) a steel sheet blank is forced to fill into the clearance between the female die and male punch, forming a rollover zone in the shear surface (Fig. 2.10 (a)); (2) as the punch continues penetrating into the

tested metal, vertical walls on the edge of the punched hole metal can be observed, forming a burnished or ironing zone (Fig. 2.10 (b)); (3) internal stress increases with increasing the punch penetration depth and the tested metal is separated, when the internal stress reaches a critical value, forming a fracture zone (Fig. 2.10 (c)); and (4) a shear burr can be formed when the fracture surface is in contact with the punching die or the punch (Fig. 2.10 (d)). Thus, the initial punched hole surface normally consists of zones of rollover, burnishing, fracture and shear burrs. However, the effect of shear surface (i.e., the area percentage of individual zone) on HER is still being investigated.

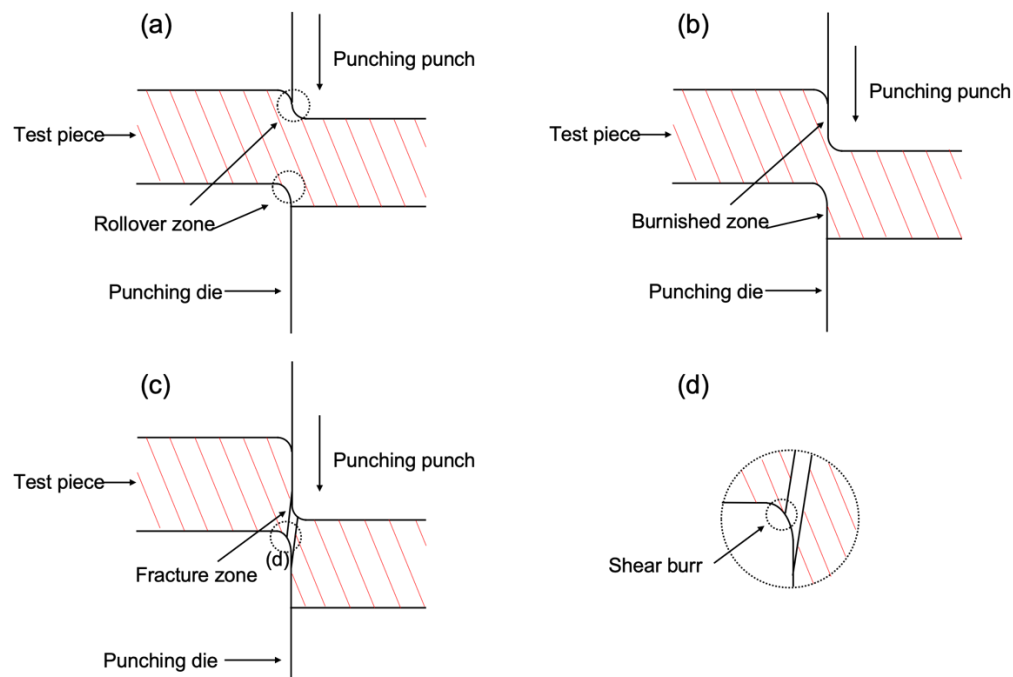


**Figure 2.10** The schematic illustration of punching process. The formation of (a) rollover zone, (b) burnished zone, (c) fracture zone and (d) shear burr [129].

In terms of other methods of making a hole, Yoon et al. [115] investigated the HER values of two kinds of initial holes. One was the punched hole and the other one was a hole milled after

punching. The HER results indicated that the HER blanks with the latter hole had the better hole expansion behavior, since the following milling process removed the punching damages [39,125,128,131–133]. Moreover, Taylor et al. [33] studied the sheared-edge ductility of hole edges formed by punching and electric discharge machining (EDM). In his study, no existence of sheared affected zone (SAZ) near the initial hole formed by EDM resulted in higher HER values. Sugimoto et al. [65] revealed the fact that the stretch-flangeability of high strength TRIP aided DP steels were remarkably improved by the combination of warm hole punching and subsequent warm hole expanding. In this case, the benefit to HER appeared to be caused by the carbon content or stability of the retained austenite instead of the volume fraction of the retained austenite. Chilutti [134], Skapik [135] and Cherry et al. [136] in BAMPRI studied effects of several common hole preparation methods (i.e., punching, laser cutting, water jet cutting and drilling) on the microstructures near initial hole edges and the HER results of DP590 and DP780 steels. Compared with another three methods, the HER specimens with the drilled holes in the center had the best hole expansion performances, since they had the reasonable edge quality without damages caused by punching, heat affected zones caused by laser cutting or non-uniform holes caused by water jet cutting [134,135]. Additionally, in Cherry et al.'s research [136], two post-punching approaches (in-hole and above-hole induction heating) were applied, and the results showed that the HER values of DP980 HER specimens with in-hole induction heating was improved from 16.3% can reach 108.6%.

Regarding the fracture mechanism occurring during the hole expansion of DP steels with a variety of strength levels, both Hasegawa et al. [128] and Levy et al. [131] found that microcracks always existed in the ferrite-martensite interfaces during HETs, while some cracks still propagated inside the ferrite or martensite grains, when considering some high stretch-frangibility DP steels.

Furthermore, Pathak et al. [39] concluded four void nucleation mechanisms for DP 780 steels. Martensite cracking and the decohesion of ferrite/martensite interface were two dominant void nucleation mechanisms, while some voids were also found at the ferrite/ferrite grain boundaries near the final fracture and a few voids were associated with the presence of TiN particles at a low strain [39].

### 3.0 Motivation and Objectives

The current study will investigate how to further increase the strength of DP steels, while not severely sacrificing ductility and HER. The following key questions will be addressed:

- (i) What final microstructure is needed to reach a high UTS (i.e., 1000 MPa) in DP steels?
- (ii) How to obtain these critical microstructures after contiguous galvanizing line (CGL) simulations by the changes in composition and processing?
- (iii) What is the acceptable HER value for high-strength DP steels?
- (iv) What are the key factors governing hole expansion?

This research focuses on processing, microstructures and properties of a new generation of DP steels produced on continuous galvanizing lines. There are several program variations that need to be taken into consideration.

- (i) In terms of alloy design, 0.15 wt.% C, 0.04/ 0.4/ 0.8 wt.% Al and 0.06/ 0.12 wt.% V was assessed.
- (ii) The pre-annealing conditions including two coiling temperatures (580°C and 677°C) and a 60% cold reduction were chosen.
- (iii) The effects of two annealing approaches, a simulation of standard galvanizing and a simulation of a novel supercooling process on the structures and properties of DP steels were compared.

## 4.0 Operating Hypotheses

(i) Both global ductility (i.e., total elongation) and local ductility (i.e., hole expansion ratio) of the candidate DP steels can be improved by the changes in composition and processing.

(ii) HER test includes hole punching and hole expansion. Knowledge of the defects formed during hole punching, their growth during hole expansion, and the influence of microstructure in these two steps are critical for improving HER.

(iii) HER values are related to the differences in hardness between ferrite and hard constituents. Possibilities of improving HER include strengthening ferrite and softening martensite.

## 5.0 Experimental Procedures

### 5.1 Materials and Processing

The candidate DP steels used in this dissertation were supplied by United State Steel Research and Technology Center. The measured compositions are listed in Table 5.1. The designations or IDs of laboratory heats are composed of three digits. The first digit specifies the Al-addition contents (L is for 0.04 wt.% Al, M for 0.4 wt.% Al and H for 0.8 wt.% Al). The second digit is used to describe the V content (L is for 0.06 wt.% V and H for 0.112 wt.% V). Finally, the last one represents the coiling temperatures (L is for a low coiling temperature of 580°C and H for a high coiling temperature of 677°C).

**Table 5.1 Measured chemical compositions (wt. %) and IDs of candidate DP steels**

IDs	C	Al	Cr	Mn	Ni	Si	V	N
LL	0.153	<b>0.040</b>	0.504	2.015	0.010	0.414	<b>0.061</b>	0.0046
LH	0.153	<b>0.042</b>	0.503	2.020	0.010	0.415	<b>0.117</b>	0.0042
ML	0.153	<b>0.394</b>	0.510	2.042	0.010	0.427	<b>0.062</b>	0.0048
MH	0.152	<b>0.394</b>	0.510	2.035	0.010	0.426	<b>0.115</b>	0.0047
HL	0.147	<b>0.800</b>	0.503	2.019	0.014	0.418	<b>0.061</b>	0.0047

Note: the embolden values reflect the variables in Al or V contents

Figure 5.1 schematically illustrates the thermomechanical processing and heat treatments used in this dissertation. Concerning thermomechanical processing, after vacuum melting and solidification in cast iron molds, the ingots were first reheated to 1250°C and hot rolled to 25 mm.

In the wake of rough rolling, the steels were soaked again at 1250°C, then immediately further hot rolled to 5 mm with several passes, ~27.5% hot reduction for each pass, then cold water sprayed to two coiling temperatures (677°C or 580°C) from 920°C, followed by in-coil cooling simulated by cooling to room temperature at  $-30^{\circ}\text{C h}^{-1}$ . After surface grinding and 60% cold rolling to 1.2 mm, the cold rolled steel sheets were given two CGL simulations, by using a Gleeble 3800 machine. One CGL simulation replicated standard galvanizing (denoted by GI) and the other one was called supercooling process (denoted by SC), which will be described in the following content, Fig. 5.1.

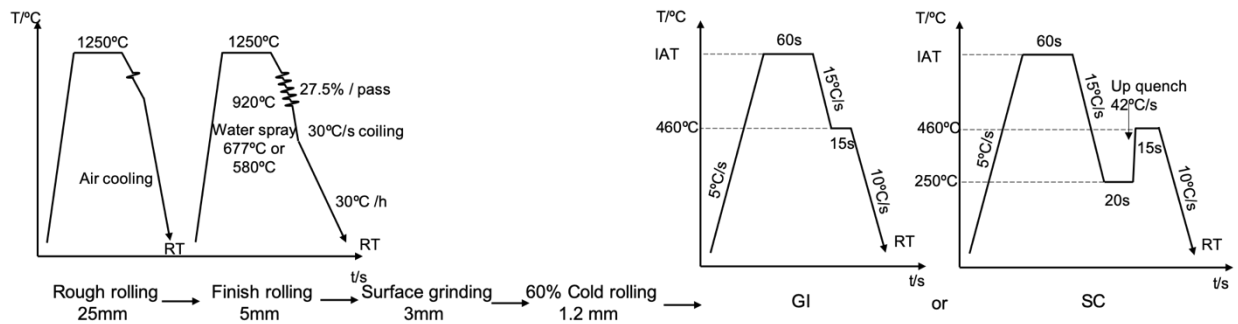


**Figure 5.1 Schematic illustration of thermomechanical processing and heat treatments used in this dissertation**

In order to obtain ultra-high strength, it is known that a large amount of fresh martensite should be observed in the final microstructures of DP steels. Previous researchers [9,27,52,53] found that intercritical annealing temperatures (IATs) played a critical role in controlling the volume fraction of fresh martensite in dual-phase microstructures. The  $AC_3$  line at the top of the intercritical region, together with the inverse lever rule, mean that for a given carbon content, higher annealing temperatures will mean more austenite in the two-phase mixture, but at a lower carbon content of this austenite. This means lower hardenability or stability and less chance of minimizing higher temperature transformation to new ferrite, pearlite or bainite during slow cooling for example from the IAT, near 800°C to the zinc pot temperature near 460°C. Additionally,

Al is one of the ferrite stabilizer elements, which can increase  $A_{C1}$  and  $A_{C3}$  temperatures and enlarge both the  $\alpha$  phase field and the intercritical  $\gamma+\alpha$  region of the Fe-Fe<sub>3</sub>C phase diagram [20]. Therefore, higher IATs must be used for high Al-bearing DP steels to obtain similar initial austenite as the low Al-bearing DP steels. So, prior to CGL simulations, optimum IAT experiments needed to be conducted. The steels with different Al contents were heated to distinct IATs, ranging from 760°C to 820°C and water quenched to room temperature (WQRT). The volume fraction of fresh martensite for each condition was measured and recorded in Table 5.2. Fig. 5.2 shows the fresh martensite percentages of DP steels with different Al levels varying with IATs. From previous experience [27], about 10%–15% austenite transforms into ferrite or bainitic microstructures during full CGL simulations. So, 780°C, 800°C and 820°C were selected as the optimum IATs of candidate DP steels containing 0.04 wt.%, 0.4 wt.% and 0.8 wt.% Al contents, respectively.

As shown in Fig. 5.1, GI and SC anneals have some similar heat treatments in the early stage of CGL simulations. The cold rolled steel sheets were heated to the desired IATs, varying with Al contents (as shown in Table 5.2 and Fig. 5.2), at  $+5^{\circ}\text{C s}^{-1}$  and isothermally soaked for 60 s, after which the specimens of each steel conditions were divided into two groups and each group was given different succeeding heat treatments of GI or SC anneals. One group was immediately cooled to the zinc pot temperature of 460°C at  $-15^{\circ}\text{C s}^{-1}$ , held 15s, followed by cooling to room temperature at  $-10^{\circ}\text{C s}^{-1}$ . The other group of steel conditions were cooled to 250°C at  $-15^{\circ}\text{C s}^{-1}$ , up-quenched to 460°C at  $+42^{\circ}\text{C s}^{-1}$ , soaked for 15s and later cooled to room temperature at  $-10^{\circ}\text{C s}^{-1}$ .

**Table 5.2 Martensite volume fraction (%) of DP steels with different Al levels at distinct IATs in DP steels fully processed in CGL simulations**

IDs	Al (wt.%)	V (wt.%)	Fresh martensite volume fraction (%)						
			760°C	770°C	780°C	790°C	800°C	810°C	820°C
LL	0.04	0.06	65.0	74.5	<b>84.9</b>	92.5	-	-	-
ML	0.4	0.06	-	59.3	67.0	73.4	<b>82.5</b>	-	-
HL	0.8	0.06	-	41.9	57.4	65.2	72.9	78.7	<b>86.1</b>

Note: the embolden values were selected for further studies.

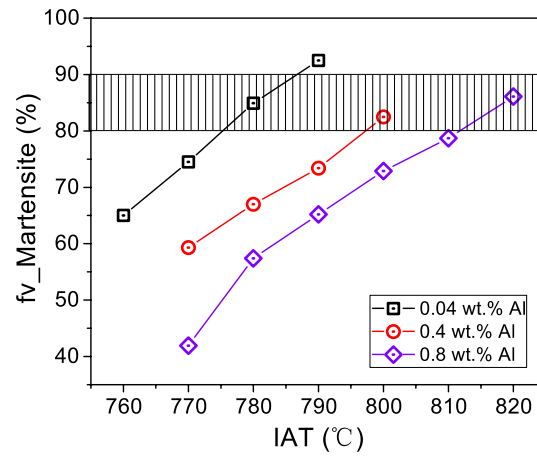


**Figure 5.2 The volume fractions of martensite for steels with different Al levels at distinct IATs. The selection of IAT for each Al content resulting in 80-90 Vol % fresh martensite**

## 5.2 Stored Energy Evaluation <sup>1</sup>

### 5.2.1 Material Characterizations

The hot rolled and cold rolled steel specimens with different pre-annealing conditions were sectioned, mounted, ground, polished and etched with 2% Nital reagent, in the preparation for the examination with a Nikon optical microscopy (OM).

In EBSD analysis, inferior surface condition may affect the local strain measurements of materials studied. So, one additional step of final vibratory polishing with 0.05  $\mu\text{m}$  alumina suspension became highly critical for EBSD sample preparation. The automated collection of EBSD data was conducted by using a FEI Scios dual beam scanning electron microscopy (SEM) combined with a EDAX EBSD detector and the fixed operating parameters, i.e., an accelerating voltage of 20kV, the current of 13 nA, the working distance of 14 mm, a low magnification of 1000 $\times$ , and the step size of 100 nm. Later, the EBSD data were analyzed via OIM Analysis<sup>TM</sup> v8 software.

---

<sup>1</sup> Much of this section appears in print: Adapted by permission from Springer Nature Customer Service Centre GmbH: Springer Nature, Metall. Mater. Trans. A., Ref. [99] Stored energy evaluation for high strength dual-phase steels with different pre-annealing conditions, Y. Wu, J. Uusitalo and A.J. DeArdo, © 2020 Springer Nature Switzerland AG.

## 5.2.2 Vickers Hardness Measurements

The Vickers hardness testing of the hot rolled and cold rolled DP steels was conducted with a load of 300gf and a dwell time of 15s, using a LECO LM310AT hardness tester, on the highly polished sample surface. The mean Vickers hardness of each steel condition was calculated by averaging the hardness values of 10 random indents.

## 5.2.3 Stored Energy Evaluation Methods with EBSD Technology

Three methods of determining the stored energy values of the initial conditions prior annealing were investigated in this dissertation, by applying EBSD technology.

The first method is the sub-grain method, which is associated with the sub-grain structures in the deformed grain centers [99]. So, this dislocation-related stored energy can be calculated in Eq. 5.1 [137],

$$SE_d = \frac{k\gamma_s}{d} \quad (5.1)$$

where, k is the geometric constant (k=3 [137]),  $\gamma_s$  the sub-grain boundary energy and d the average sub-grain size. Eq. 5.2 can be shown below, as both sides of Eq. 5.1 are divided by the maximum grain boundary energy  $\gamma_m$ ,

$$\frac{SE_d}{\gamma_m} = \frac{k}{d} \left( \frac{\gamma_s}{\gamma_m} \right) \quad (5.2)$$

Since, the sub-grain boundary energy  $\gamma_s$  can be expressed by a function of grain boundary misorientation [98], according to the Shockley-Read LAGB energy relation [108,109],  $\gamma_s$  can be given in Eqs. 5.3 and 5.4 [99,109],

$$\gamma_s = \gamma_m \frac{\theta}{\theta_m} \left[ 1 - \ln \left( \frac{\theta}{\theta_m} \right) \right], \text{ if } \theta < \theta_m \quad (5.3)$$

$$\gamma_s = \gamma_m, \text{ if } \theta \geq \theta_m \quad (5.4)$$

where,  $\theta_m$  is the usual limit for the low angle grain boundary misorientation in OIM packages ( $\theta_m = 15^\circ$ ).  $\gamma_m$  is the special boundary energy for HAGBs ( $\gamma_m = 7.56 \text{ J m}^{-2}$  [100]). Note:  $\gamma_s = 3.95 \text{ J m}^{-2}$  when  $\theta = 3^\circ$ , a frequently used figure for the definition of sub-grain boundary misorientation using dislocation models [138]. It should be noted that the sub-grain boundary energy is dependent upon the sub-grain boundary misorientation, which relies upon two things: the sub-grain size and the measurement method. The cell size depends on the growth as it approaches the critical size for the nucleation of recrystallization. Since the annealing time in the CGL is limited, neither the cells themselves nor the wall misorientation would be expected to be large. Concerning the measurement method, the standard OIM packages use a cut-off of  $15^\circ$  as the demarcation between low and high angle boundaries. However, dislocation boundaries directly observed in the TEM show misorientations below about  $6^\circ$ . Obviously, the choice between  $6^\circ$  and  $15^\circ$  will have a large influence on the calculated stored energy values. It is believed that  $6^\circ$  is more valid, so  $\theta = 6^\circ$  was utilized in this research. Therefore,  $\gamma_s = 5.79 \text{ J m}^{-2}$  when  $\theta = 6^\circ$ , the upper limit of sub-grain boundary misorientation using dislocation models [139].

Image Quality or IQ is an essential parameter of EBSD technology, which is used for describing the quality of electron backscatter Kikuchi patterns generated from a large volume of diffraction within the materials studied [140,141]. It is defined as the average of the total heights of peaks detected by Hough Transform, as shown in Eq. 5.5 [142],

$$IQ = \frac{1}{N} \sum_{i=1}^N H_i(\rho_i, \theta_i) \quad (5.5)$$

where, N is the total number of the peaks,  $H_i$  ( $\rho_i$  and  $\theta_i$ ) the height of the  $i$ th peak with a specific location associated with the Hough Transform. IQ values are assumed to have a positive linear relationship with local strain or dislocation density [99,141,143]. So, the correlation between stored energy and the reconstructed IQ is given in Eq. 5.6,

$$SE_d \propto IQ = \left( 1 - \frac{IQ_i - IQ_{\min}}{IQ_{\max} - IQ_{\min}} \right) \times 10 \quad (5.6)$$

where,  $IQ_i$  is the IQ value of the  $i$ th diffracted site,  $IQ_{\min}$  and  $IQ_{\max}$  the minimum and maximum IQ values, respectively.

In the EBSD analysis, KAM is another approach of determining local misorientation [112,144]. EBSD-KAM technology calculated the average misorientation of all the surrounding points with respect to the center point within a defined kernel. The definition of KAM is also given in Eq. 5.7 [144],

$$KAM = \frac{1}{N} \sum_{i=1}^N \theta_i \quad (5.7)$$

where, N is the total number of surrounding points within a kernel and  $\theta_i$  the misorientation of ith surrounding point with respect to the center point.

In Ashby's research on plastic deformation of non-homogeneous materials, two dislocation densities were involved, one was statistically stored dislocations (SSDs) and the other one geometrically necessary dislocations (GNDs) [111]. SSDs evolved from random trapping [111,145] and GNDs was related to the plastic strain gradients and geometrical constrains to lattice crystals [111,146] during uniform plastic deformation. So, the geometrically necessary dislocation density ( $\rho_{\text{GND}}$ ) can be expressed as a function of local misorientation, by using KAM technology, shown in Eq. 5.8 [112,144],

$$\rho_{\text{GND}} = \frac{2\theta}{Xb} \quad (5.8)$$

where,  $\theta$  is the KAM value in radians, X the unit length and b the Burgers vector and equivalent to 0.248 nm. The stored energy evaluated with KAM method can be expressed by Eq. 5.9 [113],

$$\text{SE}_d = \frac{1}{2} G \rho_{\text{GND}} b^2 \quad (5.9)$$

where, G is shear modulus ( $G=82\text{GPa}$  [147]).

The last three methods mentioned above were used for the evaluation of stored energy in the dislocation structures within deformed grains. While the energy stored in the HAGB can be calculated by Eq. 5.10 [100],

$$\text{SE}_{\text{HAGB}} = 7.56 \times S_V \times 10^{-5} \quad (5.10)$$

where,  $S_V$  is the HAGB area per unit volume, which can be given in Eqs. 5.11 and 5.12 [148],

$$S_V = 2N_L, \text{ for hot rolled steels} \quad (5.11)$$

where,  $N_L$  is the intercept number per unit length.

$$S_V = 0.429 (N_L)_{\parallel} + 1.571 (N_L)_{\perp}, \text{ for cold rolled steels} \quad (5.12)$$

where,  $(N_L)_{\parallel}$  and  $(N_L)_{\perp}$  are the intercept numbers per unit length along RD and normal direction (ND), respectively.

The total stored energy ( $SE_{tot}$ ) is taken to be the sum of the energy stored in the sub-grain boundaries ( $SE_d$ ) and HAGBs ( $SE_{HAGB}$ ), which is given in Eq. 5.13

$$SE_{tot} = SE_d + SE_{HAGB} \quad (5.13)$$

### 5.3 Austenite Formation Studies with Al Contents

#### 5.3.1 Annealing Stimulations

In order to investigate the effect of Al on austenite formation during heating and isothermal holding during intercritical annealing, special heat treatments were applied in this study.

Fig. 5.3 shows the schematic heat treatment used to study the austenite formation in steels with different Al contents, which was stimulated in an MTS 458 system with a quartz filament furnace. The cold rolled steels were reheated to the 740°C, 770°C and 800°C at  $+5^{\circ}\text{C s}^{-1}$ . After

isothermal holding for 5s, 15s, 30s, 60s, 180s, 600s, 1800s and 3600s, the samples were water quenched to room temperature. Since all the intercritically formed austenite is assumed to transform to martensite by water quenching, the martensite volume percentage ( $f_m$ ) is supposed to equal to the volume fraction of intercritically formed austenite ( $f_\gamma$ ). The values of  $f_\gamma$  in different conditions were measured and recorded. Also, the equilibrium fraction of austenite at different annealing temperatures was determined by the fraction of austenite of the samples with the 3600s holding time.

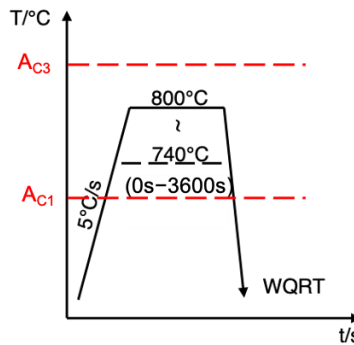


**Figure 5.3** The schematic illustration of austenite formation studies of steels with different Al contents

### 5.3.2 Material Characterizations

The water-quenched specimens were sectioned, mounted, ground, polished and etched with 2% Nital etchant. The microstructures of these samples were characterized by a FEI Apreo SEM at an accelerating voltage of 20 kV and a spot sized of 15. The fraction of martensite was determined by using manual pointing counting method from ASTM E562-19 [149]. The SEM images of randomly selected three positions in each sample were selected for martensite fraction determination. Each SEM micrograph was covered with an array of  $20 \times 20$  (400 in total) points formed by a grid, and the number of points falling in the martensite area was counted and recorded.

## 5.4 Microstructure – Property Relationship Study

### 5.4.1 Mechanical Testing

The sub-sized dogbone-like tensile test specimens were machined from the fully annealed DP steels with the dimensions of 1.2 mm thickness, 6 mm gage width and 10 mm gage length along the transverse direction (TD), following ASTM E8-16 [150]. Uniaxial tensile tests were conducted by a ZwickRoell Z100 tensile tester, at a strain rate of  $10^{-4} \text{ s}^{-1}$ .

## 5.5 Stretch-Flangeability Investigation <sup>2</sup>

### 5.5.1 Hole Expansion Testing

The hole expansion tests are primarily used in dissertation to help determine the sheared edge cracking resistance of the candidate DP steels. It was performed in accordance with ISO 16630 [151], by using a BAMPRI hole expansion tester reconstructed from a Tinius Olsen formability test machine equipped with conical punch, dies, camera, video output and power supply [152,153].

From the requirements of ISO 16630, the tested materials should be machined into the HER blanks in the dimension of 100 mm × 100 mm × thickness with a 10-mm-diameter central

---

<sup>2</sup> Much of this section appears in print: Adapted from the article published in Ref. [130], Mater. Sci. Eng. A, Volume 797, Yingjie Wu, Juha Uusitalo, Anthony J. DeArdo, Investigation of effects of processing on stretch-flangeability of the ultra-high strength, vanadium-bearing dual-phase steels, 140094, © 2020 Elsevier B.V.

hole. However, the candidate DP steels in this study were given two CGL simulations conducted by a Gleeble 3800 machine. The largest dimensions of the Gleeble blanks are 100 mm in length  $\times$  80 mm  $\times$  thickness with a 30-mm-diameter heated zone in center. From previous BAMPRI experimental results, HER values were not importantly affected by the dimensions of HER blanks. So, the HER blanks with the dimension of 100 mm in length  $\times$  80 mm in width  $\times$  1.2 mm in thickness were applied in this study.

Fig. 5.4 displays the entire procedure of hole expansion testing, including hole punching, shearing and expansion. In the process of shearing, the 10-mm-diameter punched hole was expanded by a conical punch at a constant rate of ( $\sim 3 \text{ mm mm}^{-1}$ ), and the test was considered complete and final hole diameter measured when a through-thickness edge crack was observed. HER is defined by Eq. 5.14 [151],

$$\text{HER} = \frac{D_f - D_o}{D_o} \quad (5.14)$$

where,  $D_o$  and  $D_f$  are diameters of initial and final holes, respectively.

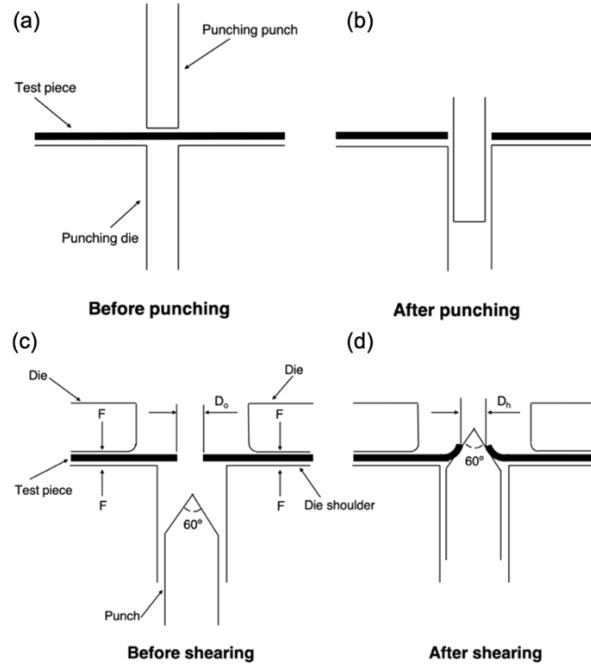


**Figure 5.4** The schematic process of hole expanding (a) before hole punching, (b) after hole punching, (c) before shearing and (d) after shearing [151].

### 5.5.2 Microstructural Observation after Hole Punching

The microstructural damages caused by hole punching are reported to have effects on hole expansion performances of AHSSs [29,117,125]. In the present study, the HER blanks with the initial punched hole were sectioned. Two critical areas, the initial punched hole and the shear affected zone (SAZ) near the initial punched hole shear edge, as seen in Fig. 5.5 were examined by a FEI Apreo SEM at an accelerating voltage of 20 kV and a spot sized of 15. Prior to SEM characterization, the initial punched hole area was ultrasonically cleaned by alcohol to remove dirt, oil and debris caused by cutting and SAZ was sectioned, mounted, ground, polished and etched by 2% Nital etchant.

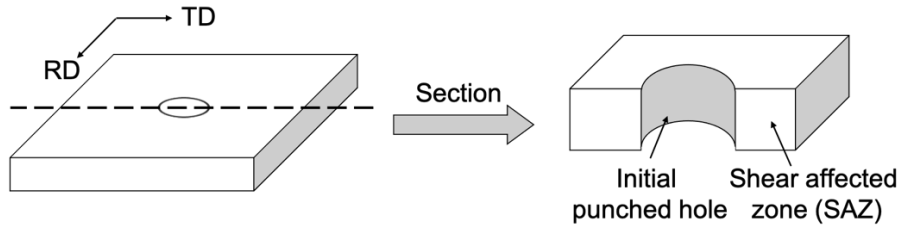


**Figure 5.5 Positions for SEM characterization**

### 5.5.3 Local Internal Plastic Strains Study

Punching damages still can be quantified as plastic strains for fully annealed DP with both GI and SC anneals. Thus, the internal plastic strains introduced in the SAZ near the initial punched hole shear edges were examined by EBSD and nanoindentation technologies. Fig. 5.6 shows the different positions in the SAZ near the initial punched hole sheared edges.

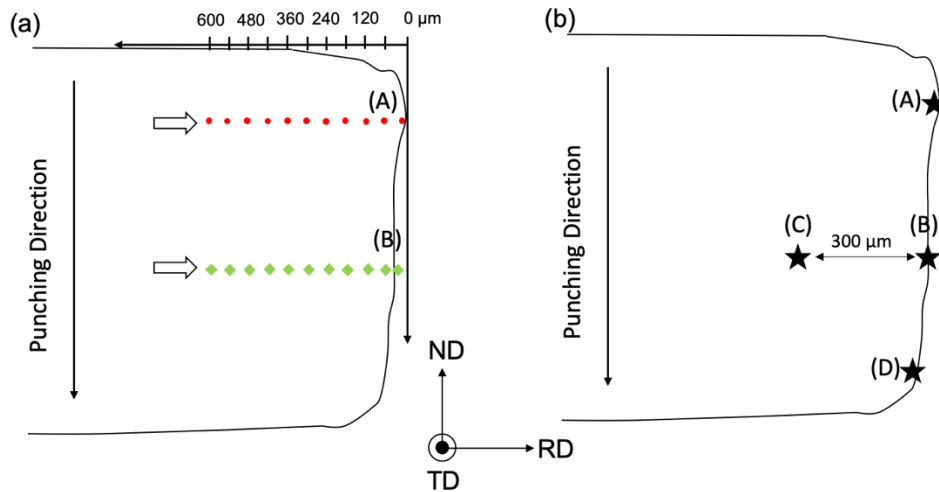


**Figure 5.6 Positions for the examination of internal plastic strains caused by hole punching with (a) EBSD-KAM and (b) nanoindentation technologies**

EBSD-KAM method is one of the most effective way to measure the local misorientations illustrating internal plastic strain distributions, i.e., local dislocation density, introduced by the step

of hole punching. In this method, the local misorientation is calculated by averaging all misorientations of spots with respect to the center spot within a kernel [110]. KAM values are considered to reflect the geometrically  $\rho_{\text{GND}}$  associated with the plastic deformation gradients [112]. So, with this consideration, the local misorientations of the areas in the distance of 0–600  $\mu\text{m}$  from position A (near the burnished and fracture transition zone) and position B (near the middle of fracture zone), as seen in Fig. 5.6 (a), were assessed by a FEI Scios dual beam SEM combined with a EDAX EBSD detector and the fixed operating parameters, i.e., an accelerating voltage of 20kV, the current of 13 nA, the working distance of 14 mm, a magnification of 2000 $\times$ , and the step size of 100 nm. KAM values were analyzed by using OIM Analysis<sup>TM</sup> v8 software. Additionally, the correlation between KAM results and local equivalent strains ( $\epsilon_{\text{eq}}$ ) was given in Eq. 5.15 [154], by combining EBSD-KAM and digital image correlation (DIC) methods.

$$\text{KAM (rad)} = \frac{\pi}{180} \times 1.68 \epsilon_{\text{eq}}^{0.44} \quad (5.15)$$

So, given KAM values, the results of  $\epsilon_{\text{eq}}$  can be expressed by Eq. 5.16,

$$\epsilon_{\text{eq}} = \sqrt[0.44]{\frac{\text{KAM (}^\circ\text{)}}{1.68}} \quad (5.16)$$

In the wake of hole punching, both ferrite and hard constituents in SAZs near the initial punched hole sheared edges would be sheared, introducing lattice defects by plastic deformation, leading to the increase in hardness. So, nanoindentation is another useful way of quantifying the damages caused by hole punching. As shown in Fig. 5.6 (b), the nanohardness values of both ferrite and hard constituents (fresh martensite in the GI annealed DP steels or tempered martensite in the fully annealed DP steels with SC anneal) were determined in four test positions. Positions A and

B were described above. Position C is the area, 300  $\mu\text{m}$  away from Position B, and position D is the bottom of the fracture zone. An array of  $5 \times 5$  (25 in total) of indentations were performed, by using a Hysitron TI900 Triboindenter, on the final polished surface for each position with a load of 2000  $\mu\text{N}$ , and the distance between each indentation was 6  $\mu\text{m}$  to avoid the potential effect of overlapping plastic zones. The nanoindentation results were determined by applying the Oliver-Pharr method [155]. The microstructures with 25 nano-indenters in each tested position were revealed by a 2% Nital etching reagent and observed via SEM.

#### 5.5.4 Micro-Fracture Mechanism Study

In order to study the micro-mechanism of fracture occurring in the punched hole surfaces of HER blanks during HET, incomplete or partial HETs were conducted. HER blanks of one selected condition, with the dimensions of 100 mm  $\times$  80 mm along with a 10 mm diameter punched hole in the center, were tested with the HER values of 0%, 5%, 10%, 15% and 25%. One half of the final hole surfaces along the TD of HER samples (Figure 5.7) with different HERs were cut and ultrasonically cleaned in ethanol to remove oil, iron debris particles and dust inadvertently added during cutting, followed by observing via SEM.

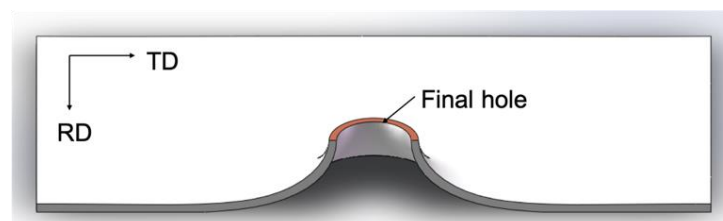


Figure 5.7 The schematic illustration of final hole surface (highlighted in orange color) after hole expanding.

## 6.0 Stored Energy Evaluation <sup>3</sup>

### 6.1 Results

#### 6.1.1 The Microstructures of the Starting Conditions

In examining the microstructures of the starting conditions prior to intercritical annealing, it is essential to make appropriate phase identification as well as microstructural features of both hot band coils and cold rolled sheet steels. So, OM imaging was applied to assess the samples with different pre-annealing conditions (i.e., Al, V contents and coiling temperatures).

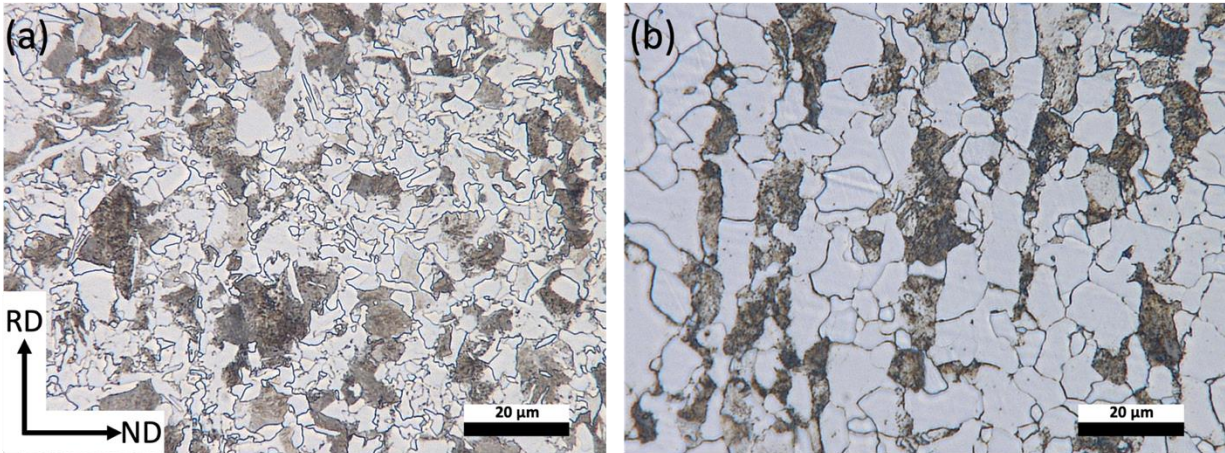
As shown in Figure 6.1 (a) is the OM micrograph of the steel condition the LLL HB (0.04Al-0.06V-CT580°C), consisting of ferrite and pearlite. The ferrite matrix is comprised of polygonal and acicular ferrite morphologies. Additionally, the banded polygonal ferrite-pearlite mixture is observed in the OM micrograph of the steel condition of LLH HB (0.04Al-0.06V-CT677°C), as seen in Fig. 6.1 (b).

Table 6.1 lists the microstructural characteristics of the hot band coils studied. From Table 6.1, pearlite volume percentages of different steel conditions range from 24.1% to 41.1%. Fig. 6.2 presents the effects of Al and V contents along with coiling temperatures on average ferrite grain size, based on the data in Table 6.1. The findings in Fig. 6.2 show that the 0.4 wt.% Al-bearing

---

<sup>3</sup> Much of this section appears in print: Adapted by permission from Springer Nature Customer Service Centre GmbH: Springer Nature, Metall. Mater. Trans. A., Ref. [99] Stored energy evaluation for high strength dual-phase steels with different pre-annealing conditions, Y. Wu, J. Uusitalo and A.J. DeArdo, © 2020 Springer Nature Switzerland AG.

steel conditions have the finest-grained ferritic microstructure, among other Al contents. V contents slightly coarsen ferrite grain sizes. Also, ferrite grain sizes increase with the increase in coiling temperature from 580°C to 677°C.



**Figure 6.1** The OM micrographs of the hot rolled steels of steel conditions: (a) LLL HB (0.04Al-0.06V-CT580°C) and (b) LLH HB (0.04Al-0.06V-CT677°C).

Fig. 6.3 displays the cold rolled microstructures of steel conditions of LLL CR (0.04Al-0.06V-CT580°C) and LLH CR (0.04Al-0.06V-CT677°C). In these two conditions, both ferrite grains and pearlite colonies are deformed and elongated along the rolling direction (RD). In contrast to coarse, deformed polygonal ferrite observed in the candidate DP steels with a high coiling temperature of 677°C, the ferrite grains are compacted so tightly that the ferrite grain boundaries are barely visible for the steel condition coiled at 580°C. In addition, after cold rolling, a large amount of cementite is found located at the deformed ferrite grain boundaries in the OM micrographs of the cold rolled steels with a CT of 580°C.

**Table 6.1 Microstructural features (i.e., ferrite grain size ( $d_\alpha$ ), ferrite volume fraction ( $f_{V(\alpha)}$ ) and pearlite volume fraction ( $f_{V(P)}$ ) of hot rolled steels**

IDs	$d_\alpha$ ( $\mu\text{m}$ )	$f_{V(\alpha)}$ (%)	$f_{V(P)}$ (%)
LLL HB	5.57±3.08	69.3	30.8
LLH HB	8.70±4.17	71.5	28.5
LHL HB	5.68±3.47	74.3	25.7
LHH HB	9.22±4.56	67.7	32.3
MLL HB	4.44±2.79	61.7	38.3
MLH HB	6.08±3.58	58.9	41.1
MHL HB	5.06±3.40	71.1	28.9
MHH HB	6.71±3.92	65.5	34.5
HLL HB	5.22±3.34	68.5	31.5
HLH HB	7.66±3.58	75.9	24.1

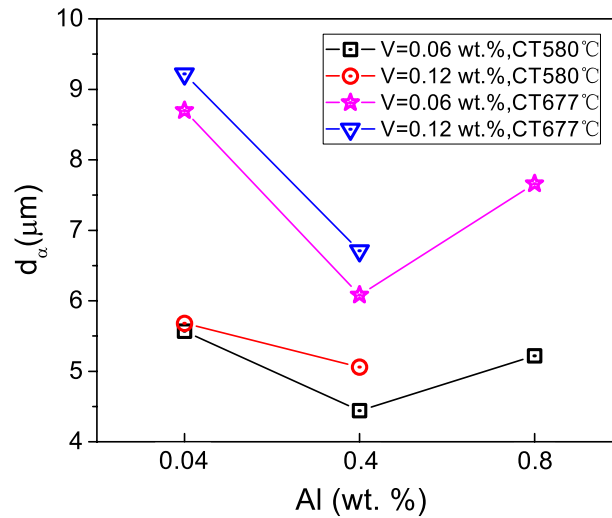


**Figure 6.2 Effects of Al and V additions and coiling temperatures on ferrite grain sizes of hot band coils**

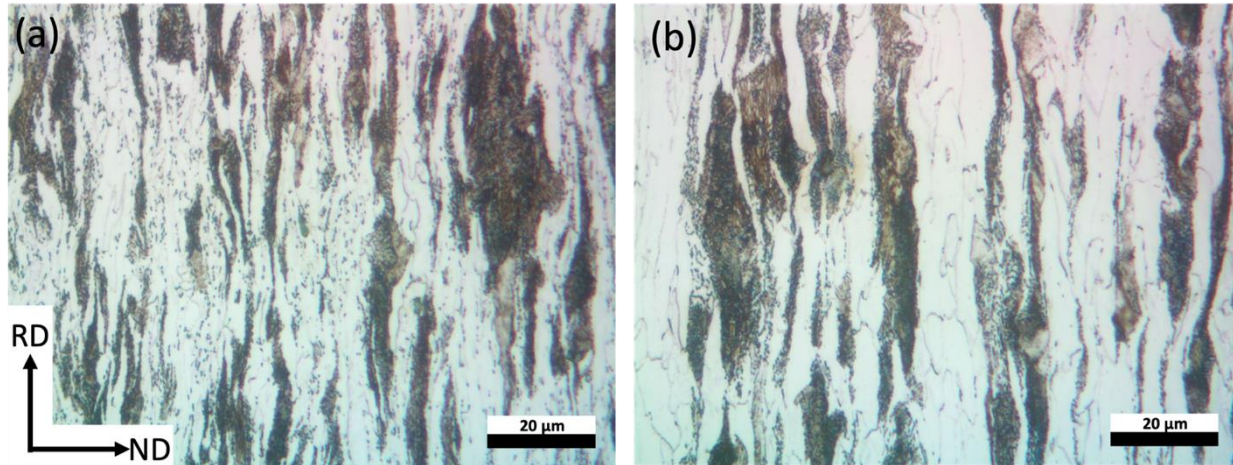


Figure 6.3 OM micrographs of cold rolled steel sheets of steel conditions: (a) LLL CR (0.04Al-0.06V-CT580°C) and (b) LLH CR (0.04Al-0.06V-CT677°C).

### 6.1.2 Microstructural Analysis with EBSD Technology

EBSD is one of the mainstream materials characterization technologies used for providing information associated with crystallographic orientation, grain size and grain boundary misorientation, and local strain of materials studied [141,156]. Figure 6.4 displays the EBSD mappings (i.e., image quality (IQ), inverse pole figure (IPF), KAM and  $SE_{\text{sub-grain}}$ ) of HLL (0.8%Al-0.06%V-CT580°C) and HLH (0.8%Al-0.06%V-CT677°C) with both hot rolled and cold rolled conditions.

Figs. 6.4 (a)–(d) show the EBSD-IQ maps of steel conditions of HLL HB, HLL CR, HLH HB and HLH CR. EBSD-IQ maps are generated from electron backscattered diffraction patterns and the contrast in maps are mainly caused by internal strains [142,157] due to the difference in dislocation density. In IQ maps, the light gray area reveals the low strain region with low dislocation density, while the dark gray area represents high strain region with high dislocation density. Also, the black lines denote the HAGBs ( $>15^\circ$ ). From Fig. 6.4 (a), the microstructure of

HLL HB (CT580°C) predominantly consists of acicular ferrite and refined polygonal ferrite with a higher strain contrast, resulting a lower IQ value, since acicular ferrite transforms from a low coiling temperature (580°C in this study) with a high dislocation density. While, the strain contrast and IQ value are much lower in Fig. 6.4 (c), the IQ map of HLH HB (CT677°C), and this steel condition is characterized by a large amount of coarse polygonal ferrite. The transformation of coarse polygonal ferrite is at a high coiling temperature (677°C in this study) with a low dislocation density. So, the dislocation density differences in acicular ferrite and polygonal ferrite result in different strain contrasts and IQ values. Regarding the IQ maps of the cold rolled steel conditions, much higher strain contrast is observed in Fig. 6.4 (b) and (d), which is due to considerable lattice defects, mainly dislocations were introduced by plastic deformation (i.e., 60% cold reduction in this study).

The EBSD-IPF maps of steel conditions of HLL HB, HLL CR, HLH HB and HLH CR with a unit triangle showing the color code for the crystallographic orientation of ferrite grains are displayed in Figs. 6.4 (e)–(h). Different colors show different orientation, i.e., red, blue and green denote {001}, {011} and {111} lattice planes, respectively, with respect to the rolling direction (RD).

Figs. 6.4 (i)–(l) provide the color coded EBSD-KAM maps of steel conditions of HLL HB, HLL CR, HLH HB and HLH CR. In EBSD analysis, local misorientation denotes the strain distribution of the metal and alloys studied [110,158], and KAM is the one of the most useful approaches. In this method, for any spot in the kernel for square grids, its misorientation is calculated by averaging the misorientations of all the spots within the kernel. In these KAM maps, the color distribution represents the local strain distribution of the samples [110] with different pre-annealing conditions, which is in agreement with the strain contrast shown in EBSD-IQ maps.

Cold colors (blue and green) and warm colors (yellow, orange and red) represent low internal strains (or low dislocation density) and high internal strains (or high dislocation density), respectively. The results indicate that a higher internal plastic strain or dislocation density can be observed for the steel condition of a low coiling temperature of 580°C combined with 60% cold reduction.

The stored energy distribution is exhibited by the intensity of red color shown in EBSD- $SE_d$  maps, applying sub-grain method, as seen in Figs. 6. 4 (m)–(p). Similar to the results found in EBSD-IQ and EBSD-KAM maps, sample HLL (0.8%Al-0.06%V-CT580°C) CR has the highest stored energy (about  $2.73 \text{ J cm}^{-3}$ ), compared with the other three steel conditions shown in Fig. 6.4.

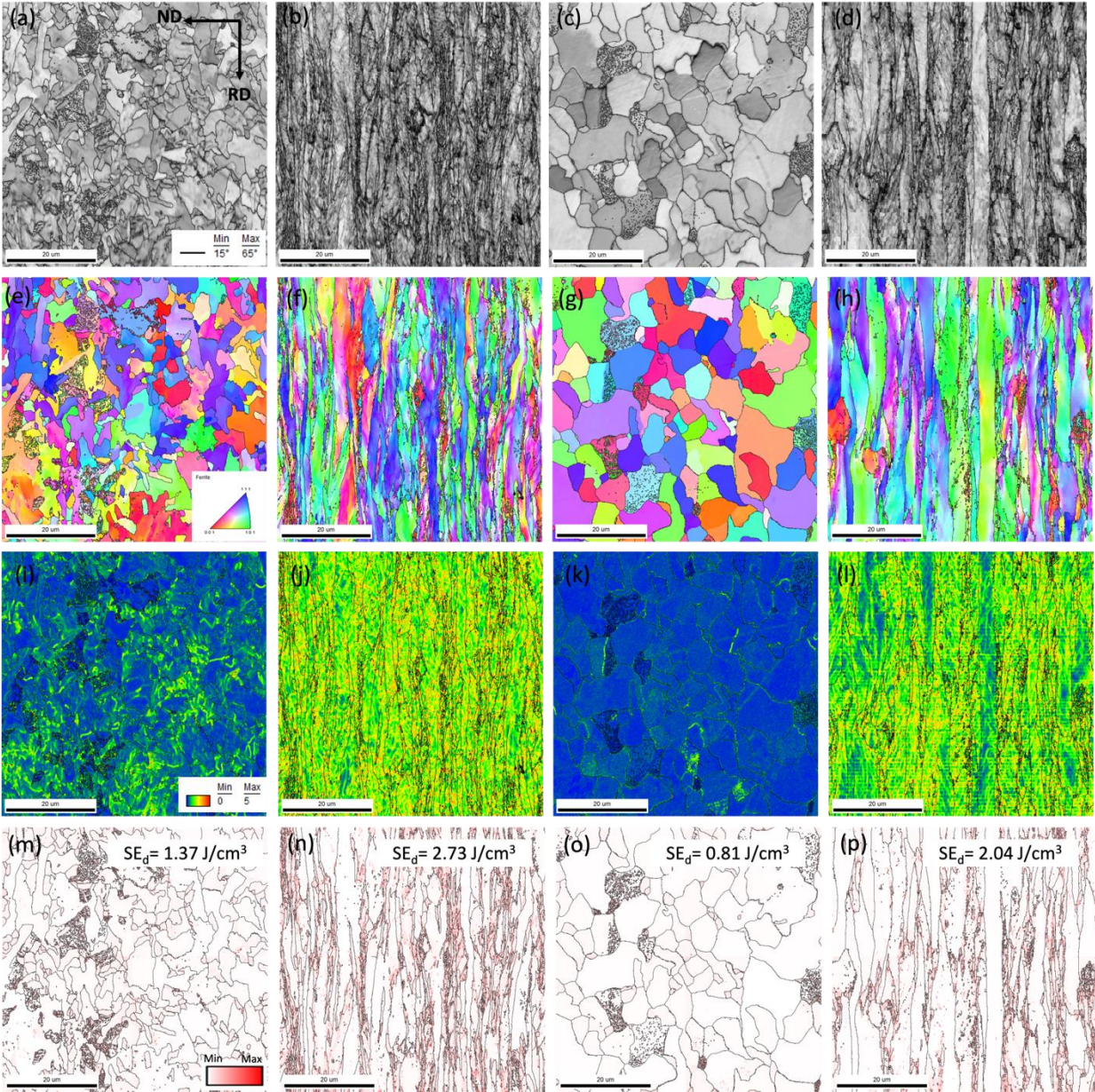


**Figure 6.4 EBSD mappings: HLL (0.8%Al-0.06%V-CT580°C) HB (a) IQ, (e) IPF, (i)KAM and (m)  $SE_d$  sub-grain; HLL CR (b) IQ, (f) IPF, (j)KAM and (n)  $SE_d$  sub-grain; HLH (0.8%Al-0.06%V-CT677°C) HB (c) IQ, (g) IPF, (k) KAM and (o)  $SE_d$  sub-grain; and HLH CR (d) IQ, (h) IPF, (l) KAM and (p)  $SE_d$  sub-grain.**

### 6.1.3 Vickers Hardness Measurements

Table 6.2 displays the microhardness (Vickers hardness 300gf) values of hot band coil and cold rolled steel sheet of each condition, which are affected by V contents, coiling temperature and cold reduction. From Table 6.2, increasing Al contents from 0.06 wt.% to 0.12 wt.% results in the increase in hardness for both hot band coils and cold rolled steel sheets. For example, the Vickers hardness values of LHL (0.04%Al-0.12%V-CT580°C) HB and LHL CR are increased from 216.2 HV to 232.6 HV and from 308.0 HV to 341.1 HV, respectively, compared with the those of LLL (0.04%Al-0.06%V-CT580°C) HB and LLL CR, since more VC precipitates formed during the transformation from finish rolling to coiling. Additionally, the results in Table 6.2 reveal that the reduction in coiling temperature from 677°C to 580°C leads to the higher Vickers hardness values for both hot rolled and cold rolled specimens. Taking the steel conditions of HLL (0.8%Al-0.06%V-CT580°C) and HLH (0.8%Al-0.06%V-CT677°C) as an example, the Vickers hardness of the hot band coil and cold rolled steel sheet for HLL are reduced by 32.8% and 6.7%, respectively, as coiling temperatures increases from 580°C to 677°C. Polygonal ferrite with low dislocation densities or sub-grain structures were found in the microstructures of candidate DP with a high coiling temperature of 677°C, while the DP steels coiled at 580°C were characterized by a large amount of acicular ferrite with high dislocation densities or sub-grain structures [159]. The combination of the differences in the dislocation densities and precipitation hardening increments led to the differences in average macro-hardness values. In addition, lattice defects, mainly dislocation were introduced by 60% cold work in this dissertation. As a result, the Vickers hardness of the cold rolled steel sheets of all steel conditions are increased by 27% - 56%, as seen in Table 6.2. Otherwise, little if any significant hardness differences were found between both hot band coils and cold rolled steel sheets containing different Al levels.

**Table 6.2 The Vickers hardness (VHN 300) values for the hot band coils (HB) and cold rolled steel sheets (CR)**

IDs	VHN (HB) (HV)	VHN (CR) (HV)	IDs	VHN (HB) (HV)	VHN (CR) (HV)
LLL	216.2 ± 5.6	308.0 ± 3.9	LLH	181.9 ± 10.7	273.3 ± 8.7
LHL	232.6 ± 14.4	341.1 ± 8.1	LHH	193.3 ± 6.9	281.6 ± 8.3
MLL	215.8 ± 9.6	302.1 ± 8.0	MLH	178.8 ± 7.4	266.1 ± 5.1
MHL	243.1 ± 7.3	333.6 ± 4.0	MHH	196.2 ± 6.4	291.4 ± 5.4
HLL	225.5 ± 6.7	286.9 ± 10.9	HLH	171.4 ± 5.3	267.7 ± 4.8

#### 6.1.4 The Assessment of Stored Energy with Three Methods Based on EBSD Technology

Sub-grain, IQ and KAM approaches based on EBSD technology were utilized to estimate the stored energy of hot rolled and cold rolled steels with different pre-annealing conditions.

##### 6.1.4.1 Sub-Grain Method

Table 6.3 shows the stored energy of the hot band coils and cold rolled steel sheets of each steel condition, estimated by applying the sub-grain method with the sub-grain misorientation limit of 6°. Applying this method to the steel conditions studied, there are two sources of GND dislocations expected to form sub-grain boundaries: one from the transformation austenite to martensite, and a second from the cold reduction. The internal strain energy is stored in these dislocation structures [100]. This is believed to be followed by dynamic recovery where the dislocations are rearranged into cells by climb of edge and cross slip of screw dislocations.

The results in Table 6.3 show that increasing coiling temperature results in a decrease in the stored energy of both hot rolled and cold rolled steels, since acicular ferrite transformed at a

low coiling temperature of 580°C, containing high dislocation densities or sub-grain structures, while the polygonal ferrite with low dislocation densities or sub-grain structures were observed in the microstructure of hot rolled DP steels with a high coiling temperature of 677°C [159]. This is despite the presence of strengthening precipitates formed at the higher coiling temperatures, as found repeatedly in earlier investigations [28]. The higher stored energy associated with the higher dislocation density found at 580°C apparently overwhelms the higher stored energy associated with the strengthening precipitates found at 677°C.

Additionally, cold work is another factor causing the difference in the stored energy. It is apparent, from Table 6.3, that the stored energy of cold rolled steels was increased by 99%–233%, compared with the counterparts of hot band coils, since 60% cold work was consumed by forming dislocation structures [99].

**Table 6.3 SE<sub>d</sub> for hot band coils (HB) and cold rolled steels (CR) based on sub-grain method**

IDs	SE <sub>d</sub> (HB) (J cm <sup>-3</sup> )	SE <sub>d</sub> (CR) (J cm <sup>-3</sup> )	IDs	SE <sub>d</sub> (HB) (J cm <sup>-3</sup> )	SE <sub>d</sub> (CR) (J cm <sup>-3</sup> )
LLL	1.44	3.06	LLH	0.93	2.17
LHL	1.16	2.70	LHH	0.84	2.37
MLL	1.27	3.21	MLH	0.69	2.30
MHL	1.19	3.01	MHH	0.94	2.15
HLL	1.37	2.73	HLH	0.81	2.04

#### 6.1.4.2 IQ Method

Previous researchers pointed out that each IQ value calculated from the Hough Transform was associated with the degree of lattice imperfection [143]. The distortion of lattices caused by the introduction of defects, such as dislocations, affects electron backscattered Kikuchi diffraction patterns, resulting in lower IQ values [141] and causing stronger strain contrasts in EBSD-IQ maps. For example, the HLL HB is characterized by a large amount of acicular ferrite with high dislocation densities or sub-grain boundaries, seen in Fig. 6.4 (a), while the microstructures of HLH predominately consist of polygonal ferrite with low dislocation densities or sub-grain boundaries, as seen in Fig. 6.4 (c). The difference in dislocation densities leads to the difference in IQ values.

In this dissertation, the reconstructed IQ results determined by applying Eq. 5.6, were normalized to range from 0 to 10. So, the reconstructed IQ values are positively related to dislocation densities or internal plastic strains. Fig. 6.5 presents the distributions of reconstructed IQ values of both hot rolled and cold rolled for steel conditions of HLL (0.8%Al-0.06%V-CT580°C) and HLH (0.8%Al-0.06%V-CT 677°C). Also, the mean reconstructed IQ values ( $IQ_{\text{mean}}$ ) for HLL HB, HLH HB, HLL CR and HLH CR are also shown in Fig. 5.6. The results reveal that  $IQ_{\text{mean}}(\text{CT}580^\circ\text{C}, \text{CR}) > IQ_{\text{mean}}(\text{CT}677^\circ\text{C}, \text{CR}) > IQ_{\text{mean}}(\text{CT}580^\circ\text{C}, \text{HB}) > IQ_{\text{mean}}(\text{CT}677^\circ\text{C}, \text{HB})$ . This indicates that, in terms of candidate DP steels containing 0.8 wt.% Al and 0.06 wt.% V, the combination of a low coiling temperature of 580°C and 60% cold work results in the highest stored energy, compared with other three pre-annealing conditions.

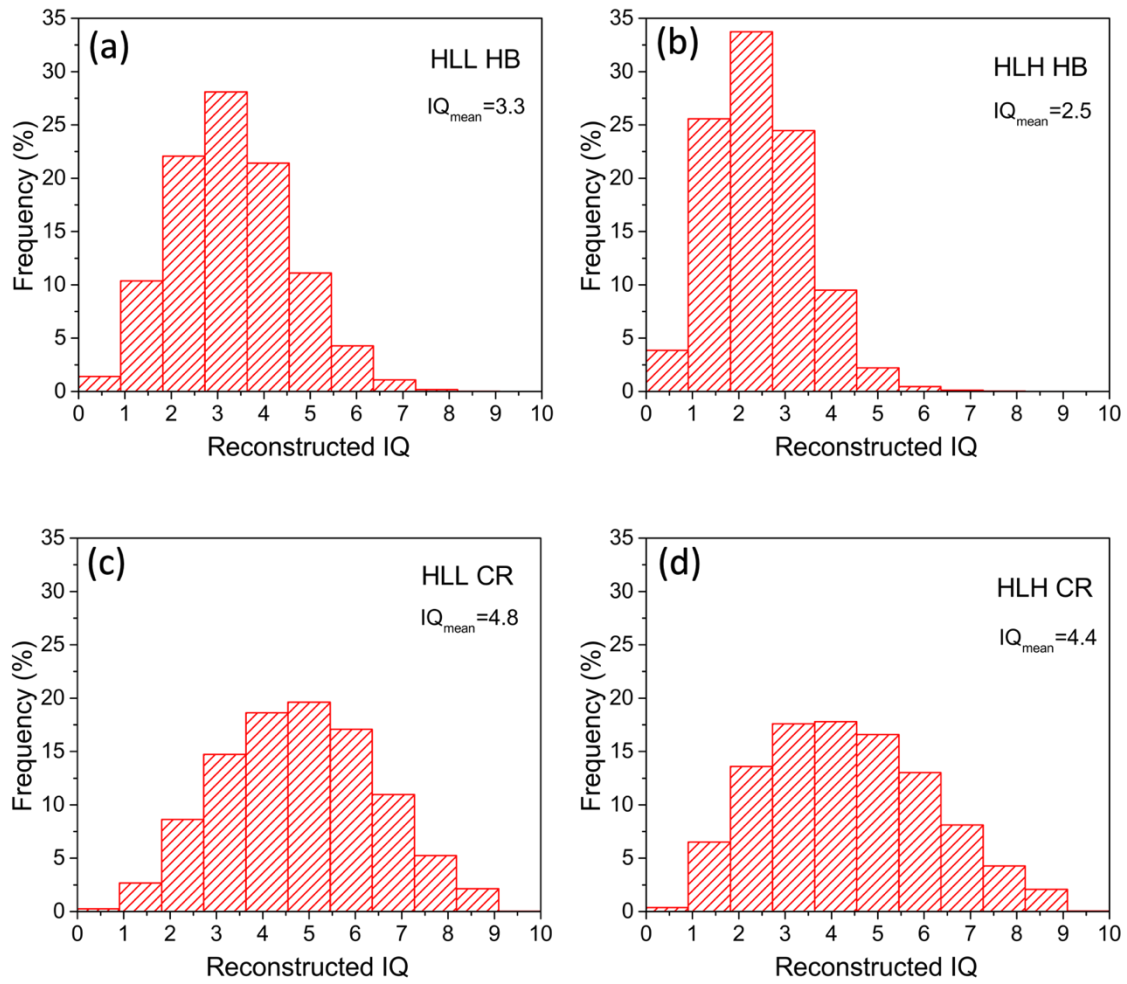


**Figure 6.5** The distributions of reconstructed IQ values for selected steel conditions with hot band coils of (a) HLL (0.8%Al-0.06%V-CT580°C) and (c) HLH (0.8%Al-0.06%V-CT 677°C) and cold rolled steel sheets of (b) HLL and (d) HLH.

### 6.1.4.3 KAM Method

The values of KAM,  $\rho_{\text{GND}}$  (calculated by using Eq. 5.8) and  $\text{SE}_d$  (calculated by using Eq. 5.9) of both hot rolled and cold rolled DP steels with different pre-annealing conditions are listed in Table 6.4. Also, these results show that pre-annealing conditions, especially coiling temperatures and cold rolling, affect the stored energy. From Table 6.4, the combination of a CT of 580°C and 60% cold reduction can result in the highest stored energy.

**Table 6.4 The results of KAM and calculated values of  $\rho_{\text{GND}}$  and  $\text{SE}_d$  for both hot rolled and cold rolled steels with pre-annealing conditions based on KAM method**

IDs	KAM	$\rho_{\text{GND}} \times 10^{10}$	$\text{SE}_d$	IDs	KAM	$\rho_{\text{GND}} \times 10^{10}$	$\text{SE}_d$
	(°)	( $\text{cm}^{-2}$ )	( $\text{J cm}^{-3}$ )		(°)	( $\text{cm}^{-2}$ )	( $\text{J cm}^{-3}$ )
LLL HB	0.568	4.00	1.01	LLL CR	1.302	9.16	2.31
LLH HB	0.347	2.44	0.62	LLH CR	1.146	8.06	2.03
LHL HB	0.519	3.65	0.92	LHL CR	1.289	9.07	2.29
LHH HB	0.409	2.88	0.73	LHH CR	1.223	8.60	2.17
MLL HB	0.617	4.34	1.09	MLL CR	1.288	9.06	2.28
MLH HB	0.380	2.67	0.67	MLH CR	1.220	8.58	2.16
MHL HB	0.634	4.46	1.12	MHL CR	1.315	9.25	2.33
MHH HB	0.395	2.78	0.7	MHH CR	1.203	8.46	2.13
HLL HB	0.585	4.11	1.04	HLL CR	1.202	8.45	2.13
HLH HB	0.384	2.70	0.68	HLH CR	1.110	7.81	1.97

#### 6.1.4.4 HAGB Energy

The total stored energy of both hot rolled and cold rolled DP steels, as given in Eq. 5.13, comprises the contribution from both sub-grain boundaries within ferrite grains and ferrite HAGBs.

Table 6.5 lists the HAGB energy ( $SE_{HAGB}$ ) calculated by Eq. 5.10. The ferrite  $SE_{HAGB}$  values for both hot band coils and cold rolled steel sheets of each pre-annealing condition only account for 11.4% - 24.6% of  $SE_d$  results, as seen in Table 6.3, evaluated by sub-grain method. This indicates that the dislocation structures (i.e., shear bands, cells or cell walls) are the predominate stored energy source, governing the kinetics of ferrite recrystallization and austenite. Otherwise, the energy contributed from HAGBs is still critical and the  $SE_{HAGB}$  of the steel conditions containing a low coiling temperature and cold reduction holds a higher value.

**Table 6.5  $SE_{HAGB}$  for hot band coils (HB) and cold rolled steels (CR)**

IDs	$SE_{HAGB}$ (HB)	$SE_{HAGB}$ (CR)	IDs	$SE_{HAGB}$ (HB)	$SE_{HAGB}$ (CR)
	(J cm <sup>-3</sup> )	(J cm <sup>-3</sup> )		(J cm <sup>-3</sup> )	(J cm <sup>-3</sup> )
LLL	0.21	0.50	LLH	0.16	0.33
LHL	0.25	0.47	LHH	0.18	0.27
MLL	0.26	0.51	MLH	0.17	0.33
MHL	0.22	0.43	MHH	0.19	0.25
HLL	0.22	0.46	HLH	0.18	0.30

## 6.2 Discussion

### 6.2.1 The Comparison among Three Stored Energy Assessment Approaches

Three approaches, by using EBSD technology, of stored energy estimation (sub-grain, IQ and KAM) for both hot rolled and cold rolled DP steels with several pre-annealing conditions were studied and compared in this chapter. Sub-grain and KAM methods quantitatively determine the stored energy, however, IQ method roughly reflect a trend for the stored energy of different steel conditions. Also, these three methods attempt to determine the grain-center stored energy associated with the internal strains in the ferrite matrix caused by dislocation density, not including the extra HAGB energy contributed from the changes in ferrite grain shape during 60% cold rolling.

Figs. 6.6 (a) and (b) show the comparison in stored energy determined by the application of sub-grain and KAM methods of hot rolled and cold rolled DP steels with different pre-annealing conditions. The results as shown in Fig 6.6 indicate that, concerning most steel conditions, the stored energy values evaluated by using sub-grain method ( $SE_d$  (sub-grain)), without including the extra ferrite HAGB energy ( $SE_{HAGB}$ ), are much higher, compared with those assessed by KAM method ( $SE_d$  (KAM)). Taking the steel condition of MLL (0.4Al-0.06V-CT580°C) as an example, the stored energy values of MLL HB, by using sub-grain and KAM methods are  $1.27 \text{ J cm}^{-3}$ , Table 6.3, and  $1.09 \text{ J cm}^{-3}$ , Table 6.4, respectively. Also, the stored energy of MLL CR calculated by sub-grain method is about  $0.93 \text{ J cm}^{-3}$  larger than that of MLL CR determined by KAM approach, Tables 6.3 and 6.4. In addition, if the extra ferrite HAGB energy ( $SE_{HAGB}$ ) is included, the total stored energy ( $SE_{tot}$ ), the sum of  $SE_d$  estimated by sub-grain method and  $SE_{HEAB}$ , is still higher than ( $SE_{tot}$ ), which is the combination of  $SE_d$  evaluated with KAM approach and  $SE_{HEAB}$ .

Fig. 6.7 (a) plots the relationship between the Vickers hardness (VHN, Table 6.2) and the stored energy determined by the sub-grain method ( $SE_d$  (sub-grain), Table 6.3) and KAM approach ( $SE_d$  (KAM), Table 6.4), respectively. The linear regression equations of VHN vs  $SE_d$  (sub-grain) and VHN vs  $SE_d$  (KAM) are given in Eqs. 6.1 and 6.2.

$$VHN = SE_d \text{ (sub-grain)} \times 58.1 + 144.7 \quad (6.1)$$

$$VHN = SE_d \text{ (KAM)} \times 71.1 + 142.3 \quad (6.2)$$

The coefficients of determination ( $R^2$ ) of linear relationship for VHN vs  $SE_d$  (sub-grain) is 0.87, while the  $R^2$  value for VHN vs  $SE_d$  (KAM) is 0.89, interpreting the fact that the nature of stored energy is highly associated with the Vickers hardness of the DP steels studied.

Fig. 6.7 (b) displays the correlation between the macro-hardness (VHN, Table 6.2) and the total stored energy ( $SE_{tot}$ ), comprising ferrite HAGB energy ( $SE_{HAGB}$ ) and sub-grain boundary ( $SE_d$ ) estimated by sub-grain or KAM methods. From the linear correlations obtained in Fig. 6.7 (b), VHN can be expressed as a function of  $SE_{tot}$  (sub-grain) or  $SE_{tot}$  (KAM), Eqs. 6.3 and 6.4.

$$VHN = SE_{tot} \text{ (sub-grain)} \times 51.3 + 142.6 \quad (6.3)$$

$$VHN = SE_{tot} \text{ (KAM)} \times 62.4 + 137.1 \quad (6.4)$$

where,  $SE_{tot}$  (sub-grain) and  $SE_{tot}$  (KAM) were defined by Eqs. 6.5 and 6.6, respectively.

$$SE_{tot} \text{ (sub-grain)} = SE_d \text{ (sub-grain)} + SE_{HAGB} \quad (6.5)$$

$$SE_{\text{tot}} (\text{KAM}) = SE_{\text{d}} (\text{KAM}) + SE_{\text{HAGB}} \quad (6.6)$$

As  $SE_{\text{HAGB}}$  is included, the coefficients of determination ( $R^2$ ) of linear relationship for VHN vs  $SE_{\text{tot}}$  (sub-grain) is 0.88, while the  $R^2$  value for VHN vs  $SE_{\text{d}}$  (KAM) is 0.92, which shows that  $SE_{\text{tot}}$ , including the extra extra  $SE_{\text{HAGB}}$ , better fits the data among the relationships for VHN vs  $SE_{\text{tot}}$  (sub-grain) and VHN vs  $SE_{\text{tot}}$  (KAM).

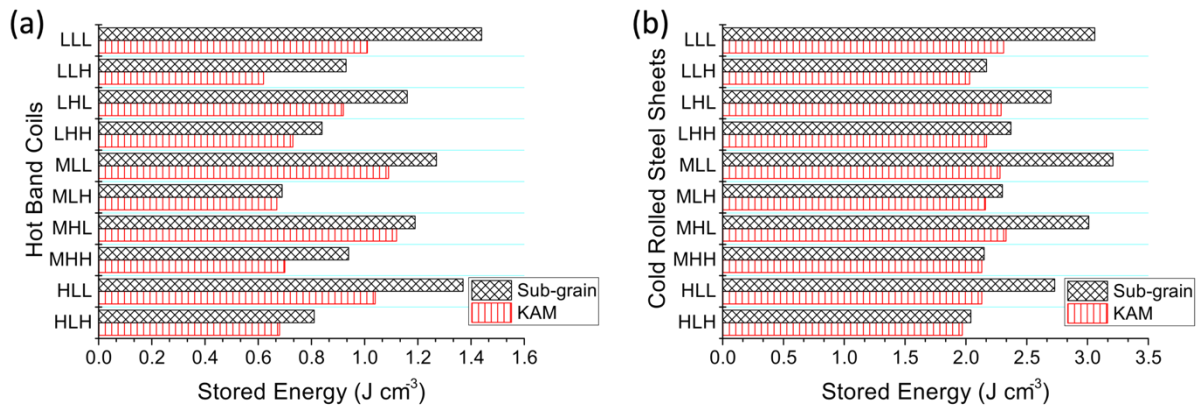


**Figure 6.6** The comparison in stored energy determined by the application of sub-grain ( $SE_{\text{d}}$  (sub-grain)) and KAM ( $SE_{\text{d}}$  (KAM)) methods of (a) hot rolled and (b) cold rolled DP steels with different pre-annealing conditions.

After plastic deformation, the cold work is often manifested by forming dislocation structures such as deformation bands, cells [99] and cell walls. Similar to grain boundaries and twin boundaries, dislocation cell boundaries (also called sub-grain boundaries) originate from geometrically necessary dislocations. But, cell boundaries follow the low energy dislocation structures (LEDS) principle [160]. So, the misorientations of cell boundaries are much smaller than those of grain boundaries and twin boundaries. In contrast, deformation bands and cell walls belong to the incidental dislocation boundaries resulting from statistically mutual random trapping,

often supplemented by “forest” dislocations [161]. In addition, most dislocations are placed in dislocation cell walls [162] and the misorientations of dislocation cell walls or shear bands are much smaller than those of cell boundaries. Calcagnotto et al.’s [112] work suggested that only the geometrically necessary dislocation densities could be calculated from KAM values, which means that energy stored in other dislocation structures such as deformation bands or cell walls cannot be obtained from the KAM method. This suggests that the KAM method is less accurate than the sub-grain boundary method. So,  $SE_d$  (sub-grain) and  $SE_d$  (KAM) are given in Eqs. 6.7 and 6.8,

$$SE_d(\text{sub-grain}) = SE_{\text{deformation bands}} + SE_{\text{cells}} + SE_{\text{cell walls}}, \text{ while} \quad (6.7)$$

$$SE_d(\text{KAM}) = SE_{\text{cells}} \quad (6.8)$$

The differences in stored energy values between these two methods is due to the difference between Eqs. 6.7 and 6.8, shown above.

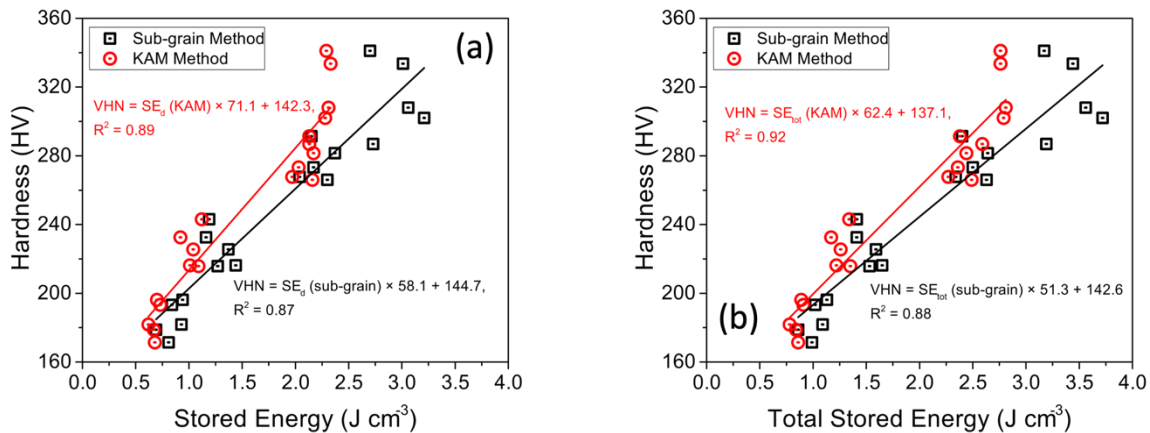


**Figure 6.7** The correlations of (a) VHN vs  $SE_d$  (sub-grain) or VHN vs  $SE_d$  (KAM) and (b) VHN vs  $SE_{tot}$  (sub-grain) or VHN vs  $SE_{tot}$  (KAM).

## 6.2.2 The Effects of Pre-Annealing Conditions on Stored Energy

In this study, the stored energy of DP steels with several initial pre-annealing conditions were investigated. Fig. 6.8 shows the effect of coiling temperatures on the total stored energy calculated by the sub-grain method for both DP hot band coils and cold rolled sheets. It is noticed that the stored energy values for steels with a low coiling temperature of 580°C are higher than those for steels coiled at 677°C. The low temperature coiled steels are characterized by the existence of a larger volume fraction of acicular ferrite with high dislocation densities or more sub-structures, while the microstructures for steels coiled at 677°C consist of polygonal ferrite with low dislocation densities [159], but high precipitation hardening increments. The difference in dislocation densities of these two types of ferrite appears to be the dominant feature leading to the difference in the total stored energy values.

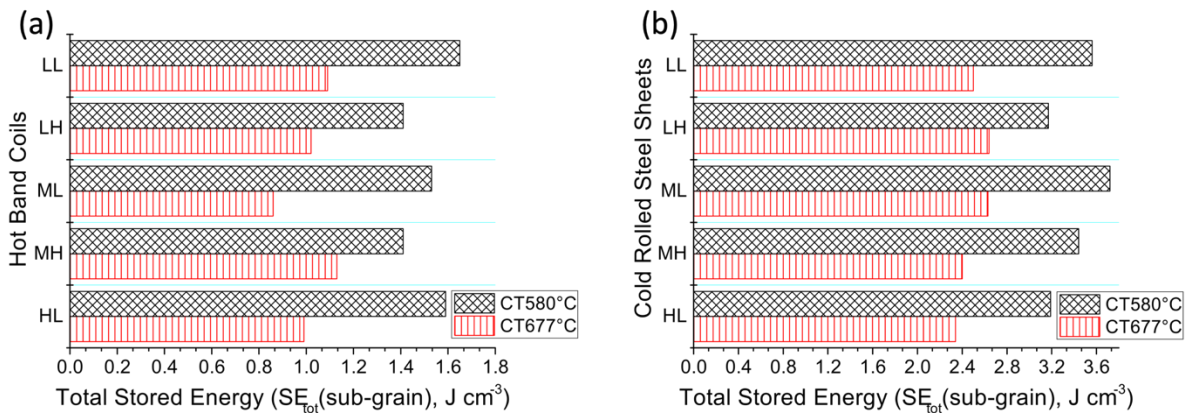


**Figure 6.8** The comparison in stored energy determined by the application of sub-grain ( $SE_d$  (sub-grain)) for hot rolled and (b) cold rolled steels with two different coiling temperatures (580°C and 677°C).

In addition to the coiling temperatures, cold reductions also have a critical influence on stored energy. Fig. 6.9 presents the total stored energy evaluation based on the sub-grain method

for DP hot band coils (without cold work) and cold rolled sheets (with 60% cold work). It should be emphasized that the total stored energy values of cold rolled sheets are higher than those of hot band coils with the same chemical compositions as well as coiling temperatures. In this case, after 60% cold rolling, cold work was consumed by forming numerous dislocation structures such as shear bands, cells [99] and cell walls and elastic strain energy was stored in the sub-grain boundaries within the ferrite matrix. It can be expected that the higher stored energy obtained from cold rolling increases the rates for ferrite recrystallization and austenite formation during the heating portion and isothermal intercritical annealing in the limited annealing time (~60 s) available in continuous galvanizing lines (CGL).

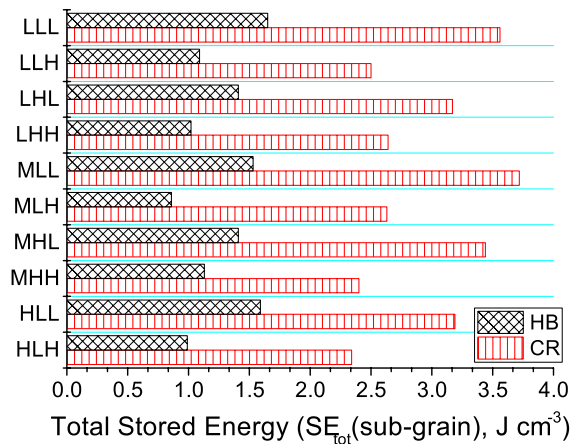


**Figure 6.9 The total stored energy evaluation based on the sub-grain method ( $SE_{tot}(\text{sub-grain})$ ) for steels with and without 60% cold reduction.**

### 6.3 Conclusions

The main purposes of this chapter were to compare three stored energy evaluation methods (sub-grain, IQ and KAM) for DP steels with different initial conditions, and to investigate the effects of pre-annealing conditions (i.e., with change in coiling temperatures at constant cold reduction) on the stored energy. The findings can be summarized as follows.

(1) Both sub-grain and KAM approaches can predict the specific stored energy values for DP steels. Compared with the sub-grain method, the KAM method highly underestimates the stored energy, since only the energy stored in dislocation cells is considered in this approach. Regarding the sub-grain method, all the dislocation structures (i.e., shear bands, cells and cells walls) are taken into consideration. Although IQ method cannot quantitatively predict the stored energy values, this method does help to show the trends of stored energy for steels with initial pre-annealing conditions.

(2) The minority of stored energy comes from HAGB energy, which accounts for about 11.4% - 24.6% of the energy stored in dislocation structures, but it is still critical to reflect the hardness.

(3) The stored energy varies with both coiling temperatures and cold reductions. At a low coiling temperature, acicular ferrite nucleates and grows with high dislocation densities, while polygonal ferrite with low dislocation densities exists in the microstructures of steels coiled at a high coiling temperature. The difference in dislocation density results in the difference in stored energy. In terms of cold reduction, the cold work is consumed by forming dislocation structures (shear bands, cells and cell walls), so the stored energy values of cold rolled sheets are always higher than those of hot band coils.

(4) The DP steels with the combination of low coiling temperature and low cold reduction have the highest stored energy, providing more initial driving force for ferrite recovery and recrystallization as well as austenite nucleation and growth during the subsequent intercritical annealing.

## 7.0 Austenite Formation Studies with Al Contents

### 7.1 Results

#### 7.1.1 Fe-Fe<sub>3</sub>C Phase Diagram

The Fe- Fe<sub>3</sub>C phase diagrams and critical temperatures ( $A_1$ ,  $A_3$  and  $A_{cm}$ ) for DP steels with different Al and V contents were estimated by applying JMatPro, seen in Fig. 7.1. Comparing the phase diagrams for three Al levels (0.04/0.4/0.8 wt.% Al), it is obvious that Al (as a ferrite stabilizer) increases both  $A_1$  and  $A_3$  temperatures and expands dramatically  $\alpha + \gamma$  two phase region. The corresponding values are recorded in Table 7.1. For example, in terms of the steel conditions of LL (0.04Al-0.06V), ML (0.4Al-0.06V) and HL (0.8Al-0.06V), the  $A_1$  temperature raises from 707.6°C to 714.8°C and to 724.2°C, as seen in Fig. 7.1 and Table 7.1, with increasing Al content from 0.04 to 0.4 and to 0.8 wt.%. Also, the relevant  $A_3$  temperatures of LL (0.04Al-0.06V), ML (0.4Al-0.06V) and HL (0.8Al-0.06V) are 808.6°C, 848.1°C and 911.7°C. As a result,  $A_3 - A_1$  temperature range varies with Al contents, starting from 101.0°C (LL (0.04Al-0.06V)) to 187.5°C (HL (0.8Al-0.06V)), Table 7.1. Additionally, the effect of V contents on Fe-C diagram is not evident. The V content starting from 0.06 wt.% to 0.12wt% only slightly increases  $A_1$  and  $A_3$  temperatures, Fig 7.1 and Table 7.1.

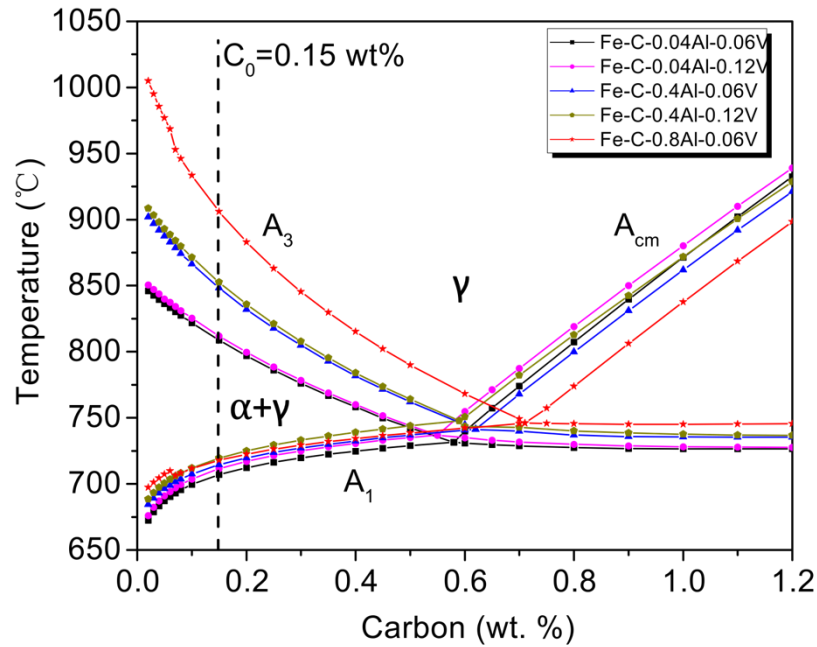


Figure 7.1 The Fe-C phase diagrams for candidate DP steels, illustrating effects of Al and V contents on Fe-C phase diagram (critical temperatures were estimated by JMatPro)

Table 7.1 Effects of Al and V on critical temperatures  $A_1$  and  $A_3$

IDs	Steel Conditions	$A_1$ (°C)	$A_3$ (°C)	$A_3 - A_1$ (°C)
LL	0.15C-0.04Al-0.06V	707.6	808.6	101.0
LH	0.15C-0.04Al-0.12V	712.1	811.8	99.7
ML	0.15C-0.4Al-0.06V	714.8	848.1	133.3
MH	0.15C-0.4Al-0.12V	719.9	852.3	132.4
HL	0.15C-0.8Al-0.06V	724.2	911.7	187.5

### 7.1.2 CCT Diagram

Fig. 7.2 presents the CCT diagrams estimated by JMatPro from full austenite region (cooling from the FRT of 920°C) for candidate DP steels with different Al and V levels. The effects of cooling rates on transformation temperatures for austenite decomposition products are shown in Fig. 7.2, with ferrite, pearlite, bainite and martensite start temperatures and martensite finish temperature labeled by  $F_s$ ,  $P_s$ ,  $B_s$ ,  $M_s$  and  $M_f$ , respectively. Table 7.2 lists the transformation cooling rate of  $15^\circ\text{C s}^{-1}$ , since  $15^\circ\text{C s}^{-1}$  is the cooling rate applied in the two Gleeble CGL simulations used in this research.

The comparison of CCT diagrams for the candidate DP steels with different Al contents illustrates that the  $F_s$  temperature increases with increasing Al contents starting from 0.04 wt.% to 0.8 wt.%, Fig. 7.2. Regarding the steel conditions of LL (0.04Al-0.06V), ML (0.4Al-0.06V) and HL (0.8Al-0.06V), the  $F_s$  temperature dramatically increases from 537.0°C (LL (0.04Al-0.06V)) to 784.4°C (HL (0.8Al-0.06V)) at a cooling rate of  $15^\circ\text{C s}^{-1}$ , Table 7.2. Also, the Al contents expand the ferrite formation zone to the higher cooling rates from  $20^\circ\text{C s}^{-1}$  (LL (0.04Al-0.06V)) to more than  $100^\circ\text{C s}^{-1}$  (HL (0.8Al-0.06V)). This means that the high Al content lowers austenite stability and new ferrite formation cannot be avoided during intercritical annealing even at a higher cooling rate, which will reduce the amount of fresh martensite and thus cause the loss of UTS. However, the influence of V on  $F_s$  is not evident. V contents only slightly lower  $F_s$  temperature, Table 7.2.

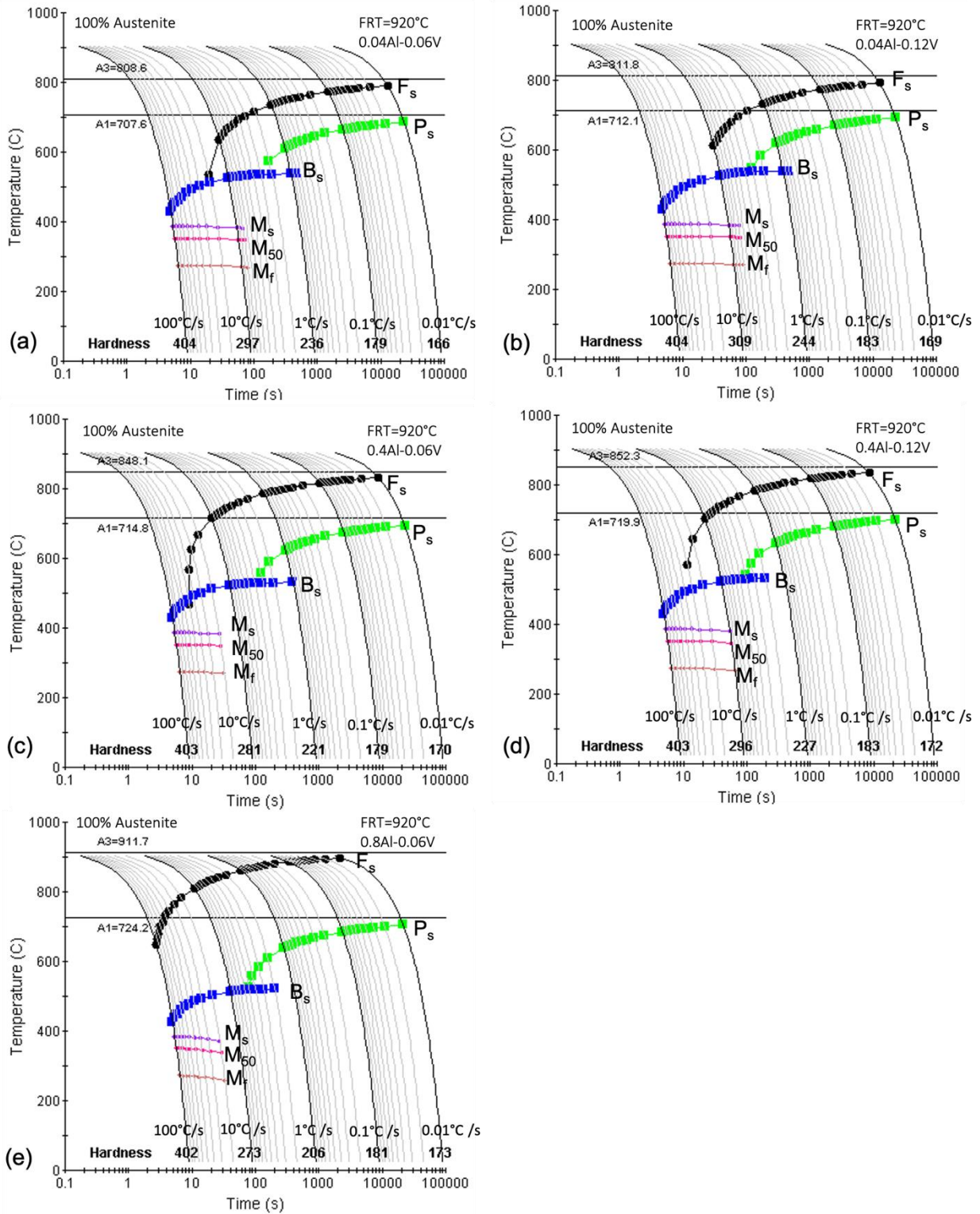


Figure 7.2 The CCT diagrams estimated by JMatPro from full austenite region for candiadte DP steels with conditions of (a) LL (0.04Al-0.06V), (b) LH (0.04Al-0.12V), (c) ML (0.4Al-0.06V), (d) MH (0.4Al-0.12V) and (e) HL (0.8Al-0.06V).

The Al content reduces austenite stability and hence advances pearlite transformation at a relatively high cooling rate, for instance,  $5^{\circ}\text{C s}^{-1}$  (for 0.8Al), Fig. 7.2. Since  $15^{\circ}\text{C s}^{-1}$  is the cooling rate applied in two Gleeble CGL simulations, pearlite can be totally avoided in the final microstructures.

The  $B_s$  temperatures vary with Al contents from  $513.3^{\circ}\text{C}$  (for 0.04 wt.% Al) to  $503.8^{\circ}\text{C}$  (for 0.8 wt.% Al), in terms of the cooling rate of  $15^{\circ}\text{C s}^{-1}$ , as seen in Table 7.2. The existence of bainite makes martensite not the predominate phase as the cooling rate exceeds  $15^{\circ}\text{C s}^{-1}$  within the CCT diagram. As a result, martensite is not the only second phase in the final microstructures of the fully annealed DP steels, even at a cooling rate of  $100^{\circ}\text{C s}^{-1}$ . This will hinder the ability of these steels to reach high UTS levels.

In terms of martensite transformation, The  $M_s$  and  $M_f$  temperatures decrease as the cooling rate falls. Additionally, Al contents slightly lower both  $M_s$  and  $M_f$  temperatures. This is ascribed to the formation of a large amount of new ferrite and carbon enrichment in the remaining austenite.

**Table 7.2 Effects of Al and V on transformation temperatures of austenite decomposition products from full austenite temperature (FRT =  $920^{\circ}\text{C}$ ) at a cooling rate of  $15^{\circ}\text{C s}^{-1}$**

IDs	Steel Conditions	$F_s$ ( $^{\circ}\text{C}$ )	$B_s$ ( $^{\circ}\text{C}$ )	$M_s$ ( $^{\circ}\text{C}$ )	$M_f$ ( $^{\circ}\text{C}$ )
LL	0.15C-0.04Al-0.06V	537.0	513.3	385.4	273.2
LH	0.15C-0.04Al-0.12V	526.1	513.3	385.8	273.6
ML	0.15C-0.4Al-0.06V	669.1	511.6	382.7	270.3
MH	0.15C-0.4Al-0.12V	643.8	512.7	384.3	272.0
HL	0.15C-0.8Al-0.06V	784.4	503.8	371.9	258.5

### 7.1.3 Microstructural Observation of Austenite Formation for Candidate DP Steels with Al

#### Contents

Prior to intercritical annealing, the initial microstructures of the selected cold rolled DP steel conditions LLL (0.04Al-0.06V-CT580°C), MLL (0.4Al-0.06V-CT580°C) and HLL (0.8Al-0.06V-CT580°C) are elongated ferrite-pearlite aggregates, shown in Fig. 6.3, consisting of about 60% – 70% ferrite, Table 6.1.

Phase transformations occurring during intercritical annealing for a DP steel with a starting microstructure of cold rolled ferrite-pearlite aggregates consist of ferrite recrystallization and austenite formation. Ferrite recrystallization has been shown to be completed prior to austenite formation at a low reheating rate (i.e.,  $+1 \sim +5^\circ\text{C s}^{-1}$  [53,66,74]), and ferrite recrystallization coexists with austenite formation at a high reheating rate (i.e.,  $> +50^\circ\text{C s}^{-1}$  [53,66,74]). The reheating rate used in this research was  $+5^\circ\text{C s}^{-1}$ , combined with the effect of stored energy obtained from low temperature ferrite transformation during coiling (CT580°C) and cold work (60% cold reduction), so ferrite recrystallization was considered to fully complete during reheating to desired IATs.

During the intercritical annealing of the DP steels with the initial microstructures of ferrite plus pearlite mixtures, the first step of austenite formation is pearlite dissolution (i.e., dissolution of pearlitic cementite) [9,51,52,163]. Pearlite dissolution is considered to complete within 15s at a high intercritical annealing temperature [9]. For example, Fig. 7.3 shows the microstructural evolution of a steel condition MLL (0.4Al-0.06V-CT580°C) annealed at 770°C from 0s to 60s. In this case, the completion of pearlite dissolution only took 5s. In the wake of 5-second holding at 770°C, all the pearlite was fully dissolved, with only with a few cementite particles remaining undissolved in the ferrite matrix, Fig. 7.3 (b).

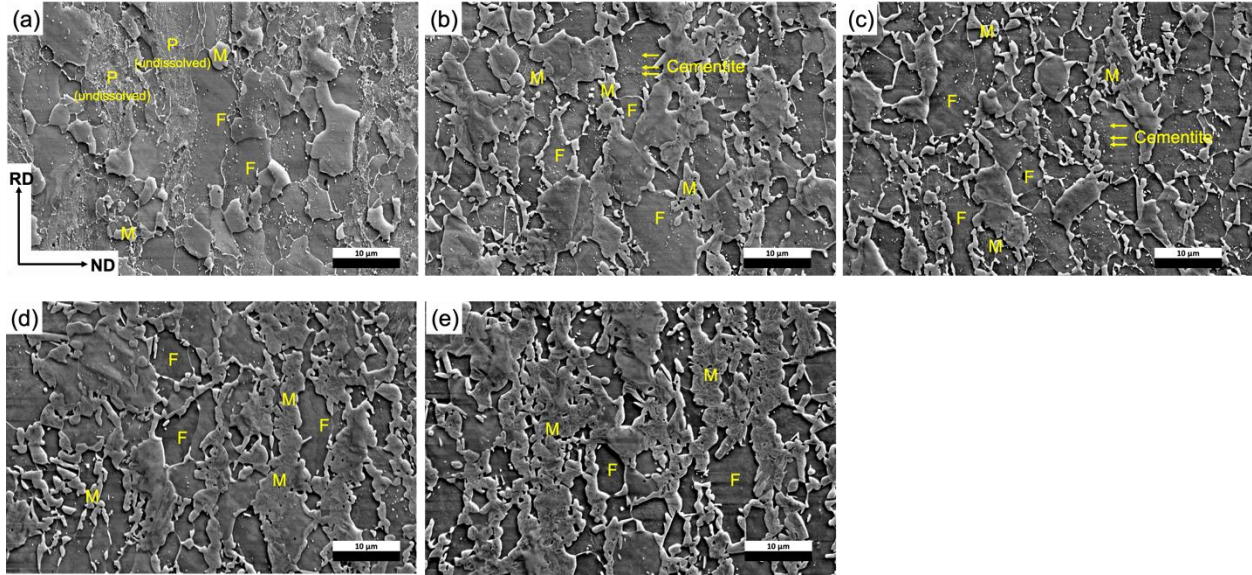


**Figure 7.3 SEM micrographs of steel condition MLL (0.4Al-0.06V-CT580°C) annealed at 770°C for (a) 0s, (b) 5s, (c) 15s, (d) 30s and (e) 60s. Note: ferrite is indicated by F, pearlite by P and martensite by M. Water-quenched martensite represents intercritically formed austenite.**

However, the process of pearlite dissolution becomes more time-consuming as IAT falls to 740°C. An example of partial cementite dissolution of steel condition MLL (0.4Al-0.06V-CT580°C) annealed at 740°C for 60s is shown in Fig. 7.4.

Additionally, the early stage of austenite formation is austenite nucleation, shown in Fig. 7.5. Fig. 7.5 presents the SEM micrographs of steel condition LLL (0.04Al-0.06V-CT580°C) reheated to 740°C without isothermal holding and water quenched to room temperature. Those tiny water-quenched martensite islands represent austenite nuclei at 740°C. Fig. 7.5 (a) shows the austenite nuclei located at cementite/ pearlitic ferrite interfaces within pearlite colonies. Also, austenite nuclei were observed at the interfaces between ferrite and prior pearlite colonies, Fig. 7.5 (b). As shown in Fig. 7.5 (c), austenite nucleated at the recrystallized ferrite/ ferrite grain boundaries or triple points associated with undissolved cementite, which is in agreement with

Garcia and DeArdo's previous observation [51]. Finally, several austenite particles were found within ferrite grains, Fig. 7.5 (d). The nucleation of austenite located at the ferrite/ferrite grain boundaries or within ferrite grains is possibly due to the carbon diffusion through a long distance from carbon-rich prior pearlite colonies to the carbon-limited recrystallized ferrite areas [164].

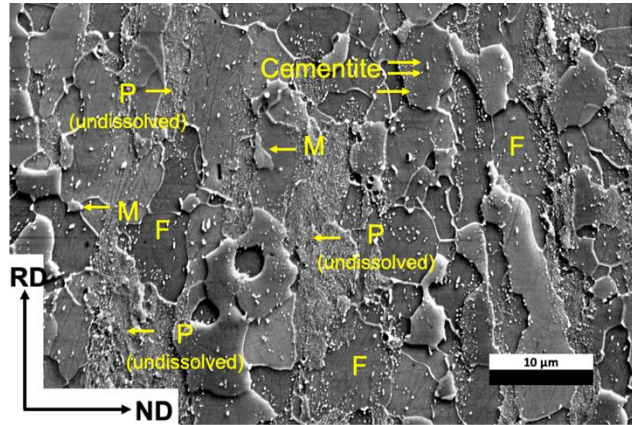


**Figure 7.4 SEM micrograph of steel condition MLL (0.4Al-0.06V-CT580°C) annealed at 740°C for 60s. Note: ferrite is indicated by F, pearlite by P and martensite by M. Water-quenched martensite represents intercritically formed austenite.**

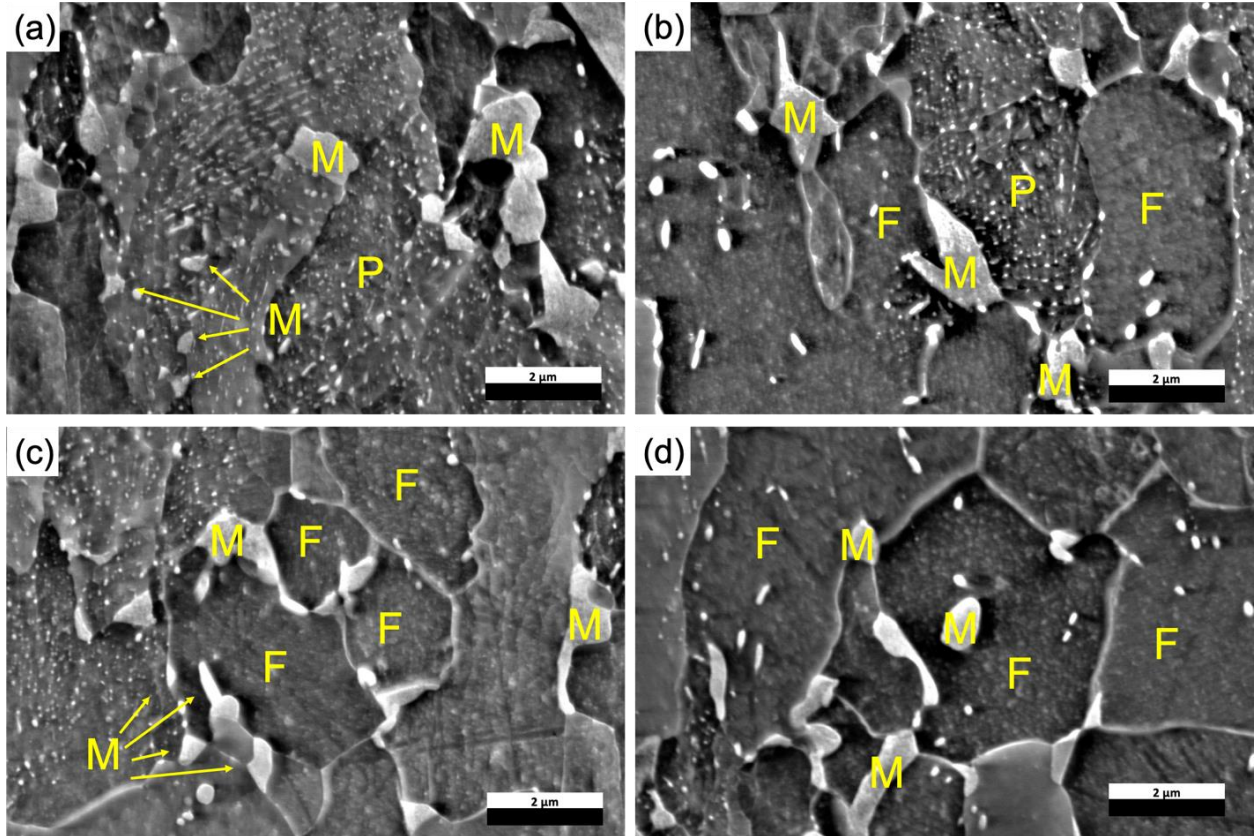


**Figure 7.5 SEM micrographs of steel condition LLL (0.04Al-0.06V-CT580°C) annealed at 740°C for 0s, illustrating austenite nucleation sites: (a) interfaces between cementite/pearlitic ferrite within pearlite colonies, (b) interface between ferrite/pearlite, (c) recrystallized ferrite/ferrite grain boundaries or triple points and (d) within ferrite grains. Note: ferrite is indicated by F, pearlite by P and martensite by M. Water-quenched martensite represents intercritically formed austenite.**

As the isothermal holding time increases, further austenite growth continues, shown in Figure 7.6, presenting the SEM micrograph of steel condition LLL (0.04Al-0.06V-CT580°C) annealed at 740°C for 5s. Austenite grew from the prior pearlite colonies (the area highlighted by the spot curve in Fig. 7.6), consuming dissolving pearlite, and from the grain boundary allotriomorphic austenite, which were also reported in other studies [9,51,53,74,163]. Also, the slow heating rate (i.e., +5 °C in this study) advances the growth of austenite nucleated in the prior

pearlite colonies [74], so the distribution and morphology of austenite are similar to those of prior pearlite colonies which were geometrically modified by cold rolling.

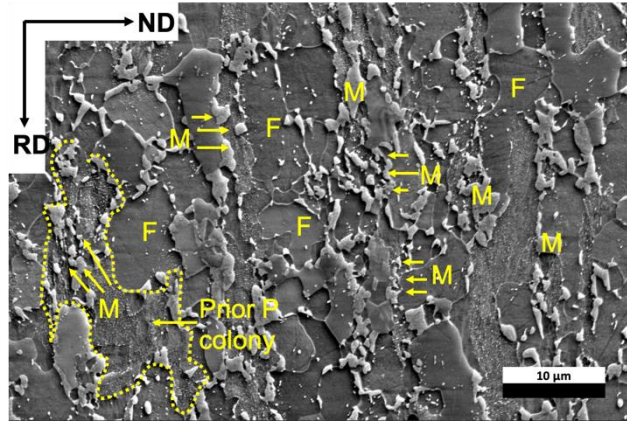


**Figure 7.6 SEM micrograph of steel condition LLL (0.04Al-0.06V-CT580°C) annealed at 740°C for 5s. Note: ferrite is indicated by F, pearlite by P and martensite by M. Water-quenched martensite represents intercritically formed austenite.**

Since all the intercritically formed austenite is assumed to transform to martensite by water quenching, martensite volume percentage ( $f_m$ ) is assumed to equal to the volume fraction of intercritically formed austenite ( $f_\gamma$ ). The results of quantitative measurements for  $f_\gamma$  of selected DP steels with Al contents in different annealing conditions are plotted in Fig. 7.7. The differences in austenite percentages among annealing time, annealing temperatures and Al contents can be observed in Fig. 7.7. It is obvious that  $f_\gamma$  can be a function of annealing temperature and  $f_\gamma$  increases as annealing time increases. Fig. 7.8 shows the SEM micrographs of steel condition LLL (0.04Al-0.06V-CT580°C) annealed at 740°C, 770°C and 800°C for 3600s. The increase in annealing temperatures advances  $f_\gamma$ . Fig. 7.9 presents the SEM micrographs of steel conditions LLL (0.04Al-0.06V-CT580°C), MLL (0.4Al-0.06V-CT580°C) and HLL (0.8Al-0.06V-CT580°C) annealed at 800°C for 3600s. Al contents reduces  $f_\gamma$  at the same annealing temperature and annealing time.

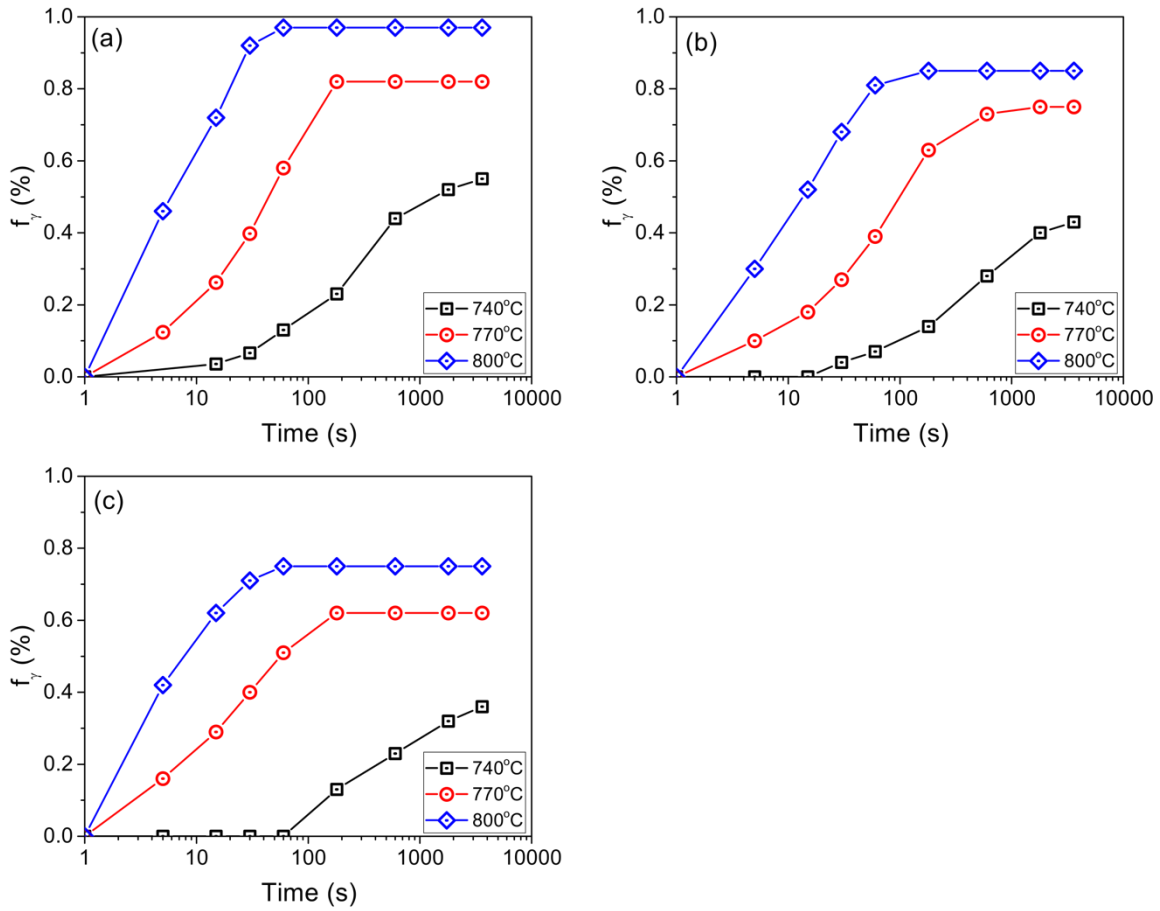


**Figure 7.7** The plots of volume fraction of intercritically formed austenite as a function of annealing time at different intercritical annealing temperatures for steel conditions of (a) LLL (0.04 wt.% Al), (b) MLL (0.04 wt.% Al), and (c) HLL (0.8 wt.% Al).

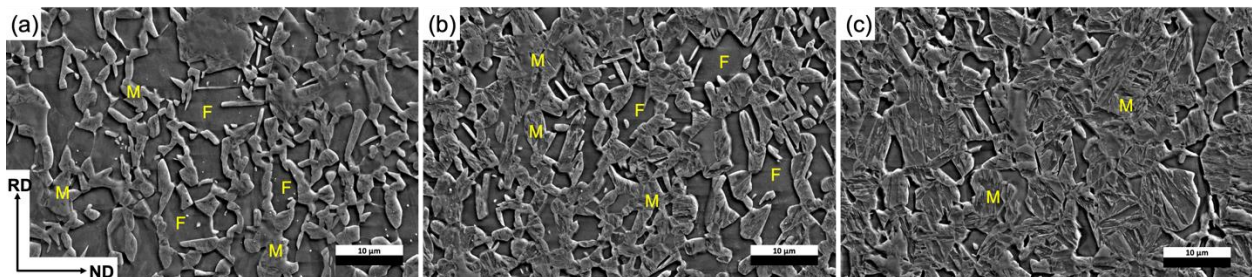


**Figure 7.8** SEM micrographs of steel condition LLL (0.04Al-0.06V-CT580°C) annealed at (a) 740°C, (b) 770°C and (c) 800°C for 3600s. Note: ferrite is indicated by F and martensite by M. Water-quenched martensite represents intercritically formed austenite.

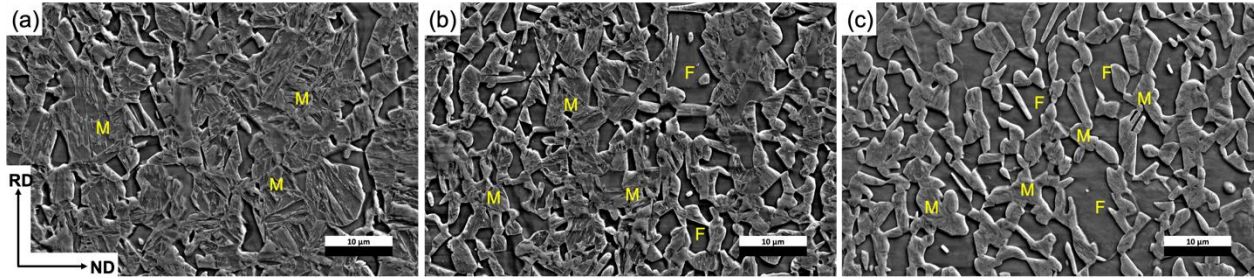


Figure 7.9 SEM micrographs of steel conditions (a) LLL (0.04Al-0.06V-CT580°C), (b) MLL (0.4Al-0.06V-CT580°C) and (c) HLL (0.8Al-0.06V-CT580°C) annealed at 800°C for 3600s. Note: ferrite is indicated by F and martensite by M. Water-quenched martensite represents intercritically formed austenite.

#### 7.1.4 Determination of the Kinetics Model of Intercritically Annealed Austenite Formation

The austenite formation from a cold rolled DP steel is a diffusion-controlled phase transformation, the reaction proceeding by nucleation and growth [165]. The fraction of austenite ( $f_\gamma$ ) can be estimated by using Johnson-Mehl-Avrami (JMA) with Kolmogorov modification (JMAK), shown in Eq. 7.1 [49,165–169],

$$f_\gamma = 1 - \exp(-kt^n) \quad (7.1)$$

where,  $t$  is the annealing time,  $n$  the Avrami exponent and  $k$  the rate constant. However, one problem of Eq. 7.1 is that the infinity value of  $f_\gamma$  at some IATs can never approach one. Since by reheating a cold rolled DP steel to an IAT, the austenite volume percentage, according to the lever rule, in the final microstructure after full annealing cannot reach one. So, a modified JMAK model was established for the kinetics of intercritically annealed austenite formation, which can be presented by Eq. 7.2 [169],

$$\frac{f_{\gamma}}{f_{\gamma(\text{eq})}} = 1 - \exp(-kt^n) \quad (7.2)$$

where,  $f_{\gamma(\text{eq})}$  is the equilibrium fraction of austenite at a certain IAT. In this case,  $f_{\gamma}/f_{\gamma(\text{eq})}$  is the degree of austenitization, ranging from zero to one. Taking the logarithm on both sides of Eq. 7.2, Eq. 7.3 is shown as follows,

$$\ln \left[ \ln \left( \frac{f_{\gamma(\text{eq})}}{f_{\gamma(\text{eq})} - f_{\gamma}} \right) \right] = n \ln t + \ln k \quad (7.3)$$

From Eq. 7.3, the linear relations of  $\ln(\ln(f_{\gamma(\text{eq})}/(f_{\gamma(\text{eq})}-f_{\gamma})))$  vs  $\ln t$  can be plotted, indicating the Avrami exponent ( $n$ ), the slope of the straight lines and  $\ln k$ , the intercept with  $\ln(\ln(f_{\gamma(\text{eq})}/(f_{\gamma(\text{eq})}-f_{\gamma})))$  axis.

Additionally, the rate constant ( $k$ ) is dependent on annealing temperature, nucleation rate and growth rate [170], which can be expressed by Eq. 7.4 [166],

$$k = k_0 \exp \left( \frac{-Q}{RT} \right) \quad (7.4)$$

where,  $k_0$  is the pre-exponential factor,  $Q$  the apparent activation energy,  $R$  the ideal gas constant ( $R = 8.3145 \text{ J mol}^{-1} \text{ K}^{-1}$ ) and  $T$  the absolute temperature in Kelvin. Also, taking the logarithm on both sides of Eq. 7.4, the following Eq. 7.5 can be reached,

$$\ln k = -\frac{Q}{RT} + \ln k_0 \quad (7.5)$$

From Eq. 7.5, the apparent activation energy ( $Q$ ) and frequency factor ( $k_o$ ) can be predicted from the linear plots of  $\ln k$  vs  $1/T$ . From Fig. 7.9, the equilibrium fraction of austenite ( $f_{\gamma (eq)}$ ) of candidate DP steels with different Al contents are shown in Table 7.3. After data analysis by using Eqs. 7.3 and 7.5, the Avrami exponent ( $n$ ), pre-exponential factor ( $k_o$ ) and apparent activation energy ( $Q$ ) of steel conditions of LLL (0.04 wt.%), MLL (0.4 wt.%), and HLL (0.8 wt.%) are listed in Table 7.4.

**Table 7.3 Equilibrium fraction of austenite ( $f_{\gamma (eq)}$ ) of candidate DP steels with different Al contents**

IDs	Steel Conditions	Equilibrium Fraction of Austenite		
		Intercritical Annealing Temperature ( $^{\circ}\text{C}$ )		
		740	770	800
LLL	0.04Al-0.06V-CT580 $^{\circ}\text{C}$	0.55	0.82	0.97
MLL	0.4Al-0.06V-CT580 $^{\circ}\text{C}$	0.43	0.75	0.85
HLL	0.8Al-0.06V-CT580 $^{\circ}\text{C}$	0.36	0.62	0.75

**Table 7.4 Avrami exponent ( $n$ ), pre-exponential factor ( $k_o, \text{s}^{-1}$ ) and activation energy ( $Q, \text{kJ mol}^{-1}$ ) of candidate DP steels with different Al contents**

IDs	Steel Conditions	$n$	$k_o (\text{s}^{-1})$	$Q (\text{kJ mol}^{-1})$
LLL	0.04Al-0.06V-CT580 $^{\circ}\text{C}$	0.81	4.7E+19	422.9
MLL	0.4Al-0.06V-CT580 $^{\circ}\text{C}$	0.76	2.8E+20	436.5
HLL	0.8Al-0.06V-CT580 $^{\circ}\text{C}$	0.72	4.5E+23	496.7

Applying  $f_{\gamma(eq)}$ ,  $n$ ,  $k_0$  and  $Q$  values in Tables 7.3 and 7.4 to Eqs. 7.4 and 7.6, Fig 7.10 shows the predictions based on kinetics modeling of austenite volume percentages of three candidate DP steels with Al contents at different IATs and annealing times. From Fig 7.10, the modeling curves have a good fit to the experimental results.

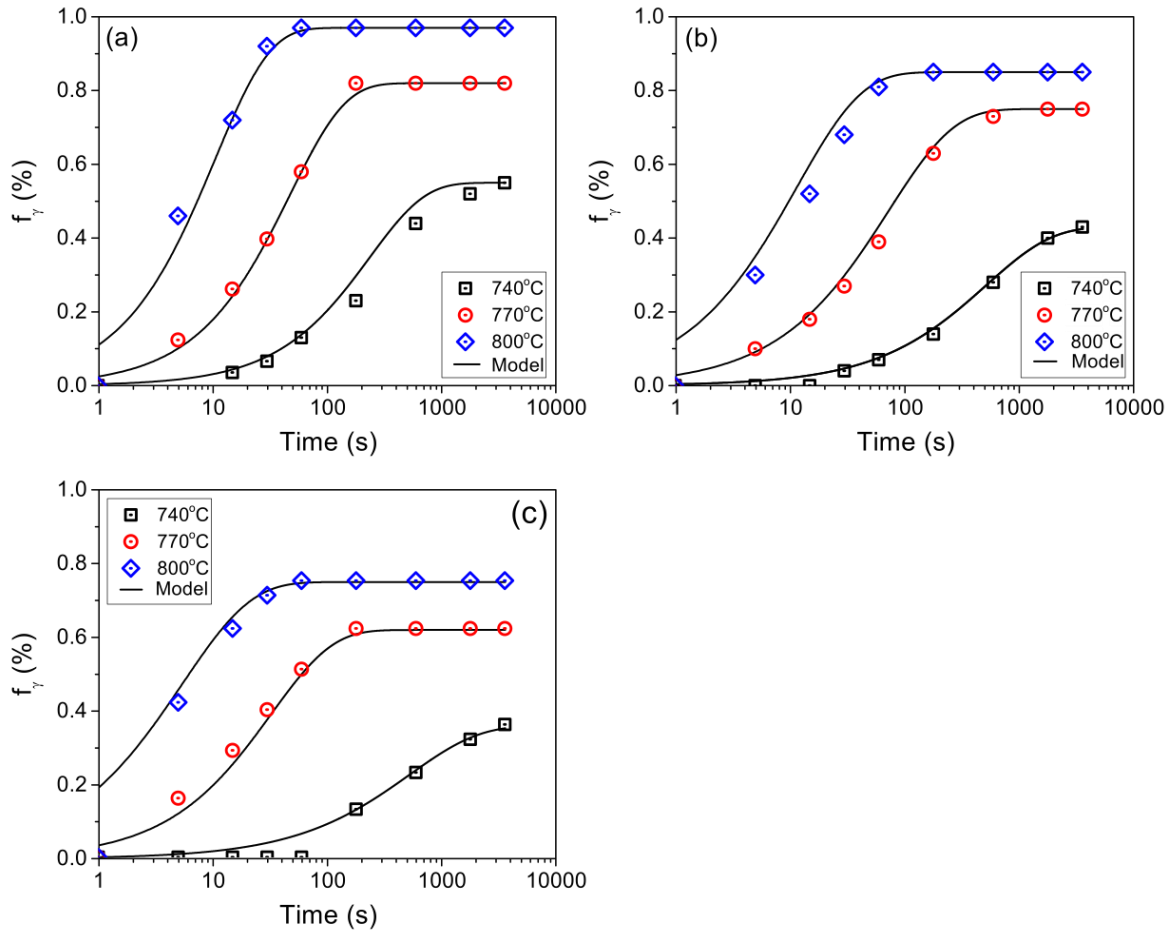


**Figure 7.10 Predictions based on kinetics modeling and experimental results of austenite volume percentages of steel conditions of (a) LLL (0.04 wt.% Al), (b) MLL (0.4 wt.% Al) and (c) HLL (0.8 wt.% Al). Data points shown as symbols while theory shown as continuous lines.**

## 7.2 Discussion

### 7.2.1 Effect of Al Contents on Austenite Formation during Intercritical Annealing

Fig. 7.11 shows schematically the microstructural evolution of the candidate DP steels from the starting condition to the annealed. The hot band coils with a low coiling temperature of 580 °C were characterized by a combination of acicular ferrite, polygonal ferrite and pearlite, Fig. 6.1 (a). After 60% cold reduction, deformed and elongated ferrite and pearlite along with a large amount of cementite located at ferrite/ferrite grain boundaries were observed in the microstructures of cold rolled steel sheets, Fig. 6.3 (a), which were regarded as the initial conditions of the intercritical annealing process.

During the process of heating, the deformed ferrite has recrystallized, prior to reaching to the optimum IATs, at a low heating rate of  $+5\text{ }^{\circ}\text{C s}^{-1}$ , which is in agreement with previous studies [53,66,74]. This means that there would be no competition between ferrite recrystallization and austenite formation during isothermal holding at IATs in the case of low heating rates.

Pearlite dissolution and austenite nucleation and growth are two essential steps of austenite formation for the DP steels with ferrite-pearlite mixture initial microstructures [9,51,52,163,171]. The time for the completion of pearlite dissolution is temperature dependent. Speich et al. [9] reported that pearlite could be fully dissolved in 15s at a high IAT, while a longer time for pearlite dissolution would be needed at a low IAT. Austenite nucleated at the pearlitic ferrite/ cementite interfaces in the prior pearlite colonies (Fig. 7.5 (a)), at the prior pearlite colony boundaries (Fig. 7.5 (b)), at the recrystallized ferrite/ ferrite grain boundaries or triple points (Fig. 7.5 (c)) and within ferrite grains (Fig. 7.5 (d)). These austenite nuclei were also observed by Garcia and DeArdo [51], Speich [9], Yang [52], Yi [163] and Caballero [172].

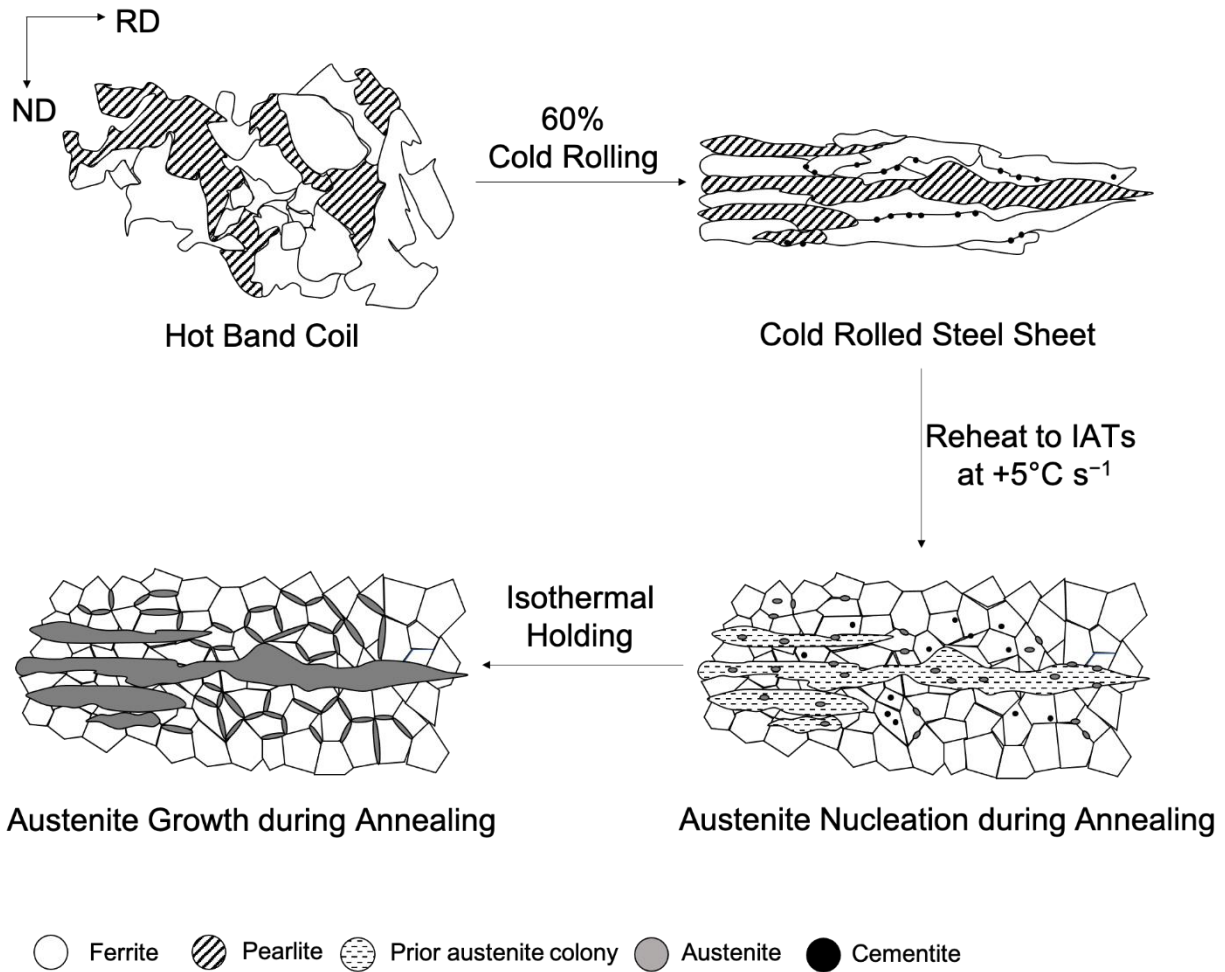


**Figure 7.11 Schematic illustration of microstructural evolution of candidate DP steels during intercritical annealing.**

In this chapter, a JAMK model was utilized to study reversed austenite growth in the  $\alpha + \gamma$  two-phase region. The results in Table 7.4 indicate that the Avrami exponents ( $n$ ) of JMAK model for austenite formation fall in the range 0.72–0.81, all below 1. The formation of intercritically annealed austenite is considered to be diffusion-controlled growth and decreasing nucleation rate [173]. The  $n$  values range from 0.5 to 2.5 in the case of diffusion-controlled growth [174]. For example, a value of 2.5 for Avrami coefficient ( $n$ ) indicates three-dimensional growth and constant nucleation rate [175]. However, the value of  $n$  will fall to about 1 or lower as the nucleation rate

decreases [173]. Numerous studies [165,167,169,176] have attempted to study the kinetics of reversed austenite formation by using JMAK model. Etesami et al. [167] reported that the  $n$  value of austenite formation for Fe-1.39Ni-0.7Mn-0.14C DP steel was below 1. Concerning the kinetics of austenite formation investigated by Kohout [169], the  $n$  values of ferritic nodular cast iron were determined, ranging from 0.6 to 1.3. Guo et al. [176] mentioned that the Avrami exponent of 18 wt.%Ni-C250 maraging steel was 0.97. Asadi Asadabad et al. [165] confirmed that the results of Avrami coefficient ( $n$ ) for Fe-1.3Mn-0.11C, varying with temperature, were 0.7–0.9. Another interesting finding in this research is that the Avrami exponent ( $n$ ) reduces from 0.81 to 0.72 with increasing Al contents from 0.04 wt.% to 0.8 wt.%.

The results of the apparent activation energy ( $Q$ ) study for austenite formation, varying with Al contents, of steel conditions of LLL (0.04 wt.%), MLL (0.4 wt.%) and HLL (0.8 wt.%) are 422.9 kJ mol<sup>-1</sup>, 436.5 kJ mol<sup>-1</sup> and 496.7 kJ mol<sup>-1</sup>, respectively, Table 7.4. These values are all much larger than the values of  $Q$  for carbon diffusion in both ferrite (84.1 kJ mol<sup>-1</sup> [177]) and austenite (157.0 kJ mol<sup>-1</sup> [178]). This is due to the existence of alloying elements, i.e., Mn, Cr, Si and Al in this study. Mn, the austenite stabilizer, lowers carbon diffusivity in austenite [13], thus increasing the apparent activation energy. Cr, a carbide-forming element, retards carbon diffusion in austenite, since there is attractive interaction between Cr and C atoms [179], hence increasing the activation energy. The finding that Al contents increase the values of  $Q$  indicates that Al content decreases carbon diffusivity in austenite, which is in agreement with Babu and Bhadeshia's observation [179].

The growth of austenite nuclei from the prior pearlite colonies is triggered by carbon diffusion from austenite/ cementite boundary through austenite and from ferrite/ cementite boundary through ferrite to ferrite/austenite boundary, resulting in the transformation of the  $\alpha$ -Fe

lattice to the  $\gamma$ -Fe lattice [171,172]. The growth rate of austenite generated from pearlite is dominated by carbon diffusion in austenite at high IATs and the diffusion of substitutional alloying elements at low IATs [9]. The growth rate of austenite from pearlite is rapid, due to the adequate carbon remaining in the prior pearlite colonies. Additionally, the subsequent austenite growth at recrystallized ferrite/ ferrite boundaries is due to carbon diffusion through a long distance from carbon-rich prior pearlite colonies to the carbon-limited recrystallized ferrite areas [164]. In this study, the results in Table 7.4 indicate that Al contents increase the activation energy and lower carbon diffusivity in austenite. Since in Wycliffe et al.'s work [180], austenite growth rate was directly related to carbon diffusivity in austenite. As a result, Al content at a high level will suppress austenite growth during intercritical annealing.

### 7.3 Conclusions

In this chapter, three steel conditions of LLL (0.04Al-0.06V-CT580°C), MLL (0.4Al-0.06V-CT580°C) and HLL (0.8Al-0.06V-CT580°C) were investigated to study the austenite formation during intercritical annealing. The new findings can be summarized as follows.

(1) Al contents raise both  $A_1$  and  $A_3$  temperatures and expands  $\alpha + \gamma$  two phase temperature region. Especially for the DP steels containing 0.8 wt.% Al, the  $A_3$  can reach 911.7°C and the range between  $A_1$  and  $A_3$  temperatures is about 187.5 °C, indicating that a higher IAT is needed for DP steels with 0.8 wt.% Al, in order to obtain the similar amount of intercritically formed austenite, compared with that of other DP steels.

(2) The increase in Al contents increases  $F_s$  temperature and expands the ferrite formation zone. Also, Al contents lower austenite hardenability and increase critical cooling rate, which

means that the formation of new ferrite and bainite, with regard to high Al bearing DP steels, cannot be avoided during a conventional industrial cooling path.

(3) The determined parameters of JMAK models for austenite formation show that Avrami exponent ( $n$ ) decreases and activation energy ( $Q$ ) increases with increasing Al content. The difference in apparent activation energy ( $Q$ ) of the three different Al bearing DP steels indicates that Al additions lower carbon diffusivity in austenite. Since austenite growth in DP steels is diffusion-controlled process, Al contents retard austenite growth during intercritical annealing.

## 8.0 Microstructure - Property Relationship Study

### 8.1 Results

#### 8.1.1 Final Microstructures after Full CGL Simulations <sup>4</sup>

The final microstructures of CGL simulated fully annealed DP steels with GI and SC anneals, produced on a Gleeble 3800 machine, are presented in Figs. 8.1 through 8.5, respectively. For example, Fig. 8.1 (a) shows the SEM micrographs of GI annealed steel condition LLL (0.04Al-<sup>4</sup>0.06V-CT580°C), consisting of ferrite, bainite and fresh martensite. The ferrite in the final microstructures of GI annealed DP steels includes old ferrite (recrystallized from the 60% cold rolled ferrite in the initial hot band during reheating from RT to the optimum IATs at a low heating rate of  $+5^{\circ}\text{C s}^{-1}$ ), and new ferrite (transformed from intercritically formed austenite during cooling from the IATs at a cooling rate of  $-15^{\circ}\text{C s}^{-1}$ ) [28]. The formation of bainite occurs during a short-time holding ( $\sim 15$  s) at the a zinc pot temperature of  $460^{\circ}\text{C}$  (near or below the  $B_s$  temperature) [28]. Fresh martensite transforms from intercritically formed austenite by quenching at a fast cooling rate of  $-10^{\circ}\text{C s}^{-1}$  from  $460^{\circ}\text{C}$  to RT. The SEM micrographs of fully annealed DP steels with SC anneal for condition LLL (0.04Al-0.06V-CT580°C) are shown in Fig. 8.1 (b). In addition to ferrite, bainite and fresh martensite mentioned above, the final microstructure of a SC annealed sample also includes tempered martensite, which formed during the up-quench to  $460^{\circ}\text{C}$  from the

---

<sup>4</sup> Much of this section appears in print: Adapted from the article published in Ref. [130], Mater. Sci. Eng. A, Volume 797, Yingjie Wu, Juha Uusitalo, Anthony J. DeArdo, Investigation of effects of processing on stretch-flangeability of the ultra-high strength, vanadium-bearing dual-phase steels, 140094, © 2020 Elsevier B.V.

fresh martensite formed by quenching from IATs to the supercooling temperature of 250°C. A large amount of fresh martensite is replaced with tempered martensite by up-quenching at a rate of +42°C s<sup>-1</sup> from the supercooling temperature to the zinc pot temperature, resulting in the increases in both TE and HER, but with the loss of UTS, which will be discussed in the following section. After the CGL simulations, the microstructural characteristics of twenty fully annealed steels with different conditions were investigated in this dissertation and are listed in Tables 8.1 and 8.2.

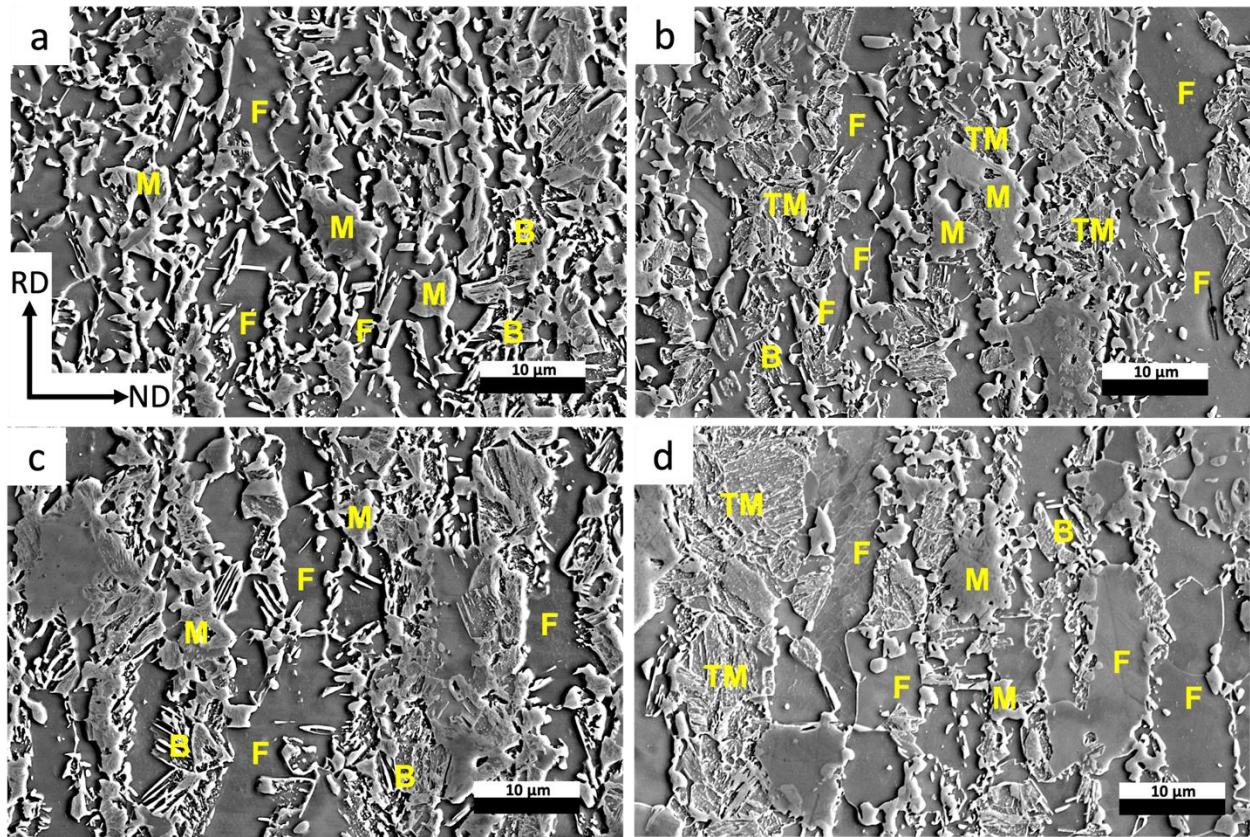


**Figure 8.1** The SEM micrographs of steel conditions LLL (0.04Al-0.06V-CT580°C) with (a) GI anneal and (b) SC anneal and LLH (0.04Al-0.06V-CT677°C) with (c) GI anneal and (d) SC anneal. Note: Ferrite is labeled by F, bainite by B, fresh martensite by M and tempered martensite by TM.

In this research, four critical variables were explored, i.e., different: (i) aluminum contents, (ii) vanadium levels, (iii) coiling temperatures, and (iv) annealing paths. From the data shown in Tables 8.1 & 8.2, the addition of Al coarsens the average ferrite grain sizes for all the steel conditions. For instance, the average ferrite grain sizes for steel condition LHL, GI (0.04 wt.% Al) and MHL, GI (0.4 wt.% Al) are 2.8  $\mu\text{m}$ , and 3.3  $\mu\text{m}$ , respectively, in Figs. 8.2 (a) & 8.4 (a). In addition, increasing the Al contents increases the volume fractions of ferrite in the final microstructures of fully annealed DP steels with GI anneals, and it also lowers the volume percentages of bainite. For example, the volume fractions of ferrite in samples LLL, GI (0.04 wt.% Al), MLL, GI (0.4 wt.% Al) and HLL, GI (0.8 wt.% Al) are 21.7%, 27.5% and 41.8%, respectively, while, the amount of bainitic structures in these three conditions decrease from 29.5% to 21.7%, and to 7.9%, in Table 8.1 and Figs. 8.1 (a), 8.3 (a) & 8.5 (a). However, the effects of Al on the microstructural features of the SC annealed samples are weak.

In addition, the influences of vanadium additions on both GI and SC annealed samples are clearly visible. In most cases, increasing the V levels from 0.06 wt.% to 0.12 wt.% refines the ferrite grain sizes. For instance, the average ferrite grain sizes of steel conditions MLH, GI (0.06 wt.% V) and MHH, GI (0.12 wt.% V) are 4.5  $\mu\text{m}$  and 4.0  $\mu\text{m}$ , respectively, in Table 8.1 and Figs. 8.3 (c) & 8.4 (c). In terms of the SC annealed DP samples LHH, SC (0.12 wt.% V), the ferrite average grain size is reduced from 4.0  $\mu\text{m}$  to 3.3  $\mu\text{m}$ , compared with steel condition LLH, SC (0.06 wt.% V), in Table 8.2 and Figs. 8.1 (d) & 8.2 (d). Furthermore, the addition of V improves the sum of the volume percentages of hard constituents (bainite, fresh martensite and tempered martensite), indicating that larger amount of intercritically formed austenite can be formed at the optimum IATs, holding for a short time (~60 s). This is evident in the case of MLL, SC (0.06 wt.% V) and

MHL, SC (0.12 wt.% V). Increasing the V levels, the total volume percentages of hard constituents increase from 69.0% to 74.3%, in Table 8.2 and Figs. 8.3 (b) & 8.4 (b).

Furthermore, the effect of two coiling temperatures (580°C and 677°C) were also investigated in this study. The volume percentages of hard constituents increase as the coiling temperature falls from 677°C to 580°C. For instance, the volume fractions of bainite and fresh martensite of MHL, GI (CT580°C) are 12.9% and 61.8%, respectively, in Table 8.1 and Fig. 8.4 (a). For fully annealed sample MHH, GI (CT677°C), the counterparts are 15.8% and 48.2%, in Table 8.1 and Fig. 8.4 (c). The total volume percentage of hard phase (bainite + fresh martensite) for MHL, GI with a low coiling temperature is higher than that for MHH, GI with a high coiling temperature.

In terms of the two annealing paths (GI and SC anneals), their effects on the final microstructures of fully annealed DP steels are apparent. The microstructures of DP steels with GI anneals include ferrite, bainite and fresh martensite. However, a considerable amount of fresh martensite is replaced with the relatively soft tempered martensite observed in the final microstructures of SC annealed DP steels. The microstructural features of samples LLL, GI and LLL, SC illustrate this point clearly, Tables 8.1 & 8.2 and Figs 8.1 (a) & (b). The only difference between these two samples is the annealing path. The volume fraction of fresh martensite of LLL, GI is 48.8% with the absence of tempered martensite, while the volume percentages of fresh martensite and tempered martensite of LLL, SC are 19.0% and 43.2%, respectively. The replacement of fresh martensite with tempered martensite leads to the large differences in the mechanical properties (i.e., UTS, TE and HER) between GI and SC annealed DP steels, observed in Tables 8.1 and 8.2, and which will be discussed in the following section.

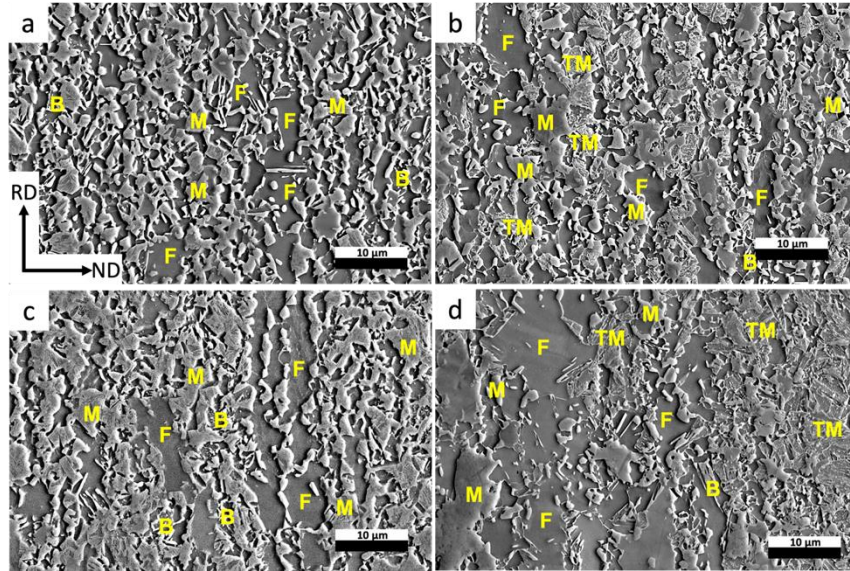


Figure 8.2 The SEM micrographs of steel conditions LHL (0.04Al-0.12V-CT580°C) with (a) GI anneal and (b) SC anneal and LHH (0.04Al-0.12V-CT677°C) with (c) GI anneal and (d) SC anneal. Note: Ferrite is labeled by F, bainite by B, fresh martensite by M and tempered martensite by TM.

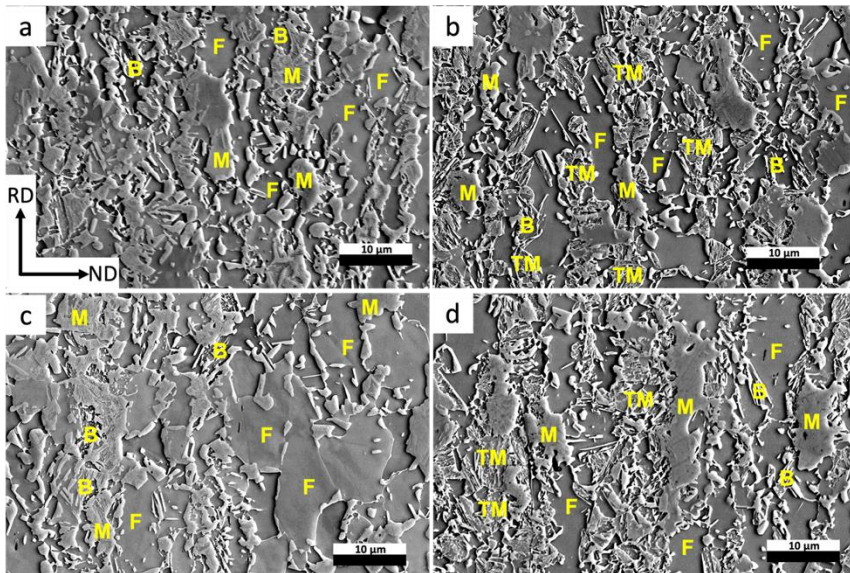


Figure 8.3 The SEM micrographs of steel conditions MLL (0.4Al-0.06V-CT580°C) with (a) GI anneal and (b) SC anneal and MLH (0.04Al-0.06V-CT677°C) with (c) GI anneal and (d) SC anneal. Note: Ferrite is labeled by F, bainite by B, fresh martensite by M and tempered martensite by TM.

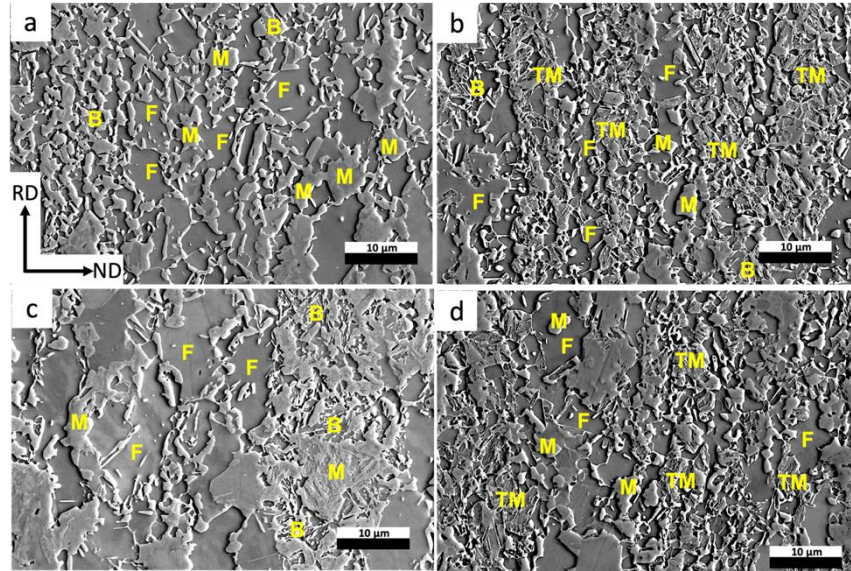


Figure 8.4 The SEM micrographs of steel conditions MHL (0.4Al-0.12V-CT580°C) with (a) GI anneal and (b) SC anneal and MHH (0.04Al-0.12V-CT677°C) with (c) GI anneal and (d) SC anneal. Note: Ferrite is labeled by F, bainite by B, fresh martensite by M and tempered martensite by TM.

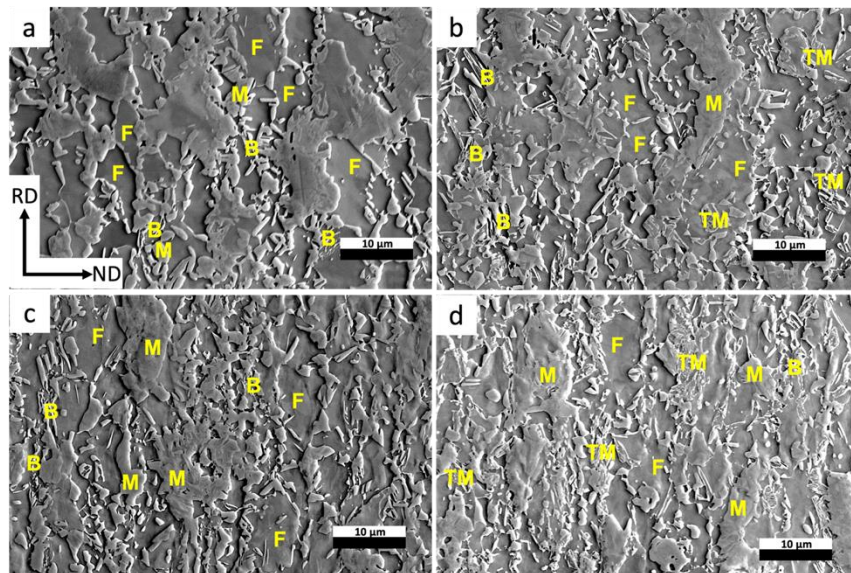


Figure 8.5 The SEM micrographs of steel conditions HLL (0.8Al-0.06V-CT580°C) with (a) GI anneal and (b) SC anneal and HLH (0.8Al-0.06V-CT677°C) with (c) GI anneal and (d) SC anneal. Note: Ferrite is labeled by F, bainite by B, fresh martensite by M and tempered martensite by TM.

**Table 8.1 The microstructural features (ferrite grain sizes ( $d_{(\alpha)}$ ) and volume percentages of ferrite ( $f_{V(\alpha)}$ ), bainite ( $f_{V(B)}$ ) and fresh martensite ( $f_{V(M)}$ ) of GI annealed samples with different pre-annealing conditions.**

IDs	$d_{(\alpha)}$ ( $\mu\text{m}$ )	$f_{V(\alpha)}$ (%)	$f_{V(B)}$ (%)	$f_{V(M)}$ (%)
LLL, GI	$3.1 \pm 1.6$	21.7	29.5	48.8
LLH, GI	$3.7 \pm 2.2$	28.2	29.0	42.8
LHL, GI	$2.8 \pm 1.3$	19.1	16.6	64.2
LHH, GI	$3.5 \pm 2.0$	19.5	19.8	60.8
MLL, GI	$3.4 \pm 1.7$	27.5	21.7	50.7
MLH, GI	$4.5 \pm 2.4$	35.5	14.1	50.4
MHL, GI	$3.3 \pm 1.7$	25.3	12.9	61.8
MHH, GI	$4.0 \pm 2.3$	36.0	15.8	48.2
HLL, GI	$5.0 \pm 1.9$	41.8	7.9	50.3
HLH, GI	$5.4 \pm 2.4$	44.3	9.4	46.3

**Table 8.2 The microstructural features (ferrite grain sizes ( $d_{(\alpha)}$ ) and volume percentages of ferrite ( $f_{V(\alpha)}$ ), bainite ( $f_{V(B)}$ ), fresh martensite ( $f_{V(M)}$ ) and tempered martensite ( $f_{V(TM)}$ ) of SC annealed samples with different pre-annealing conditions.**

IDs	$d_{(\alpha)}$ ( $\mu\text{m}$ )	$f_{V(\alpha)}$ (%)	$f_{V(B)}$ (%)	$f_{V(M)}$ (%)	$f_{V(TM)}$ (%)
LLL, SC	$3.3 \pm 1.7$	30.3	7.5	19.0	43.2
LLH, SC	$4.0 \pm 2.5$	30.3	11.1	25.6	30.1
LHL, SC	$2.6 \pm 1.5$	25.7	8.9	23.8	41.6
LHH, SC	$3.3 \pm 2.1$	30.1	10.4	25.3	34.1
MLL, SC	$3.4 \pm 1.9$	31.0	12.7	27.5	28.9
MLH, SC	$4.3 \pm 3.0$	35.5	9.2	26.1	29.2
MHL, SC	$3.1 \pm 1.6$	26.2	8.4	27.5	37.9
MHH, SC	$3.6 \pm 1.8$	33.4	16.8	25.9	27.5
HLL, SC	$4.7 \pm 2.1$	32.9	10.2	48.2	8.6
HLH, SC	$5.2 \pm 2.3$	39.4	5.7	43.4	11.5

### 8.1.2 Tensile Properties

The tensile properties of fully annealed DP steels with all steel conditions are listed in Tables 8.3 and 8.4. The engineering stress vs engineering strain flow curves and comparisons of major tensile properties (yield strength, ultimate tensile strength and total elongation) for fully annealed DP steels with both GI and SC anneals are plotted in Fig. 8.6.

The essential feature of DP steels in flow curves is continuous yielding or the absence of yield point elongation (YPE), Fig. 8.6. Also, low YS/UTS ratio is another distinctive characteristic, which can be as low as 0.46–0.53 (GI anneals, Table 8.3) and 0.46–0.58 (SC anneals, Table 8.4).

The highest YS observed is 604.1 MPa for the steel condition of LHL (0.04Al-0.12V-CT580°C) with GI anneal, Table 8.3, and 583.6 MPa for LHL, SC, Table 8.4. Except for different annealing paths, these two steel conditions shared the same composition and coiling temperature. In terms of the effect of Al on YS, the YS decreases with increasing Al contents from 0.04 wt. % to 0.8 wt.%, Tables 8.3 & 8.4 and Figs. 8.6 (a), (c) & (e). For example, the YS results of steel conditions of LLL, GI (0.04 wt.% Al), MLL, GI (0.4 wt.% Al) and HLL, GI (0.8 wt.%) are 530.3 MPa, 512.5 MPa and 494.2 MPa, respectively. Additionally, V additions enhance YS values. For instance, concerning GI annealed DP steels of MLL, GI (0.4Al-0.06V-CT580°C) and MHL, GI (0.4Al-0.12V-CT580°C), change in V levels from 0.06 wt.% to 0.12 wt.% increases YS results from 512.5 MPa to 590.0 MPa, Table 8.3. Also, for the fully annealed DP steels with SC anneals, the YS results have the similar trend.

From Table 8.3 and Fig. 8.6, the GI annealed DP steel with 0.04 wt.% Al, 0.12 wt.% V and a low coiling temperature of 580°C has the highest UTS of 1181.4 MPa. While, the highest UTS value observed for SC anneals is 1046.0 MPa for LHL, SC, Table 8.4 and Fig. 8.6. Similar to the results of YS, in terms of the steels sharing the same composition and pre-annealing condition, the

change from GI to SC anneals also reduces UTS values. From Table 8.3, for steel conditions LLL, GI (0.04 wt.% Al), MLL, GI (0.4 wt.% Al) and HLL, GI (0.8 wt.% Al), increasing Al levels from 0.04 wt.% to 0.8 wt.%, the UTS values reduce from 1092.8 MPa to 1061.4 MPa. It is apparent that UTS decreases with increasing Al contents. Concerning the effect of V on UTS, the increase in V levels from 0.06 wt.% to 0.12 wt.% results in higher martensite volume fraction and more VC precipitates, hence improving UTS, Figs. 8.6 (a) vs (b) or 8.6 (c) vs (d). In terms of effect of pre-annealing condition (i.e., coiling temperature) on UTS, a higher UTS can be obtained for the candidate DP steels with a low coiling temperature of 580°C. For example, UTS results of steel conditions MLL, GI (CT580°C) and MLH, GI (CT677°C) are 1086.0 MPa and 1059.0 MPa, respectively.

In the case of TE, the highest results of the fully annealed DP steels are 25.3% for HLH (0.8Al-0.06V-CT677°C) with GI anneal and 25.0% for HLH with SC anneal, as shown in Tables 8.3 and 8.4. The product of  $UTS \times TE$ , a ductility index for automotive steels, is also listed in Tables 8.3 and 8.4. The highest product of  $UTS \times TE$  for the fully annealed DP steels with GI anneal is 25,449.3 MPa  $\times$  % for HLH, GI (0.8Al-0.06V-CT677°C). While, with regard to SC anneals, the highest product is 24,040.0 MPa  $\times$  %. Both of these two products belong to the 3<sup>rd</sup> generation AHSS family ( $>22,000$  MPa  $\times$  %) [34,46].

**Table 8.3 Tensile properties (yield strength (YS), ultimate tensile strength (UTS), yield to tensile strength ratio (YS/UTS), uniform elongation (UE), total elongation (TE), post uniform elongation (Post UE), reduction in area (RA), and product of UTS × TE) of the fully annealed DP steels with the GI anneal.**

IDs	YS (MPa)	UTS (MPa)	YS/UTS	UE (%)	TE (%)	Post UE (%)	RA (%)	UTS × TE (MPa × %)
LLL, GI	530.3	1092.8	0.49	12.3	20.8	8.5	27.5	22730.2
LLH, GI	542.3	1039.1	0.52	12.6	17.9	5.3	16.6	18599.9
LHL, GI	604.1	1181.4	0.51	11.0	19.1	8.1	22.6	22564.7
LHH, GI	574.9	1099.8	0.52	11.1	16.2	5.1	13.6	17816.8
MLL, GI	512.5	1086.0	0.47	11.6	19.5	8.0	29.6	21177.0
MLH, GI	528.3	1059.0	0.50	11.0	14.9	3.9	24.1	15779.1
MHL, GI	596.0	1168.2	0.51	10.2	17.8	7.6	24.6	20794.0
MHH, GI	576.0	1096.9	0.53	10.9	16.6	5.7	18.5	18208.5
HLL, GI	494.2	1061.4	0.47	13.4	22.0	8.6	25.6	23350.8
HLH, GI	463.3	1005.9	0.46	14.8	25.3	10.5	22.9	25449.3

**Table 8.4 Tensile properties (yield strength (YS), ultimate tensile strength (UTS), yield to tensile strength ratio (YS/UTS), uniform elongation (UE), total elongation (TE), post uniform elongation (Post UE), reduction in area (RA), and product of UTS × TE) of the fully annealed DP steels with the SC anneal**

IDs	YS (MPa)	UTS (MPa)	YS/UTS	UE (%)	TE (%)	Post UE (%)	RA (%)	UTS × TE (MPa × %)
LLL, SC	518.2	974.7	0.53	11.9	22.2	10.3	36.6	21638.3
LLH, SC	545.4	936.5	0.58	11.2	19.6	8.5	33.4	18355.4
LHL, SC	583.6	1046.0	0.56	10.1	19.0	8.9	29.5	19874.0
LHH, SC	542.1	972.7	0.56	10.9	19.2	8.3	26.0	18675.8
MLL, SC	502.0	973.7	0.52	11.7	22.3	10.5	33.3	21713.5
MLH, SC	494.6	950.5	0.52	12.0	19.0	6.9	27.1	18059.5
MHL, SC	570.7	1040.7	0.55	10.1	17.6	7.5	34.0	18316.3
MHH, SC	522.6	975.9	0.54	12.1	20.0	7.9	26.8	19518.0
HLL, SC	459.9	983.9	0.47	14.1	24.2	10.0	29.4	23810.4
HLH, SC	444.3	961.6	0.46	15.3	25.0	9.7	23.6	24040.0

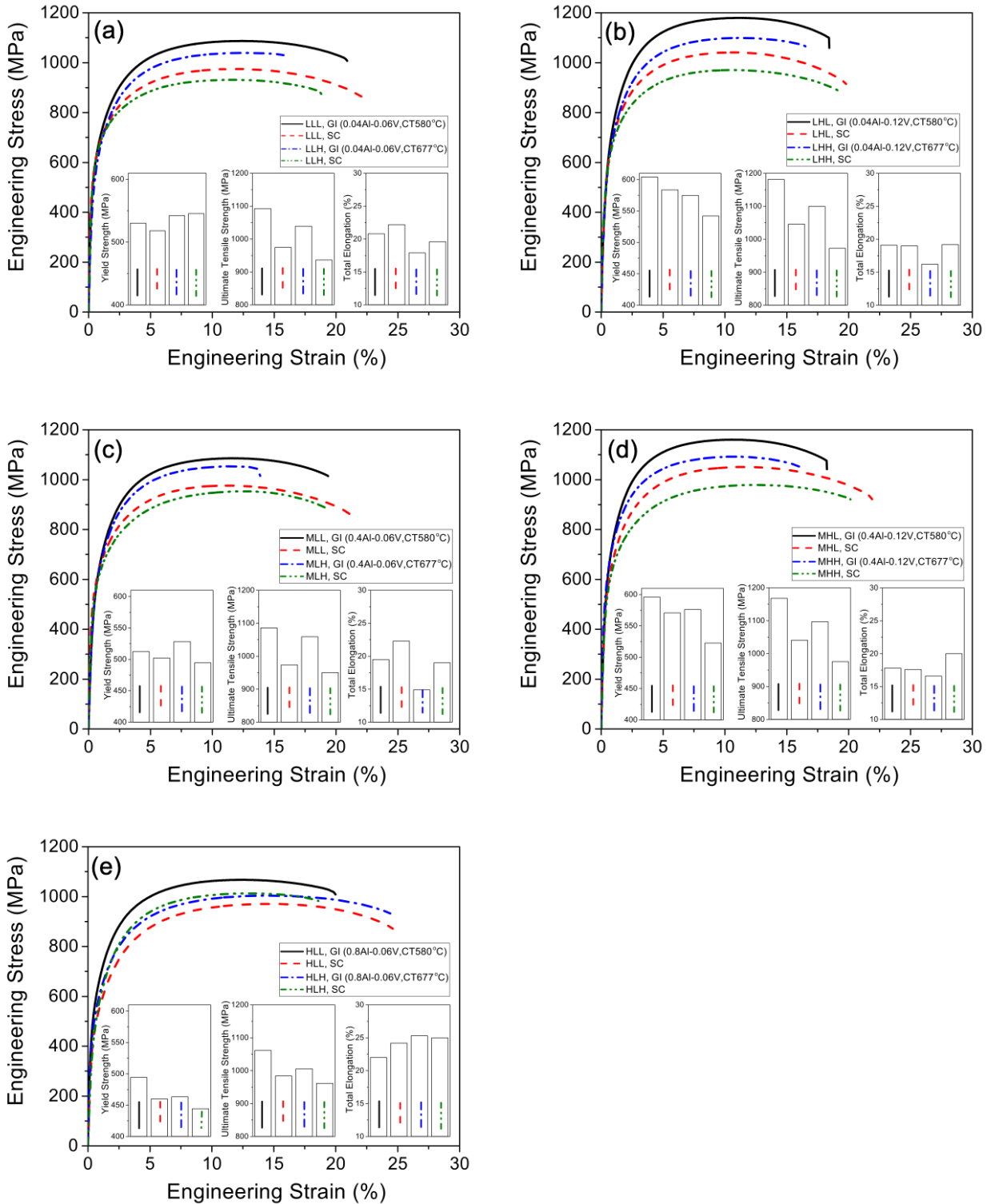


**Figure 8.6 Engineering vs engineering strain flow curves and comparisons of major tensile properties (yield strength, ultimate tensile strength and total elongation) for fully annealed DP steels with both GI and SC anneals.**

## 8.2 Discussion

### 8.2.1 Effects of Pre-Annealing Conditions on Ferrite Grain Sizes

The effects of pre-annealing conditions (i.e., compositions and coiling temperatures) on ferrite grain sizes of fully annealed DP steels with both GI and SC anneals have been investigated and plotted in Fig. 8.7, based on data listed in Tables 8.1 and 8.2. For both anneals, ferrite grains can be refined by decreasing Al levels (from 0.8 wt.% to 0.04 wt.%), coiling temperatures (from 677°C to 580°C) or increasing V contents (from 0.06 wt.% to 0.12 wt.%).

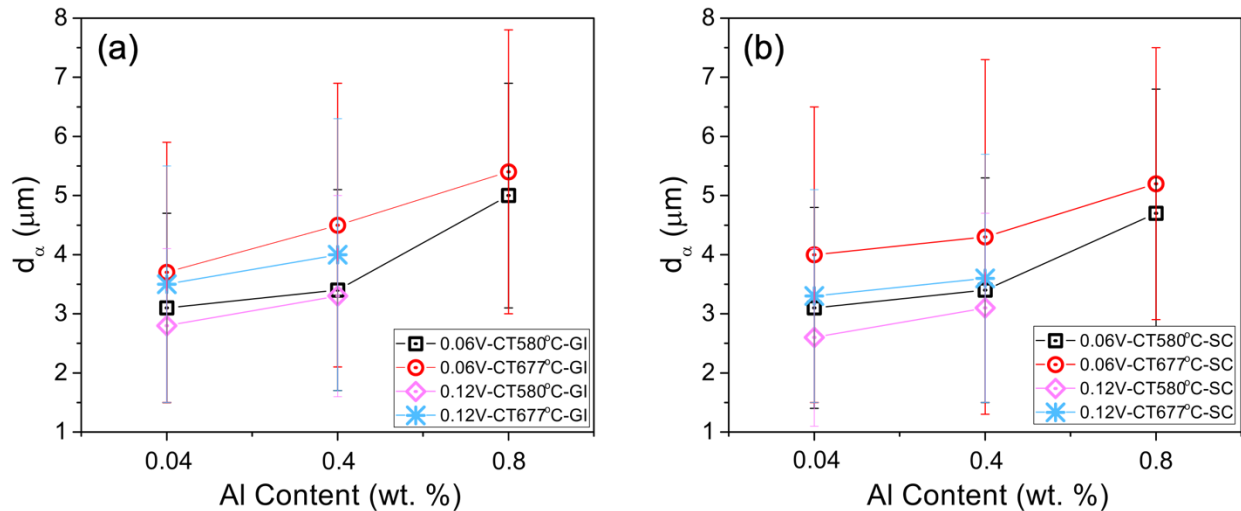


Figure 8.7 Effects of pre-annealing conditions on average ferrite grain sizes of the fully annealed DP steels with both (a) GI and (b) SC anneals.

Al additions coarsen ferrite grains in the ferrite-martensite DP steels, which is in agreement with the observations in magnetic shielding steels [181] and Nb-bearing IF steels [182]. Al additions enhance both  $A_1$  and  $A_3$  temperatures and expand dramatically  $\alpha + \gamma$  two phase region, Fig. 7.1 and Table 7.1. The increase in Al levels raises ferrite nucleation rate and meanwhile also

accelerates the ferrite grain coarsening process for high Al steels [183], especially at high IATs. In this research, in order to obtain a similar amount of austenite, higher IATs need to be chosen for high Al steels. The IATs for candidate steels with 0.04 wt.%, 0.4 wt.% and 0.8 wt.% Al were 780°C, 800°C and 820°C, respectively. Ferrite recrystallization was complete quickly during reheating to the high IATs, followed by grain coarsening, so coarse ferrite grains can be observed in the final microstructures of high Al steels.

The initial microstructures of the hot bands with a low coiling temperature of 580 °C mainly consist of pearlite and acicular ferrite ( $4.44 \mu\text{m} < d_{\alpha} < 5.68 \mu\text{m}$ ). While, the starting microstructures of the hot bands coiled at 677°C are banded pearlite-polygonal ferrite aggregates ( $6.08 \mu\text{m} < d_{\alpha} < 9.22 \mu\text{m}$ ). Compared with coarse polygonal ferrite, refined acicular ferrite has a higher value of  $S_v$  (interfacial area per unit volume), offering more ferrite nucleation sites for recrystallization during intercritical annealing. In addition, cold rolled DP steels with the combination of low coiling temperature and 60% cold reduction has more stored energy, which may provide more driving force for ferrite recrystallization. Thus, the difference in ferrite grain sizes of hot bands coiled at different temperatures remained even after ferrite recrystallization.

## **8.2.2 Influences of Pre-Annealing Conditions and Annealing Paths on the Fraction of Hard Constituents**

Fig. 8.8 shows the influences of pre-annealing conditions and annealing paths on fraction of hard constituents (i.e., bainite, fresh martensite and tempered martensite) of the fully annealed DP steels with both GI and SC anneals. From Fig. 8.8, the total volume fraction of these hard constituents increases with decreasing Al levels and coiling temperatures or increasing V contents.

Basically, as mentioned earlier, the change in annealing paths from GI to SC anneals results in the microstructural replacement of a large amount of fresh martensite by tempered martensite.

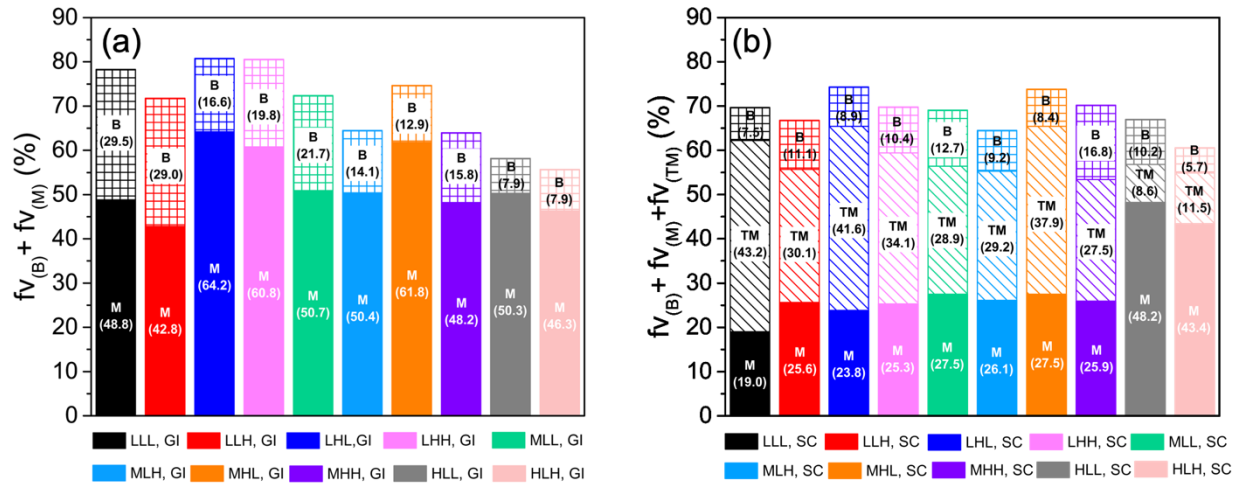


**Figure 8.8** Effects of pre-annealing conditions and annealing paths on the amount of hard constituents of the fully annealed DP steels with both (a) GI and (b) SC anneals.

Al is a ferrite stabilizer element and it increase the transformation temperature of  $\gamma \rightarrow \alpha$ , so higher IATs are required to obtain enough intercritically formed austenite. The high Al addition lowers austenite stability and new ferrite formation cannot be avoided during intercritical annealing even at a higher cooling rate (i.e.,  $-100 \text{ }^\circ\text{C s}^{-1}$ ), both of which act to reduce the amount of fresh martensite.

Similar to the pinning effect of Nb [21], additions of V retard the ferrite recrystallization during intercritical annealing, thus accelerating the nucleation and growth of intercritically formed austenite. In Table 6.1 and Fig. 6.2, additions of V refine the ferrite grains in the initial microstructures of hot band coils and cold rolled steel sheets, combined with the effect of V on ferrite recrystallization during intercritical annealing, a large number of ferrite/ferrite grain

boundaries caused by a higher V levels create more austenite nucleation sites, which is beneficial to the intercritical austenitization process.

### **8.2.3 Consequences of Pre-Annealing Conditions and Annealing Paths on Strength**

The YS is related to the mobile dislocation density or the resistance to dislocation movement in ferrite [184], which means low YS of DP steels is ascribed to highly mobile dislocations or low resistance to dislocation movement. From Tables 8.1 and 8.2, Al additions decrease the martensite volume percentages in the final microstructure of the fully annealed DP steels. The interfaces between ferrite/ martensite is considered as the new source for new mobile dislocations even at small strains [21]. So, the increase in martensite volume fraction results in the improvement of YS. In addition to the benefit of V on martensite volume percentages, compared with the DP steels containing 0.06 wt.% V, more VC would be expected to be precipitated in the ferrite matrix for the 0.12 wt.% V alloyed DP steels. More VC precipitates suppress the movement of mobile dislocation, hence leading to a higher YS. The influences of annealing paths on YS are also attributed to the amount of martensite. The change of annealing path from GI to SC anneal results in the replacement of fresh martensite with tempered martensite. Tempering in SC anneals cause residual relaxation for DP steels. These reasons mentioned above enable the candidate DP steels with 0.04 wt.% Al, 0.12 wt.% V, a low coiling temperature of 580 °C and GI anneal to result in higher martensite volume fraction and the highest YS of 604.1 MPa.

Previous researches [5–8] pointed out that the tensile strength of DP steels had a positive linear relationship with martensite volume percentages. In those studies, the final microstructure after intercritical annealing consisted only of two phases, ferrite and fresh martensite. However, in most cases, due to the hardenability of austenite, intercritical annealing temperatures, cooling rates

or complex annealing procedures, the final microstructure always contained pearlite [9], cementite [26], bainite [20,25] or tempered martensite [27–29]. Therefore, the precise structure-tensile strength relation remains unclear.

High Al levels lower the hardenability of intercritically formed austenite, and as a result, the formation of new ferrite cannot be avoided at a cooling rate of  $-15\text{ }^{\circ}\text{C s}^{-1}$  for high Al bearing DP steels, hence reducing UTS. V additions refine ferrite grains, form more VC precipitates and lead to higher volume fractions of hard constituents, resulting in the increase in UTS. In terms of effect of coiling temperature on UTS, a higher stored energy resulted from the low coiling temperature of  $580^{\circ}\text{C}$ , combined with 60% cold work, provides more driving force for austenite formation during intercritical annealing in the limited isothermal holding time. So, after fast cooling, a large amount of intercritically formed austenite transforms into fresh martensite and results in a higher UTS. Additionally, tempering occurs during SC anneals causing a large amount of tempered martensite transformed from fresh martensite, thus reducing the UTS.

Fig. 8.9 plots the relationship between strength and martensite volume percentages based on the data from Davies' works [5] and the fully annealed DP steels with GI anneals, Tables 8.1 & 8.3. It can be concluded that both yield and tensile strengths of DP steels can be expressed as functions of fresh martensite volume percentages, shown in Eqs. 8.1 and 8.2,

$$\text{YS} = 11.0 \times \text{fv}_{(\text{M})} + 84.8 \quad (8.1)$$

$$\text{UTS} = 15.9 \times \text{fv}_{(\text{M})} + 361.3 \quad (8.2)$$

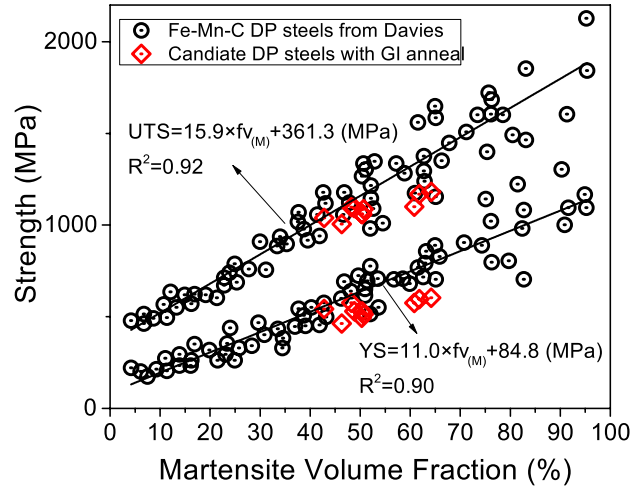


**Figure 8.9** The linear relationship between strength and martensite volume fraction based on the data from Davies’ work [5] and Tables 8.1 & 8.3.

However, fresh martensite is not the only hard constituent which can be observed in the final microstructures of the fully annealed DP steels with GI anneals. Due to the low hardenability of austenite caused by Al additions at high IATs, some portions of martensite were replaced by bainite. So, the effect of bainitic microstructures on UTS should be taken into consideration. Fig. 8.10 shows the correlations between strength and the total amount of hard constituents (i.e., bainite and fresh martensite) of the fully annealed DP steels with GI anneals. The relations can be shown as follows,

$$YS = 3.6 \times (fv_{(B)} + fv_{(M)}) + 289.2 \quad (8.3)$$

$$UTS = 4.1 \times (fv_{(B)} + fv_{(M)}) + 799.6 \quad (8.4)$$

Compared with the linear relations obtained from Fig. 8.9, the slopes of two straight lines from Fig. 8.10 are much lower. This indicates that the hardening effect of bainite on the UTS of DP steels is considerably lower than that of fresh martensite. Fonstein et al. [185] statistically

summarized the effect of bainite on the UTS and found that the replacement of 10% of martensite by bainite caused the reduction in UTS by 40 MPa in ferrite-bainite-martensite AHSS.

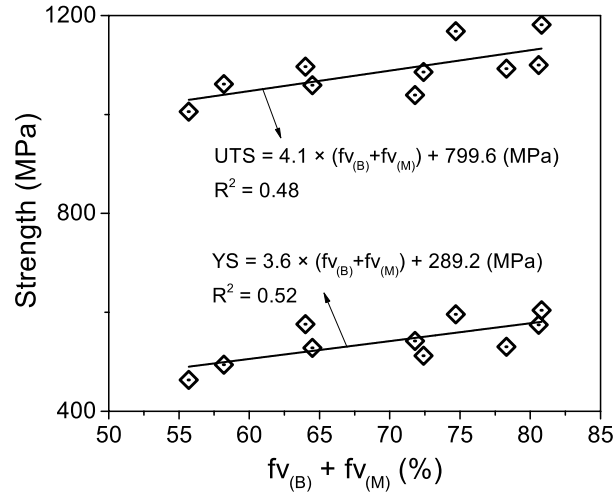


**Figure 8.10** The relationship between strength and volume percentages of hard constituents of the fully annealed DP steels with GI anneals

### 8.2.4 Significance of V Additions and Annealing Path Conditions on Work Hardening

#### Behavior

High strain hardening rate is another notable feature of DP steels, compared with the high strength low alloy (HSLA) steels, since this enables high uniform elongation and the possibility of increases in tensile strength during plastic deformation.

The relationship between true stress ( $\sigma$ ) and true strain ( $\epsilon$ ) can be expressed by a Hollomon-type equation, Eq. 8.5 [186],

$$\sigma = k\epsilon^n \quad (8.5)$$

where,  $n$  is work hardening exponent and  $k$  the strength coefficient. Taking the logarithm of both sides of Eq. 8.1, Eq. 8.2 is shown as follows,

$$\ln \sigma = n \ln \varepsilon + \ln k \quad (8.6)$$

so, the strain hardening exponent can be expressed as Eq. 8.5, which is called Hollomon model [186].

$$n = \frac{d \ln \sigma}{d \ln \varepsilon} \quad (8.7)$$

Fig. 8.11 presents the  $\ln \sigma - \ln \varepsilon$  curves of several selected candidate DP steels. From Fig. 8.11, nonlinear variations in  $\ln \sigma - \ln \varepsilon$  plots show that the work hardening exponent ( $n$ ) decreases as true strain increases during plastic deformation. Two evident working hardening exponents ( $n_1$  and  $n_2$ ) are discerned in  $\ln \sigma - \ln \varepsilon$  curves, and  $n_1$  is larger than  $n_2$ . These findings indicate that the investigated DP steels followed a two-stage work hardening mechanism during plastic deformation, which is in agreement with previous investigations [187–190]. These works were reported that ferrite was initially plastically deformed in the first stage and martensite was then deformed with the work hardened ferrite in the second stage [187–190].

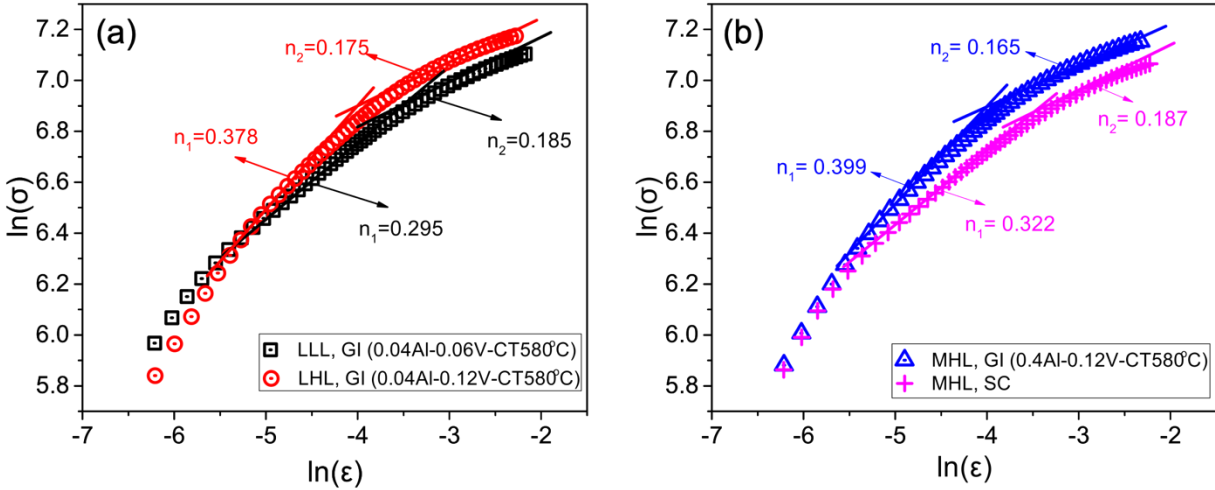


**Figure 8.11**  $\ln\sigma - \ln\epsilon$  curves of steel conditions of (a) LLL, GI vs LHL, GI and (b) MHL, GI vs MHL, SC

Table 8.5 lists strain hardening exponents at the two stages  $n_1$  ( $\epsilon=0.007$ ) and  $n_2$  ( $\epsilon=0.05$ ) of the fully annealed DP steels with both GI and SC anneals. From Table 8.5, it is apparent that V additions enhance  $n_1$  values. For example, in terms of steel conditions of LLL, GI (0.04Al-0.06V-CT580°C) and LLL, GI (0.04Al-0.12V-CT580°C), the increase in V contents from 0.06 wt.% to 0.12 wt.% results in a 28% increase in  $n_1$  ( $\epsilon=0.007$ ), Table 8.5 and Fig. 8.11 (a). Also, for the SC annealed DP steels, the  $n_1$  results of steel conditions of MLH, SC (0.4Al-0.06V-CT677°C) and MHL, SC (0.4Al-0.12V-CT677°C) are 0.277 and 0.310, respectively, Table 8.5. These results indicate that at the early stage of plastic deformation, ferrite was effectively work hardened for candidate DP steels containing a high V level, which is probably due to the pinning effects of vanadium carbides on retarding mobile dislocation movements. However, regarding the strain hardening behavior in the second stage, the results of  $n_2$  ( $\epsilon=0.05$ ) of highly V alloyed DP steels are slightly lower than those of DP steels with a low V content. This may result from the finer ferritic microstructures caused by a high V addition of 0.12 wt.%, and the mean free path among dislocations for DP steels with 0.12 wt.% V is shorter than that of DP steels containing 0.06 wt.%

V. The lower the mean free path is, the higher is the possibility of annihilation of dislocations [34] will be, resulting in slightly lower  $n_2$  values at large strains for highly V microalloyed DP steels.

In terms of the influence of annealing paths on strain hardening exponents, in most cases, the  $n_1$  ( $\epsilon=0.05$ ) values of GI annealed DP steels are larger, compared with those of fully annealed DP steels with the SC anneal. For example,  $n_1$  values of steel conditions of MHL, GI (0.4Al-0.12V-CT580°C) and MHL, SC are 0.399 and 0.322, respectively, Table 8.5 and Fig. 8.11 (b), which is similar to Brofin et al.'s work, in that the replacement of martensite by bainite led to the decrease in the initial strain hardening rate [25]. Regarding GI annealed DP steels, the existence of a high density of highly mobile dislocations in the ferrite close to ferrite/ fresh martensite interfaces is caused by the strains in the ferrite from both the volume expansion that accompanies the transformation of austenite to martensite and the shear nature of the transformation itself. However, after tempering in the SC anneals, the replacement of a large amount of fresh martensite with tempered martensite results in the reduction in mobile dislocation density and the relaxation of residual stress. These concepts might be used to explain the difference in  $n_1$  ( $\epsilon=0.007$ ) of both GI and SC annealed steels.

**Table 8.5 Calculated strain hardening exponents from the true flow curves of the fully annealed DP steels  
with both GI and SC anneals**

IDs	n <sub>1</sub>	n <sub>2</sub>	IDs	n <sub>1</sub>	n <sub>2</sub>
	(ε=0.007)	(ε=0.05)		(ε=0.007)	(ε=0.05)
LLL, GI	0.295	0.185	LLL, SC	0.246	0.181
LLH, GI	0.364	0.190	LLH, SC	0.253	0.161
LHL, GI	0.378	0.175	LHL, SC	0.331	0.173
LHH, GI	0.371	0.182	LHH, SC	0.313	0.170
MLL, GI	0.377	0.189	MLL, SC	0.256	0.188
MLH, GI	0.375	0.186	MLH, SC	0.277	0.197
MHL, GI	0.399	0.165	MHL, SC	0.322	0.187
MHH, GI	0.354	0.169	MHH, SC	0.310	0.192
HLL, GI	0.322	0.194	HLL, SC	0.325	0.227
HLH, GI	0.299	0.209	HLH, CS	0.265	0.228

### 8.2.5 Strength - Ductility Considerations of DP Steels

UE is the uniform elongation expressed as engineering strain. It is also the elongation at the maximum load, which can be controlled by the strain hardening exponent (n), as shown in Fig. 8.12 (a). Fig. 8.12 (a) plots the correlation between UE and n<sub>2</sub> (ε=0.05) of the fully annealed DP steels with both GI and SC anneals, which can be expressed by Eq. 8.8,

$$UE = 71.1 \times n_2 - 1.4 \quad (8.8)$$

The correlation coefficient ( $R^2$ ) of UE vs  $n_2$  ( $\epsilon=0.05$ ) is 0.74, indicating a relatively strong positive linear relation exists between UE and  $n_2$  ( $\epsilon=0.05$ ). These results show that high UE or global ductility can be expected by a high strain hardening ratio. Additionally, Fig. 8.12 (b) shows that UE can be expressed as a function of UTS from the results in Davies' work [1] and Tables 8.3–8.5. The results of UE fall with increasing UTS. In Fig. 8.12 (b) the candidate DP steels with both GI and SC anneals have superior ductility, at the same strength level, compared with that of Fe-Mn-C DP steels in Davies' study. This combination of high strength and high global ductility makes these candidate DP steels commercially attractive. Fig. 8.13 presents the UTS vs TE curves of automotive steels. The products of UTS  $\times$  TE for all the conditions studied in this research were included in this plot, indicating that all these candidate DP steels belong to ultra-high strength steels (UTS > 700 MPa), and the majority belong to the 3<sup>rd</sup> generation AHSS family (defined by UTS  $\times$  TE > 22,000 MPa  $\times$  %).

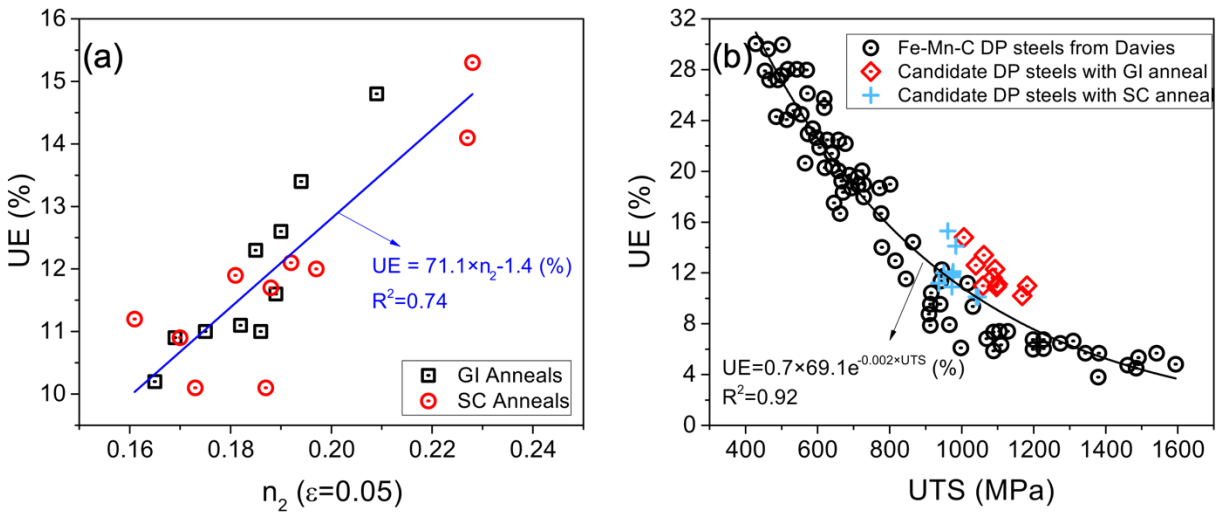


Figure 8.12 The plots of (a) UE vs  $n_2$  ( $\epsilon=0.05$ ) based on data from Tables 8.3–8.5 and (b) UE vs UTS from the results in Davies' work [5] and Tables 8.3–8.5.



(4) The combination of a low coiling temperature of 580°C and 60% cold reduction refines ferrite grains, increase fresh martensite volume percentages and improves UTS, which is due to a higher stored energy generated from the high dislocation densities caused by acicular ferrite (low temperature ferrite) transformation in hot band coils and 60% plastic deformation in cold rolled sheet steels.

(5) The change in annealing path from GI to SC anneals mainly results in microstructural replacement of a large amount of fresh martensite by tempered martensite. The tempering in the process of SC anneals causes mobile dislocation density reduction in the vicinity of ferrite/hard phase interfaces and residual stress relaxation, hence reducing YS and initial work hardening ratio.

## 9.0 Investigation of Hole Expansion Performance <sup>5</sup>

### 9.1 Results

#### 9.1.1 Hole Expansion Results

After the hole expansion tests, the measured HER values for all steel conditions are shown in Table 9.1.

**Table 9.1 Hole expansion ratios of fully annealed DP steels with GI and SC anneals**

IDs	HER (%)		IDs	HER (%)	
	CGL Simulations			CGL Simulations	
	GI Anneal	SC Anneal		GI Anneal	SC Anneal
LLL	17.0	27.5	LLH	14.6	24.3
LHL	14.5	22.9	LHH	11.5	22.1
MLL	17.6	26.6	MLH	17.3	22.0
MHL	17.0	23.2	MHH	13.2	23.5
HLL	19.0	21.2	HLH	17.6	17.6

<sup>5</sup> Much of this section appears in print: Adapted from the article published in Ref. [130], Mater. Sci. Eng. A, Volume 797, Yingjie Wu, Juha Uusitalo, Anthony J. DeArdo, Investigation of effects of processing on stretch-flangeability of the ultra-high strength, vanadium-bearing dual-phase steels, 140094, © 2020 Elsevier B.V.

Fig. 2.9 presents that the HER values for a variety of AHSSs that exhibit a strong relationship with several simple tensile properties, such as UTS (Fig. 2.9 (a)), Post UE (Fig. 2.9 (b)), and  $\bar{R}$  (Fig. 2.9 (c)). In Fig. 2.9 (a), HER values can be expressed as a function of UTS. The HER values of steels with low strength grades (i.e., IF, bake hardening (BH) and HSLA steels) decrease as UTS increases to 800 MPa, however, the HER data of DP, TRIP or martensitic steels do not follow this trend and keep scattered, if UTS exceeds 800 MPa. Figs. 2.9 (b) and (c) illustrate that hole expansion performances can also be positively correlated to Post UE and  $\bar{R}$ . In terms of the easily formable steels (i.e., IF, BH and HSLA steels), HER improves with increasing Post UE or  $\bar{R}$ . Nevertheless, these correlations cannot be employed for DP or TRIP steels at the higher strength levels.

In terms of the candidate DP steels studied in this dissertation, the universal trend can be obtained between each mechanical property and HER, assuming the simple uniaxial tensile properties and HER results are well correlated. Fig. 9.1 plots the relationships between tensile properties (i.e., YS, UTS, UE, TE, Post UE, RA,  $n_1$  and  $n_2$ ) and measured HER values of the fully annealed DP steels with both GI and SC anneals. It should be noted that, the results of HER only share a good positive linear relationship with RA values, and this relation is given in Eq. 9.1, with a high regression coefficient of 0.82.

$$\text{HER} = 0.67 \times \text{RA} + 1.66 \quad (9.1)$$

With the exception of RA, HER is not highly correlated with other simple uniaxial tensile properties of the candidate ultra-high strength, V-bearing DP steels, which supports the fact that the correlations between mechanical properties and HER are only valid for certain specific steels. So, the factors governing hole expansion performance need to be investigated, since they are

different from those controlling other conventional ductility or formability indices (i.e., strain rate sensitivity ( $m$ ) [191,192], strain rate exponent ( $n$ ) [193] and normal anisotropy ( $\bar{R}$ ) [194] for deep drawability).

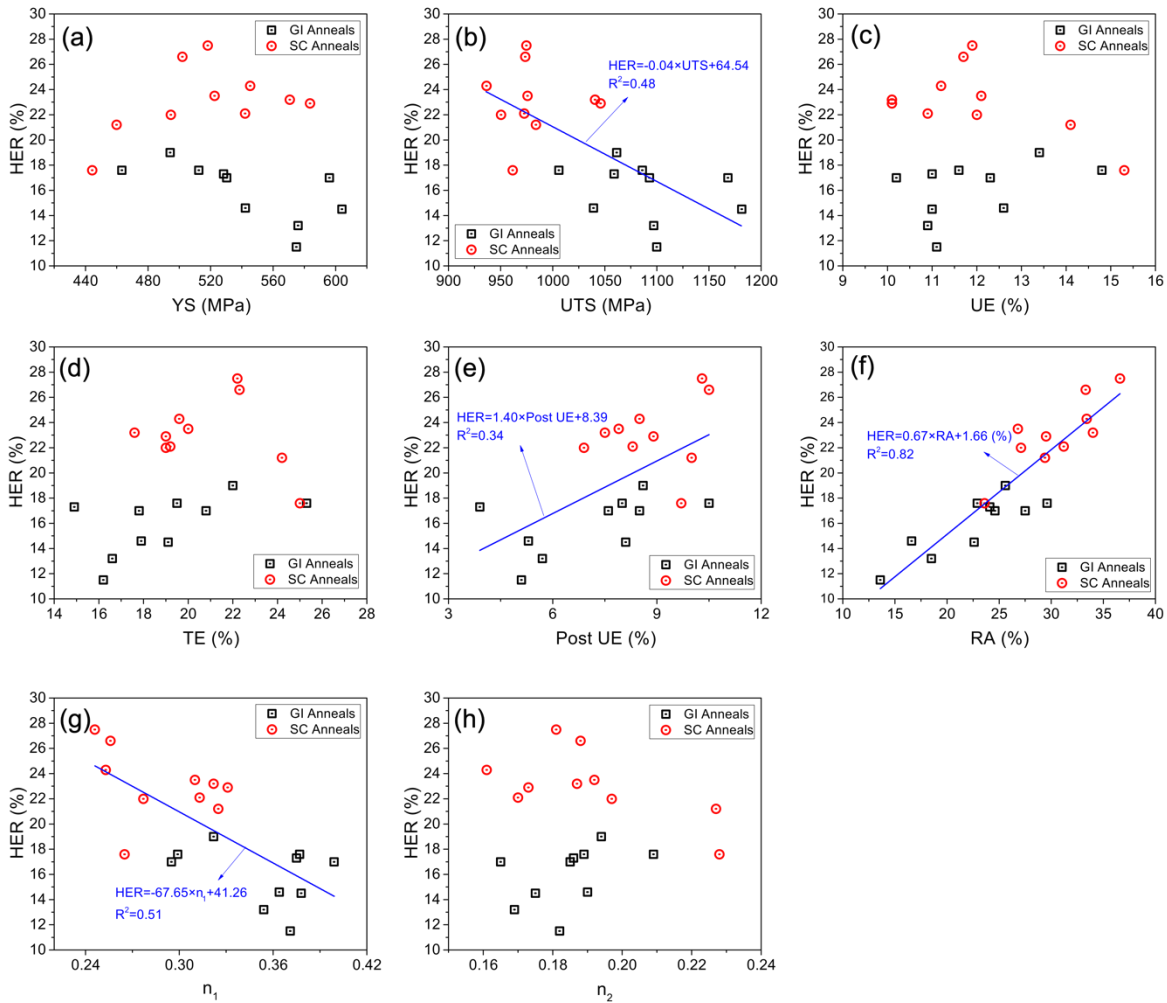


**Figure 9.1** The relations between tensile properties and measured HER values of the fully annealed DP steels: (a) YS vs HER, (b) UTS vs HER, (c) UE vs HER, (d) TE vs HER, (e) Post UE vs HER, (f) RA vs HER, (g)  $n_1$  vs HER, and (h)  $n_2$  vs HER.

### 9.1.2 Microstructure and Damage Evolutions during the Whole HET Process

The whole HET process consists of two steps, hole punching and hole expanding (Fig. 9.1). Fig. 9.1 also schematically presents the microstructure and damage evolution during the whole HET process. Before hole punching, the microstructure of a HER blank is the annealed and undeformed DP steel microstructure. Pre-strains and microstructural damages (i.e., micro-voids) are introduced at the inner surface of the initial hole during hole punching. As the hole is expanded by the conical punch at a constant rate, the shear affected zone (SAZ) is further plastically deformed. So, with further increasing plastic deformation, as the first through-thickness crack is observed in the shear surface of the final hole in the center of the HER blank, the hole expansion test is complete.

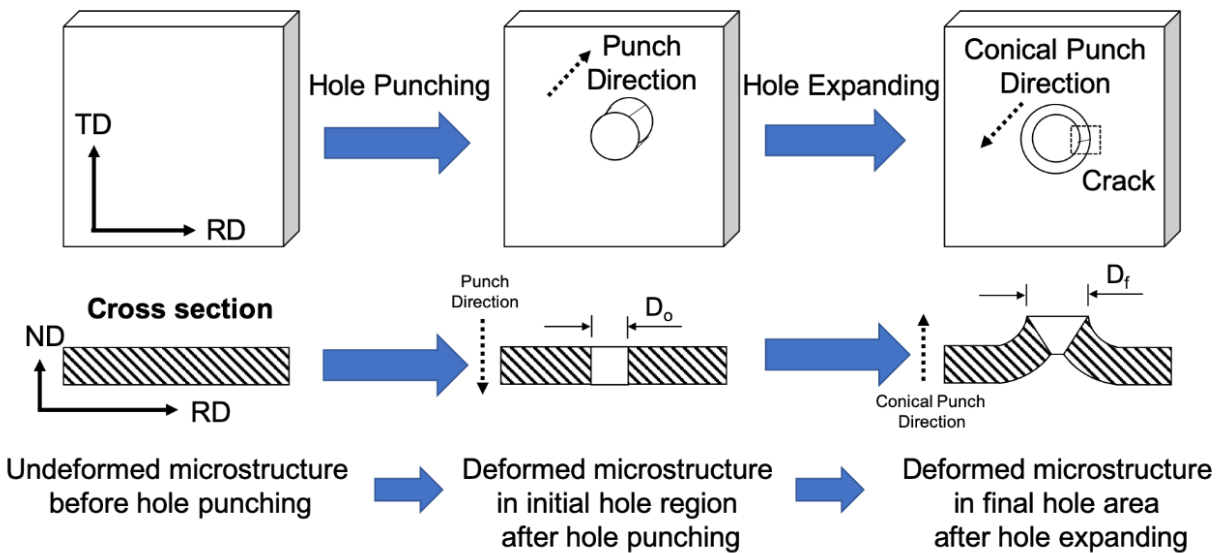
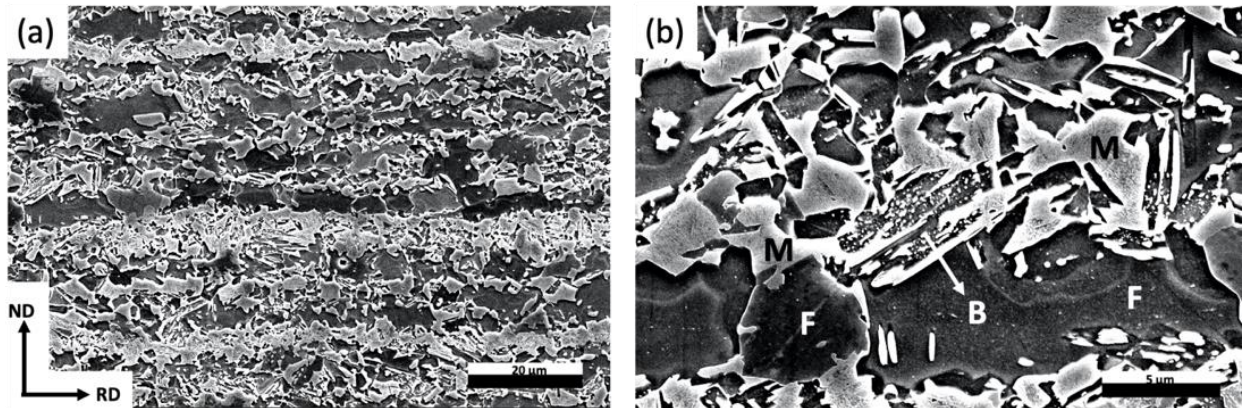
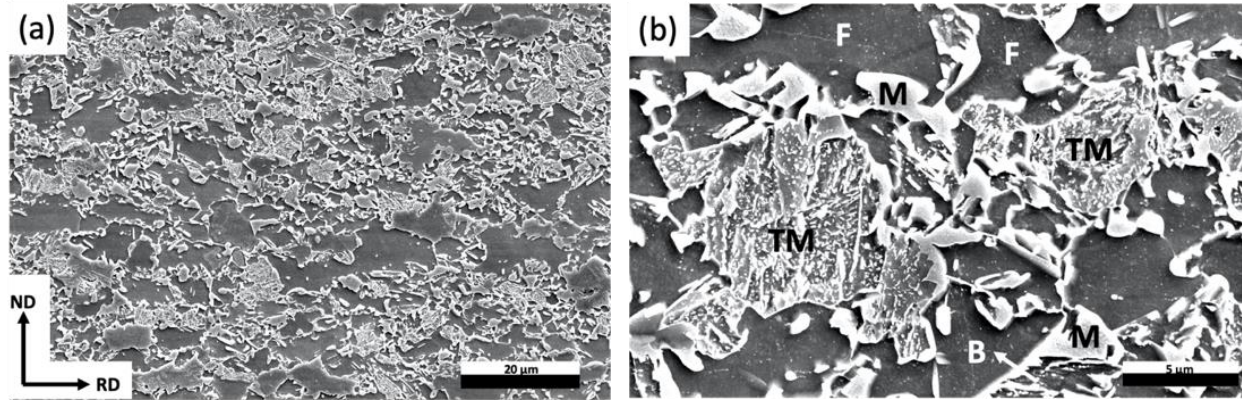


Figure 9.2 Schematic illustration of hole expansion process consisting of hole punching and hole expanding as well as the microstructure evolutions during the whole HET process.

Figs. 9.3 and 9.4 show the undeformed microstructures of steel condition LLL (0.04Al-0.06V-CT580°C) after GI and SC CGL simulations, conducted on a Gleeble 3800 machine. The GI annealed specimen is predominately composed of recrystallized ferrite, bainite and fresh martensite. From Table 8.1, the volume percentages of hard constituents bainite and fresh martensite are 29.5% and 48.8%, respectively. Also, the SC annealed specimen contains approximately 30.3% ferrite, 7.5% bainite, 19.0% fresh martensite and 43.2% tempered martensite, as seen in Table 8.2. As mentioned several times earlier, the change in the annealing paths from GI to SC results in the microstructural replacement of a large amount of fresh martensite by tempered martensite, as seen in Fig. 9.4.



**Figure 9.3** The undeformed microstructures of steel condition LLL (0.04Al-0.06V-CT580°C) GI, consisting of ferrite (labeled by F), bainite (B) and fresh martensite (M), with (a) low magnification and (b) high magnification.



**Figure 9.4** The undeformed microstructures of steel condition LLL (0.04Al-0.06V-CT580°C) SC, containing ferrite (labeled by F), bainite (B), fresh martensite (M) and tempered martensite (TM), with (a) low magnification and (b) high magnification.

Figs. 9.5 and 9.6 display the initial as-punched inner hole surface of the fully annealed HER blanks, after hole punching, of steel condition LLL (0.04Al-0.06V-CT580°C) with GI and SC anneals, respectively. As shown in Figs. 9.5 (b) and 9.6 (b), the initial hole surface, after hole punching, contains four zones: rollover zone, burnished zone, fracture zone and shear burr. Many defects are introduced in the initial hole surfaces in the process of hole punching. A few microvoids are found in the burnished zone (Figs. 9.5 (c) and 9.6 (c)), and numerous microvoids and shearing dimples are observed in the fracture zone (Figs. 9.5 (d), (e) and 9.6 (d), (e)). These results are in accord with the previous observations [125]. These punching-induced defects act as the crack initiation sites [39,125,128,131–133] and later severely affect HER results during hole expansion. Thus, in order to improve the hole expansion performances of AHSSs, some other hole formation methods (i.e., laser cutting, water jet cutting, drilling [134–136] and EDM [33]) or post-punching approaches [115,136] should be considered.

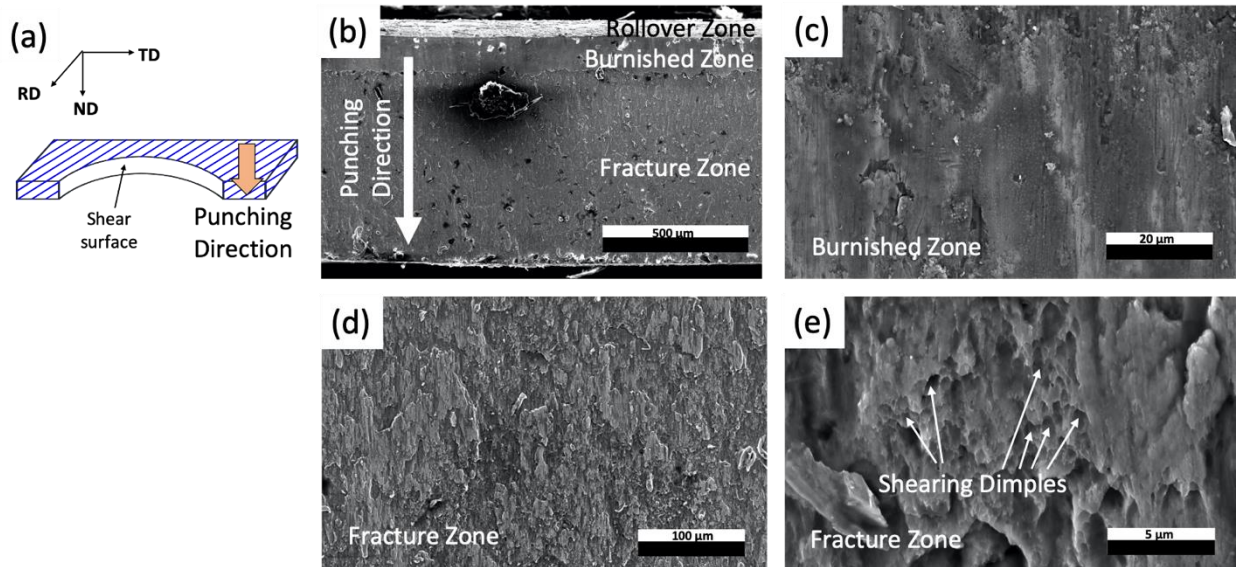


Figure 9.5 (a) The observation direction of (b) the initial hole surface of steel condition LLL (0.04Al-0.06V-CT580°C) GI, in the wake of hole punching, with cracks and shearing dimples found in (c) burnished zone and (d), (e) fracture zone.

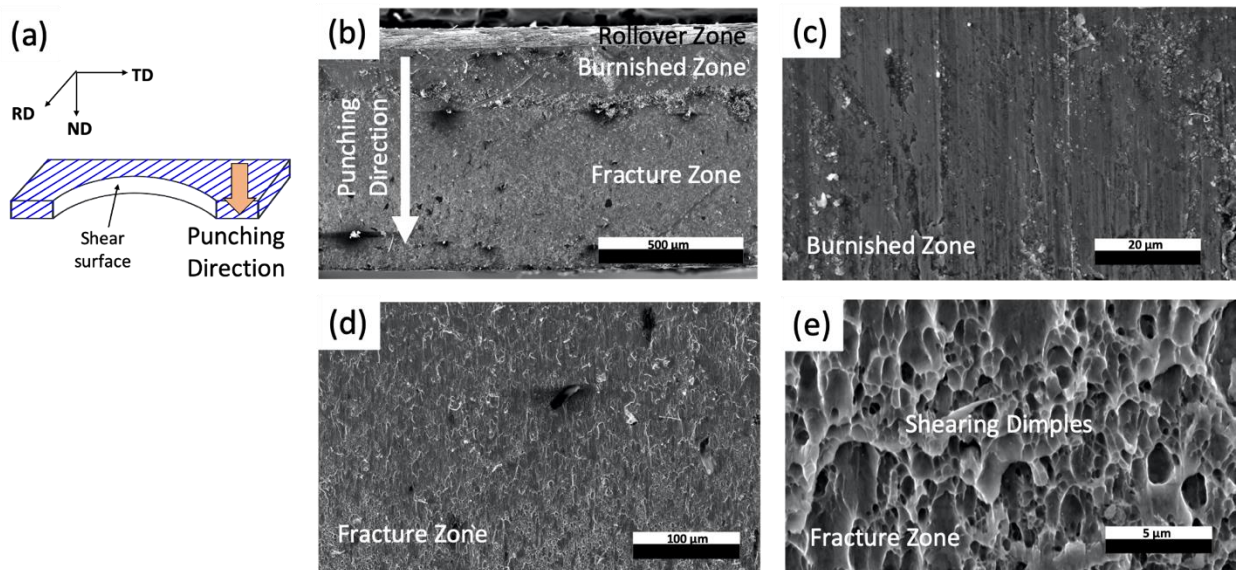
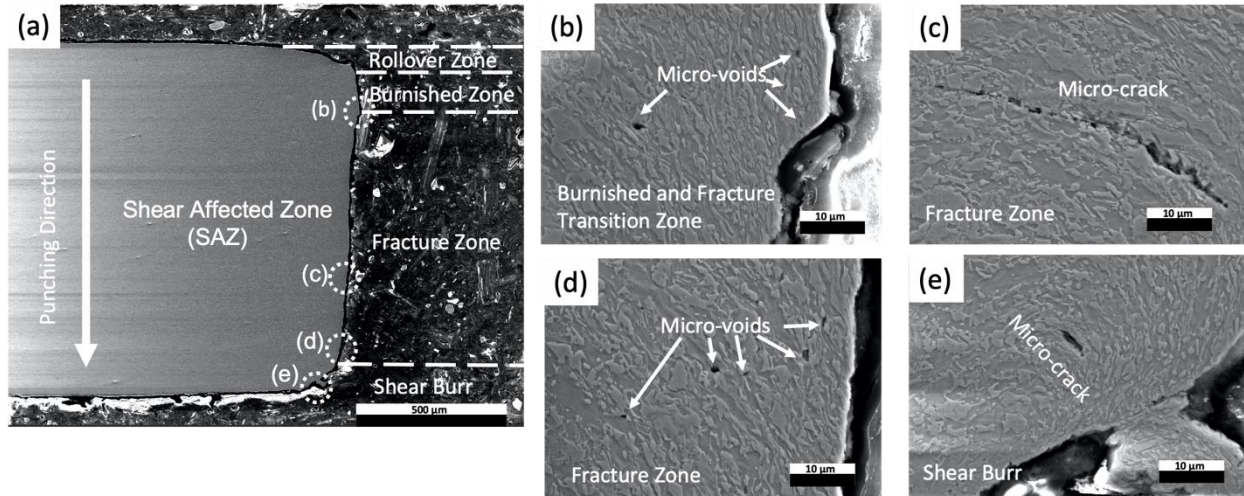
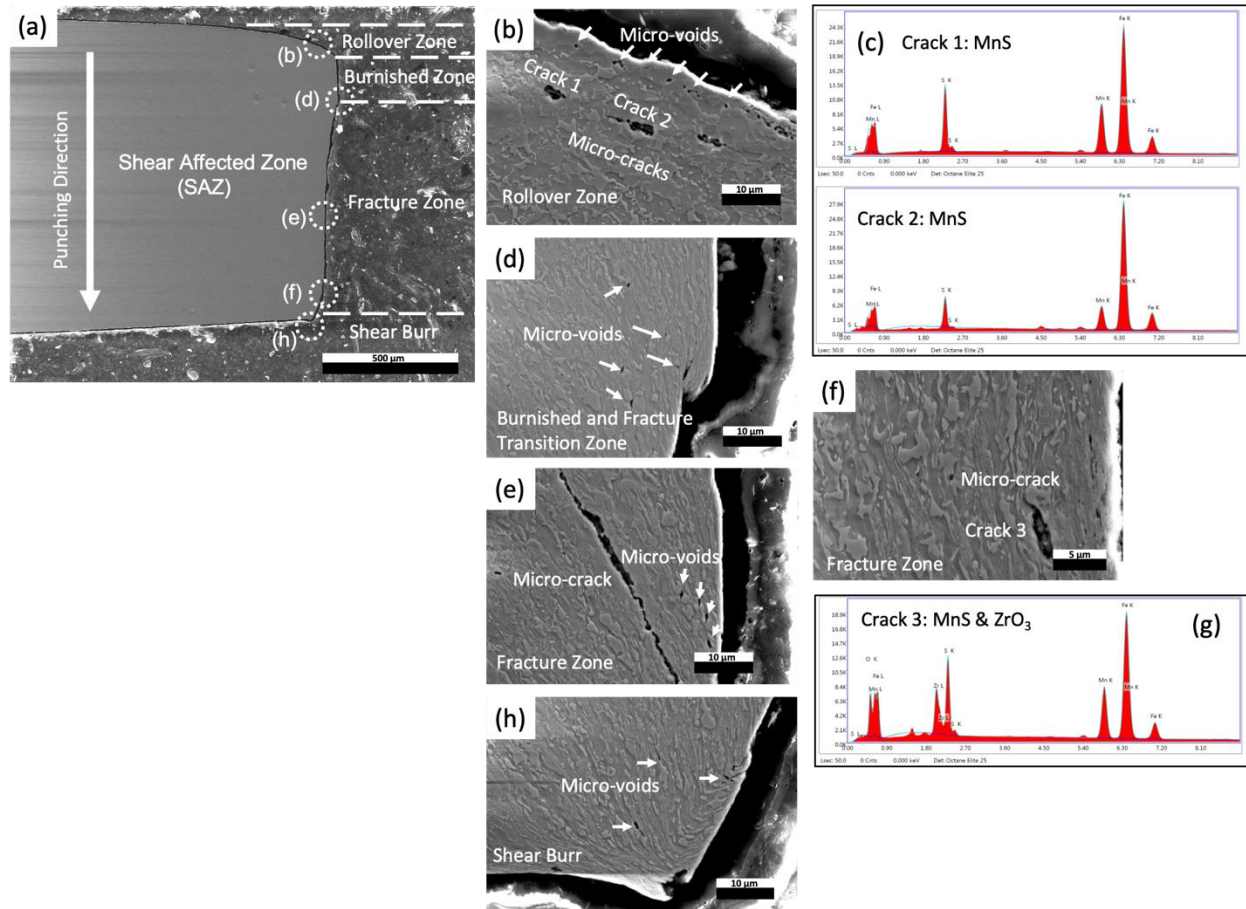


Figure 9.6 (a) The observation direction of (b) the initial hole surface of steel condition LLL (0.04Al-0.06V-CT580°C) SC, in the wake of hole punching, with cracks and shearing dimples found in (c) burnished zone and (d), (e) fracture zone.

The sheared edges and shear affected zones (SAZs) of the steel condition LLL (0.04Al-0.06V-CT580°C) GI and LLL SC, in the wake of hole punching, are presented in Figs. 9.7 and 9.8, respectively. The microstructures close to the sheared edges show that both ferrite and hard constituents are plastically deformed and elongated along the punching direction. In addition, the micro-voids or micro-cracks are observed in the area near the rollover zone (Figs. 9.8 (b)), the burnished and the fracture transition zone (Figs. 9.7 (b) and 9.8 (d)), fracture zone (Figs. 9.7 (c), (d) and 9.8 (e), (f)) and shear burr (Figs. 9.7 (e) and 9.8 (h)). Figs. 9.7 (b)–(d) and 9.8 (d), (h) show that the micro-voids nucleate by the decohesion of ferrite and hard constituents (fresh martensite for GI anneals and tempered martensite for SC anneals). Figs. 9.7 (e) and 9.8 (e) display that the micro-void nucleation is due to martensite cracking [39,125,131]. The micro-cracks (Figs. 9.8 (b) and (f)) existing near the sheared edge of steel condition LLL SC, are associated with MnS inclusions, as confirmed by energy dispersive spectroscopy (EDX) analyses in Figs. 9.8 (c) and (g), which is in agreement with Okano's observations [132]. Finally, a few micro-voids are observed at the ferrite/ferrite grain boundaries and very close to the sheared edges (Figs. 9.8 (b)), similar to the void nucleation mechanism reported in Pathak's work [39].



**Figure 9.7 (a) The sheared edge and shear affected zone (SAZ) of steel condition LLL (0.04Al-0.06V-CT580°C) GI, after hole punching, with micro-voids or micro-cracks found in (b) burnished and fracture transition zone, (c), (d) fracture zone, and (e) shear burr.**



**Figure 9.8** (a) The sheared edge and shear affected zone (SAZ) of steel condition LLL (0.04Al-0.06V-CT580°C) SC, after hole punching, with micro-voids or micro-cracks found in (b) rollover zone, (d) burnished and fracture transition zone, (e), (f) fracture zone and (h) shear burr as well as (c), (g) the EDX analyses of cracks in (b) and (f), respectively.

Figs. 9.9 (a) and (c) show the final holes, after the completion of the HETs, of steel condition LLL (0.04Al-0.06V-CT580°C) with GI and SC anneals, respectively. Closer observations, as shown in Figs. 9.9 (b) and (d), of the through-thickness cracks in the final hole surfaces are presented in Figs. 9.9 (a) and (b). It is apparent that the final hole diameter of steel condition LLL, SC is larger than that of LLL, GI, which indicates that the specimen of LLL SC has a better stretch-flangeability.

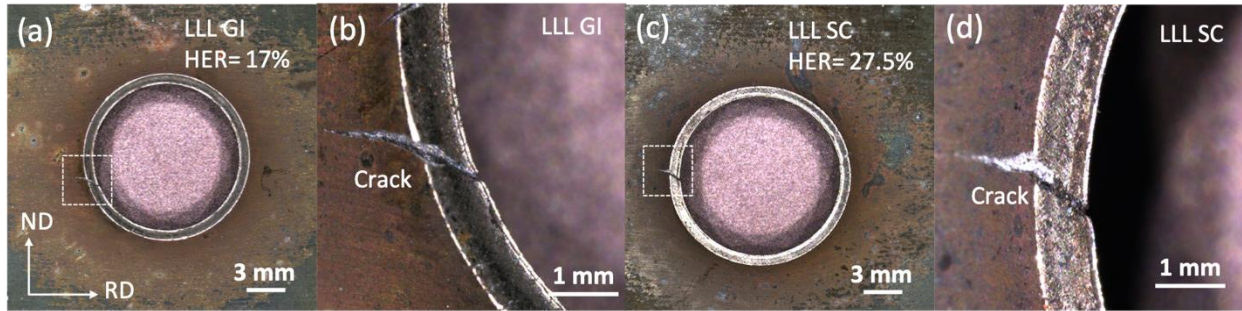


**Figure 9.9** The OM micrographs of final holes of steel conditions of (a) LLL (0.04Al-0.06V-CT580°C) GI and (c) LLL SC as well as (b), (d) the closer observations of through-thickness cracks in (a) and (c), respectively.

Figs. 9.10 and 9.11 show the sheared edges and shear affected zones (SAZs) of steel conditions LLL (0.04Al-0.06V-CT580°C) GI and LLL SC after the HETs. Both soft ferrite and hard constituents were further deformed and elongated along the conical punch displacement direction (Figs. 9.10 (b)-(d) and 9.11 (b)-(d)). The micro-voids shown in Figs. 9.11 (b) and (c) represent the early stage of ductile fracture initiation. These voids appear to be nucleated at ferrite/hard interfaces or were related to martensite cracking. Figs 9.11 (d) and (e) present the crack propagation from the final punched hole sheared edge to the sheared affected zone (SAZ). Martensite bands (for GI anneals) or tempered martensite bands (for SC anneals) result in cracks and the cracks propagate at ferrite/hard constituent interfaces along the shear flow curves. Also, the existence of the zig-zag fracture path (Figs 9.6 (d), (e)) is the apparent evidence of ductile fracture, since the zig-zag crack path was formed due to the major crack propagation in the region with a high void density [195].

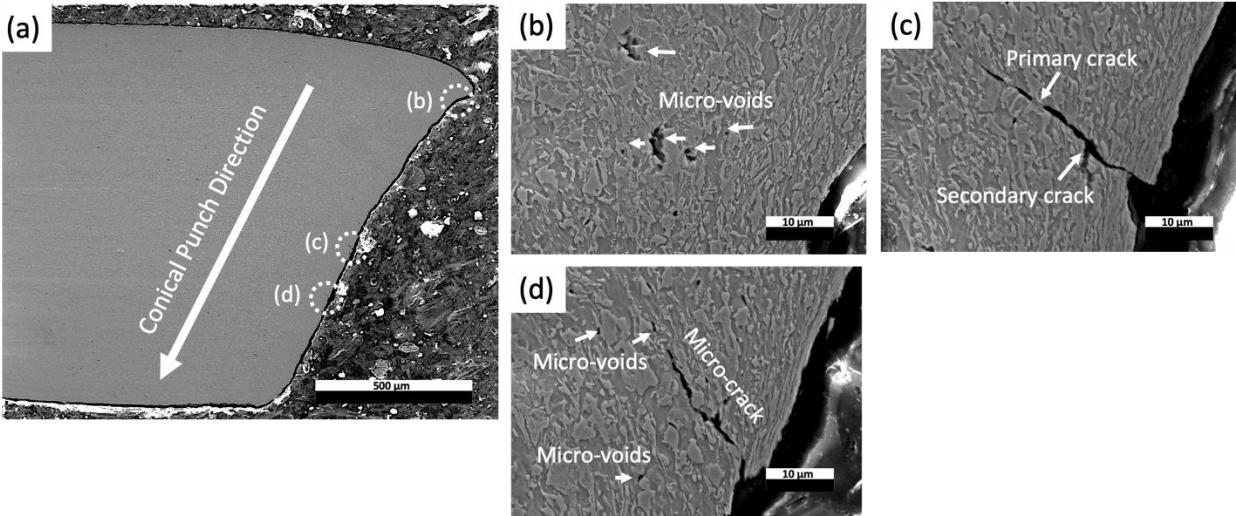


**Figure 9.10 (a) The sheared edge and shear affected zone (SAZ) of steel condition LLL (0.04Al-0.06V-CT580°C) GI, in the wake of hole expansion, with voids or cracks found in (b), (c) and (d) different areas of the sheared edge.**

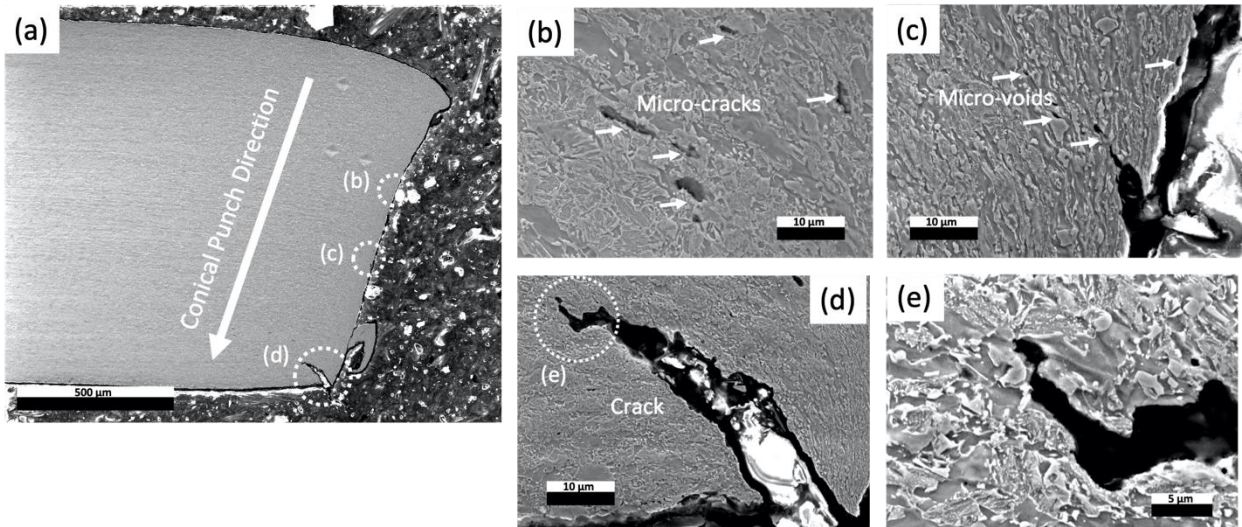


**Figure 9.11 (a) The sheared edge and shear affected zone (SAZ) of steel condition LLL (0.04Al-0.06V-CT580°C) SC, in the wake of hole expansion, with voids or cracks found in (b), (c) and (d) different areas of the sheared edge as well as (e) the closer observation of a crack in (d).**

### 9.1.3 The Determination of Punching-Induced Pre-Strains

EBSD-KAM technology is used for quantifying local misorientations within grains, which are related to  $\rho_{\text{GND}}$  [112] and plastic strain gradients [111]. So, the application of EBSD-KAM in this chapter was aimed to determine the hole-punching-induced pre-strains in the initial hole shear-edges and shear affected zones (SAZs) of HER samples for the steel condition of LLL (0.04Al-0.06V-CT580°C) with both GI and SC anneals.

As mentioned in Section 5.5.3, the local misorientations of the areas in the distance of 0–600  $\mu\text{m}$  from two critical positions were quantified. Table 9.2 list the KAM values varying with the distances from the initial hole sheared edges, in terms of different tested positions and steel conditions. Also, the  $\varepsilon_{\text{eq}}$  values were determined from KAM results, by using Eq. 5.16. So, the relationships between KAM (or  $\varepsilon_{\text{eq}}$ ) and the distance from the initial hole sheared edges are plotted in Fig. 9.12. The results of KAM and calculated  $\varepsilon_{\text{eq}}$  decrease as the distance from the initial hole sheared edges increases, and they converge with the distance exceeding 400  $\mu\text{m}$ . In addition, the distributions and values of KAM and calculated  $\varepsilon_{\text{eq}}$  vary with the tested positions from the sheared edges and the selected steel conditions. At distances of less than 150  $\mu\text{m}$ , the results of KAM or calculated  $\varepsilon_{\text{eq}}$  of the areas from the burnished and fracture transition zone (Position A) are larger than those of the areas from the middle of the fracture zone (Position B), which indicates that the maximum plastic strain is located at the burnished and fracture zone. This finding was also reported in Levy's work [129]. Additionally, the maximum calculated  $\varepsilon_{\text{eq}}$  values of two steel conditions, LLL GI and LLL SC, are 2.92 and 1.48, respectively. This shows that much internal plastic strain was introduced by hole punching for GI annealed DP steels, and later severely influenced the hole expansion performances of the fully annealed DP steels with the GI anneal.

**Table 9.2 The relationships between KAM values and the distances from the sheared edges in different positions of steel conditions of LLL (0.04Al-0.06V-CT580°C) GI and LLL SC.**

IDs	Positions	KAM (°)										
		The distance from the sheared edge (μm)										
		0	60	120	180	240	300	360	420	480	540	600
LLL, GI	Position (A)	2.69	2.11	2.02	1.68	1.49	1.35	1.22	0.94	0.90	0.79	0.79
LLL, GI	Position (B)	1.76	1.69	1.64	1.59	1.34	1.22	0.95	0.91	0.81	0.72	0.72
LLL, SC	Position (A)	2.00	1.92	1.82	1.61	1.43	1.13	0.97	0.87	0.86	0.80	0.77
LLL, SC	Position (B)	1.80	1.75	1.66	1.62	1.46	1.32	1.08	0.94	0.77	0.75	0.65

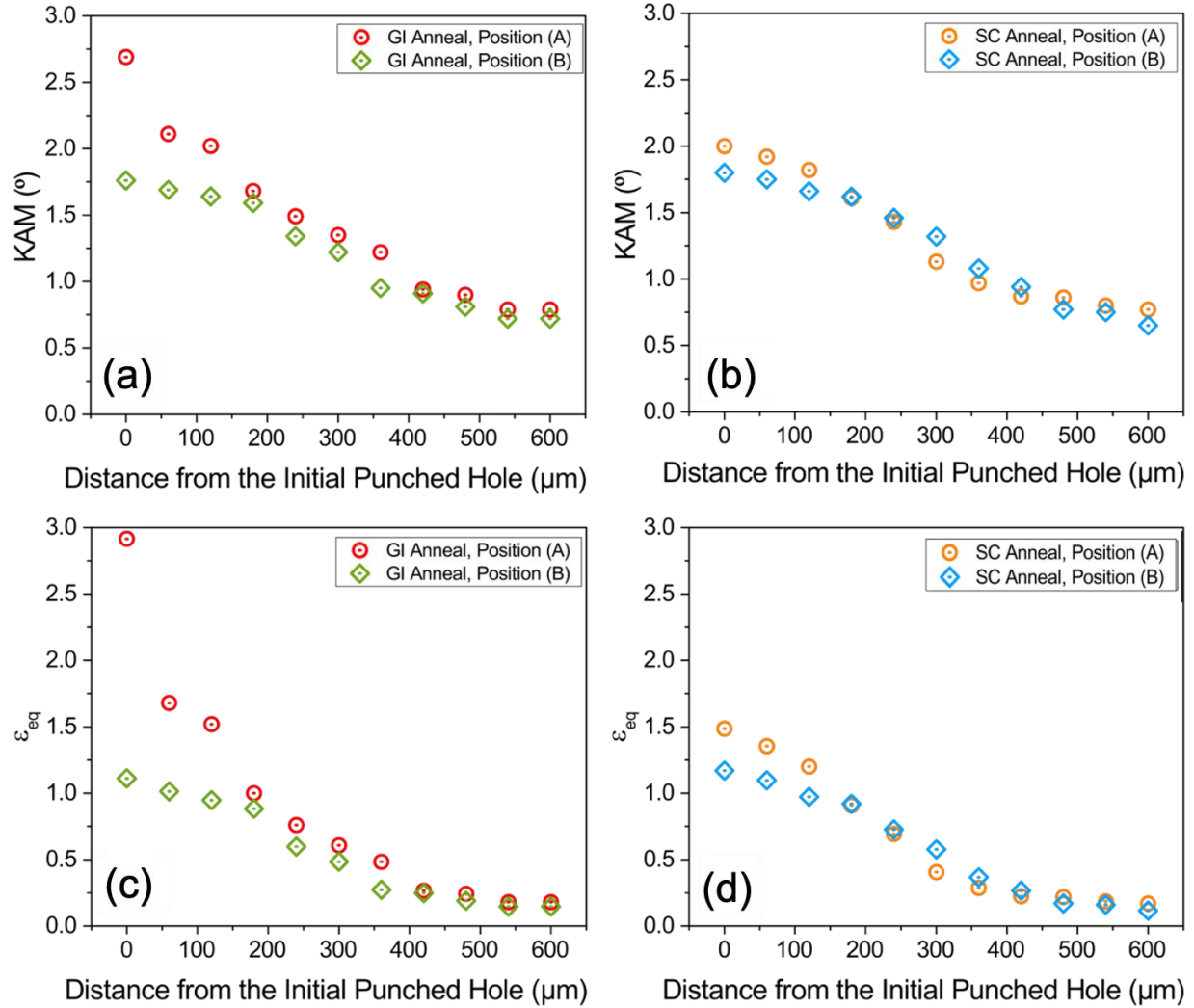


**Figure 9.12** The relationships between KAM and the distance from the sheared edge of steel conditions of (a) LLL (0.04Al-0.06V-CT580°C) GI and (b) LLL SC, and the relations of the calculated  $\epsilon_{eq}$  and the distance from the sheared edge of steel conditions of (c) LLL (0.04Al-0.06V-CT580°C) GI and (b) LLL SC.

Nanoindentation technology is another method used for determining the hole-punching-induced pre-strains, since both ferrite and hard constituents in the sheared edges or shear affected zones (SAZs) are deformed in the wake of hole punching.

Figs. 9.13 and 9.14 show the SEM micrographs of the nanoindents within the microstructures of steel conditions LLL (0.04Al-0.06V-CT580°C) GI and LLL SC, respectively.

The tested Positions A, B and D are in the areas near the initial hole sheared edges, while Position C is about 300  $\mu\text{m}$  away from Position B. Both ferrite and hard constituents (i.e., bainite, fresh martensite or tempered martensite) near the sheared edges are deformed and elongated by shear along the RD, with high aspect ratios (Figs. 9.13 (b), (c), (e) and 9.14 (b), (c), (e)). The grains in these areas are compacted so tightly that the conventional Vickers hardness test, even with a load of 1 gf, cannot differentiate the difference in hardness between ferrite and fresh martensite or tempered martensite. Therefore, the application of nanoindentation, with the lower load (i.e., 2000  $\mu\text{N}$ ) and the smaller indents, make it possible to quantify the changes in hardness values, caused by hole punching, of ferrite and hard constituents. For each tested position, 25 nanoindents were performed and characterized by SEM. The indents inside ferrite grains are signified by red circles, the indents inside fresh martensite islands by blue circles, the indents inside tempered martensite by green circles and the indents within other regions (i.e., ferrite/ferrite grain boundaries or ferrite/hard constituent interfaces) by white circles.

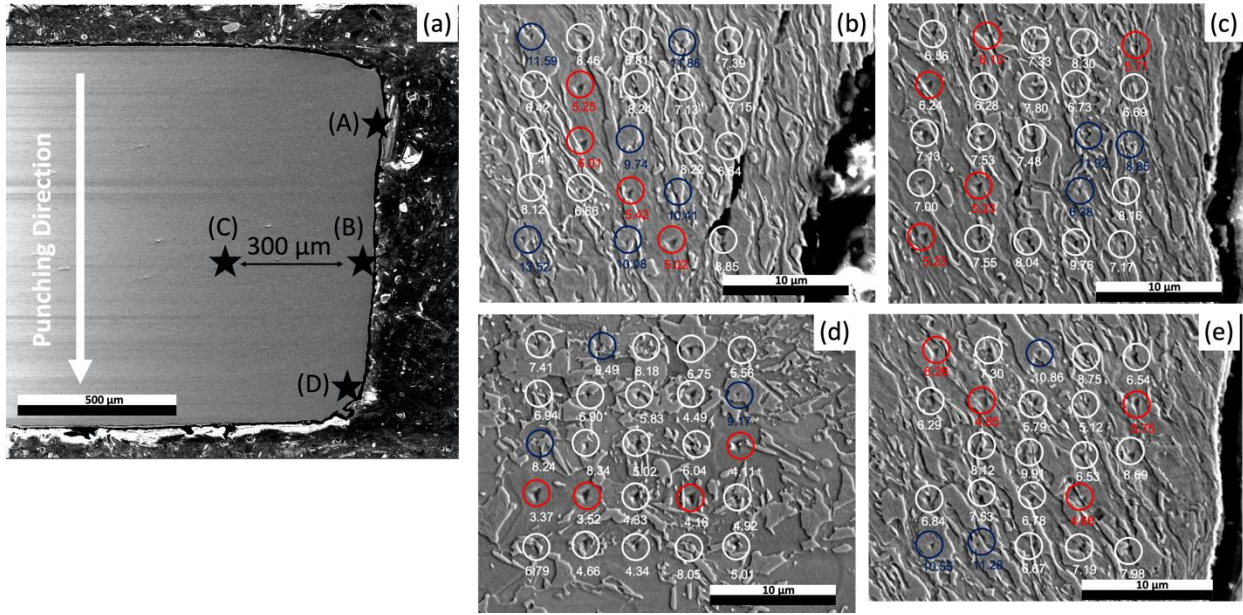


Figure 9.13 (a) The initial hole sheared edge and shear affected zone (SAZ) of steel condition LLL (0.04Al-0.06V-CT580°C) GI, after hole punching, with nanoindents in Positions (b) A, (c) B, (d) C and (e) D.

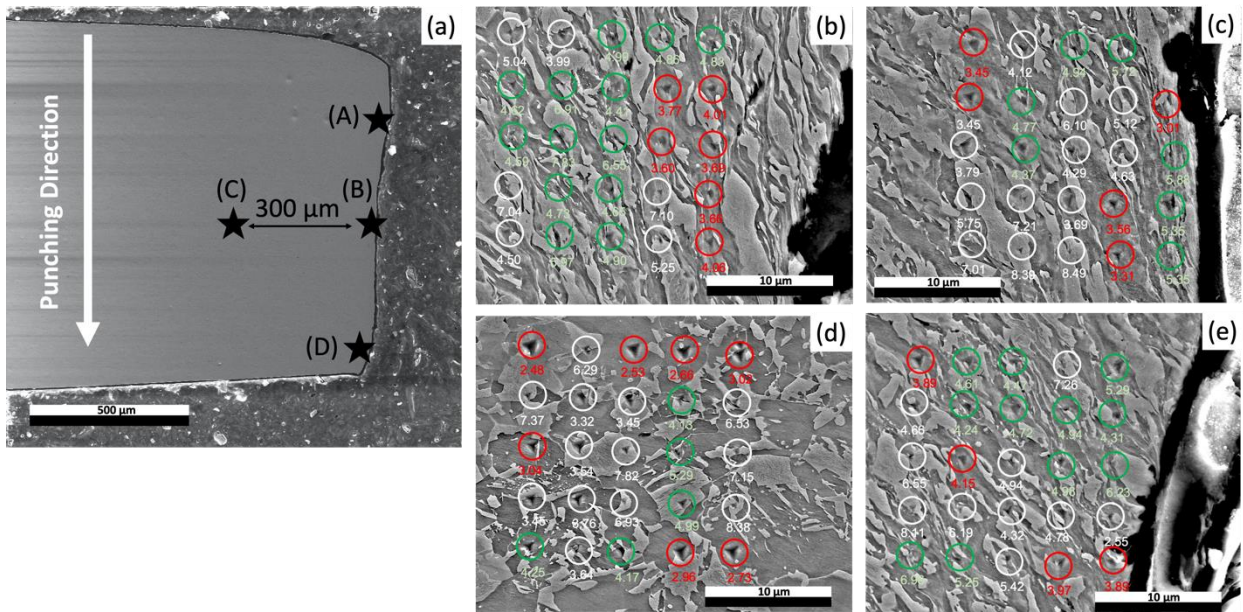


Figure 9.14 (a) The initial hole sheared edge and shear affected zone (SAZ) of steel condition LLL (0.04Al-0.06V-CT580°C) SC, after hole punching, with nanoindents in Positions (b) A, (c) B, (d) C and (e) D.

Table 9.3 lists the measured nanohardness results of ferrite and fresh martensite or tempered martensite in four tested positions of the fully annealed steel condition of LLL with both GI and SC anneals. The nanohardness values of undeformed ferrite in LLL GI and LLL SC are 3.1 GPa and 2.6 GPa, respectively. For hard constituents, the nanohardness results of undeformed fresh martensite in LLL GI and undeformed tempered martensite in LLL SC are 8.0 GPa and 4.1 GPa, respectively. In Positions A, B and D, the nanohardness values of ferrite near the sheared edges in the steel condition of LLL GI increase from 3.1 GPa to 5.7 GPa (~84% increase). Meanwhile, the fresh martensite in Position A was work hardened and obtained the nanohardness of 11.2 GPa (~40% increase) from 8.0 GPa. In terms of the SC annealed steel condition, the deformed ferrite in Position A can reach the maximum nanohardness of 3.8 GPa (~46% increase). And the nanohardness results of tempered martensite were increased by 12%–32%, reaching the maximum value of 5.4 GPa in Position A. However, nanohardness results of ferrite and hard constituents in Position A, 300  $\mu\text{m}$  away from the sheared edges, are not affected remarkably. These results indicate that the hole-punching-induced pre-strains or dislocation densities vary with the distance from the sheared edges and that microstructures of GI annealed DP steels are more strengthened than those of SC annealed DP steels.

**Table 9.3 Measured nanohardness values of four tested positions**

IDs	Phases	Nanohardness (GPa)				
		Undeformed	Position A	Position B	Position C	Position D
LLL, GI	Ferrite	3.1±0.5	5.4±0.4	5.7±0.5	3.8±0.4	5.4±0.7
	Fresh Martensite	8.0±0.6	11.2±1.4	9.7±1.9	8.9±0.6	10.9±0.3
LLL, SC	Ferrite	2.6±0.4	3.8±0.2	3.4±0.2	2.8±0.2	3.9±0.1
	Tempered Martensite	4.1±0.5	5.4±1.1	5.1±0.5	4.6±0.5	5.0±0.8

#### **9.1.4 Observation of the Deformed Microstructures near the Final Hole Sheared Edges after Incomplete Hole Expansion Tests**

In order to investigate the micro-fracture mechanism, in terms of hole expansion behaviors, for ultra-high strength, vanadium bearing DP steels, incomplete or partial HETs were conducted for the fully annealed DP sample MHL (0.4Al-0.12V-CT580°C), SC with the tests interrupted at 0%, 5%, 10%, 15% and 25% of the final tested value. The final hole internal surfaces of the tested HER blanks were sectioned, cut, ultrasonically cleaned and observed via SEM. Prior to hole expanding (HER=0%), micro-voids and shear dimples caused by hole punching can be observed in the fracture zone (Fig. 9.15 (a)). After the 5%-hole expansion testing, micro-cracks or enlarged micro-voids can be detected in the fracture zone (Fig. 9.15 (b)). Fig. 9.15 (c) shows the SEM micrograph of one micro-crack in Fig. 9.15 (b) with a high magnification, illustrating the void enlargement of the pre-existing voids introduced by hole punching. Also, the shearing dimples can be observed inside the enlarged void, which is conspicuous evidence of ductile fracture. With further deformation (HER=10%), the micro-cracks continue propagating in a zigzagging fracture path, coexisting with continuous void nucleation, Figs. 9.15 (d) and (e). Regarding the final hole surface of the selected fully annealed DP sample with the HER of 15%, the crack continues propagating from the fracture zone towards the burnished and rollover zones with plasticity, Figs. 9.15 (f) and (g). As the major crack propagates and extends through the whole thickness direction of the tested HER blank, the HET is stopped. In this condition, the major crack crossing the section of the tested sample along with minor cracks (or enlarged voids) (Fig. 9.15 (j)) and newly nucleated voids (Fig. 9.15 (i)) can be observed via SEM. Getting a closer look inside the cracks, long cracks crossing the shearing dimples still can be detected in Figs. 9.15 (h) and (k).

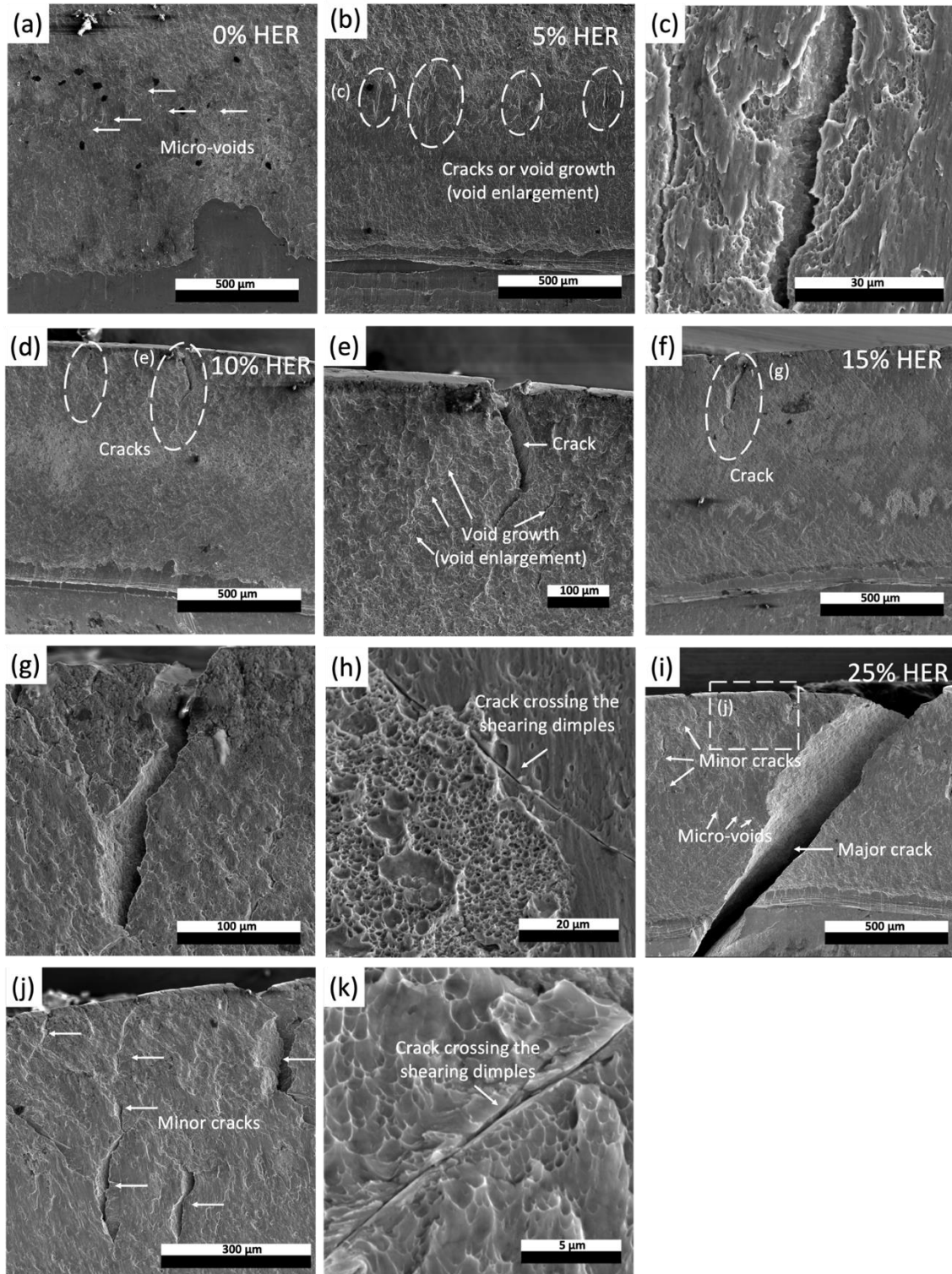


**Figure 9.15** The final hole surfaces of steel condition MHL (0.4Al-0.12V-CT580°C) SC with the HER values of (a) 0%, (b) (c) 5%, (d) (e) 10%, (f) (g) (h) 15% and (i) (j) (k) 25%.

## 9.2 Discussion

### 9.2.1 Effect of Coiling Temperature on HER

From Fig. 6.1, the OM micrographs of DP hot band coils with two coiling temperatures are characterized by a ferrite-pearlite mixture. However, the microstructures of the hot rolled steels coiled at 580°C predominantly consist of acicular ferrite and refined polygonal ferrite with high dislocation densities or sub-grain structures, while the hot band coils with a CT of 677°C, which mainly comprise coarse polygonal ferrite with low dislocation densities or sub-grain structures [159]. After 60% cold rolling and intercritical annealing, the SEM micrographs of the fully annealed DP steels with two coiling temperatures, as seen in Figs. 8.1–8.5, show that lowering coiling temperatures results in ferrite grain refinement, since cold rolled fined-grained microstructures provide higher ferrite grain shape  $S_v$  for grain boundary nucleation at the early stage of ferrite recrystallization [98] during intercritical annealing.

Figs. 9.16 shows the relationships between HER results and ferrite grain sizes, varying with coiling temperatures, for steel conditions of LLL (0.04Al-0.06V-CT580°C) and LLH (0.04Al-0.06V-CT677°C) with both GI and SC anneals. For both GI and SC annealed DP specimens, reducing the coiling temperatures leads to a decrease in average ferrite grain sizes. Meanwhile, hole expansion performances change with ferrite grain sizes, which is in agreement with the studies of Yoon et al. [196] and Gwon et al. [126]. From previous works, fracture toughness was a critical factor dominating HER values of AHSSs [125][197] and grain refinement is the only approach of improving strength and fracture toughness simultaneously. The fine-grained microstructures can provide more resistance to crack propagation [126,196]. Void nucleation and growth located at recrystallized ferrite/ferrite grain boundaries changes with ferrite grain sizes [126], showing that

fine-grained microstructures can provide more resistance to crack propagation. Thus, the hole expansion performances of DP steels can benefit from fine or ultra-fine ferritic microstructures.

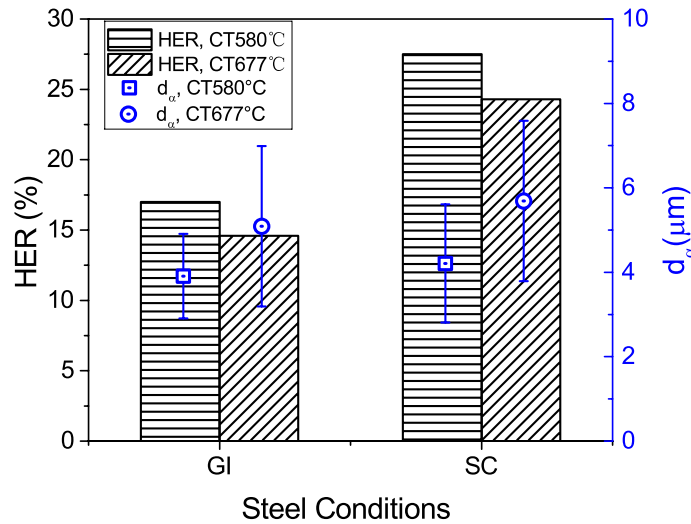


**Figure 9.16** The relationships between HER results and ferrite grain sizes ( $d_{\alpha}$ ) of steel conditions of LLL (0.04Al-0.06V-CT580°C) and LLH (0.04Al-0.06V-CT677°C) with both GI and SC anneals

### 9.2.2 Effect of CGL Simulations on HER

Standard galvanizing (GI) and supercooling (SC) process CGL simulations were conducted with a Gleeble 3800 machine, in order to investigate the effects annealing paths on microstructures, mechanical properties as well as stretch-flangeability of candidate DP steels in this dissertation.

As shown in Fig. 8.8, the change in heat treatments from GI to SC anneals results in the microstructural replacement of a large amount of fresh martensite by tempered martensite. Hasegawa et al. [128] theoretically pointed out that the hole expansion performance of DP 980 may be controlled by the hardness difference between ferrite and fresh martensite, and the hardness values were calculated by experimental equations. Later, Taylor et al. [33] used nanoindentation

technology to verify Hasegawa's assumption. So, the HER values of DP steels can be raised through the reduction in the hardness difference between ferrite and hard constituents [27,28,33]. Taking the steel condition LLL (0.04Al-0.06V-CT580°C) as an example, the change in the nanohardness difference between ferrite and hard constituents from 4.9 GPa (for GI anneals) to 1.5 GPa (for SC anneals), as seen in Table 9.3, gives a rise to the improvement of HER values from 17.0% (for GI anneals) to 27.5% (for SC anneals), as seen in Table 9.1.

The punching-induced pre-strains are another factor that causes the differences in hole expansion performances of the fully annealed DP steels with GI and SC anneals. The  $\epsilon_{eq}$  results calculated from KAM values (Fig. 9.12) and nanohardness measurements of work hardened ferrite and hard constituents (Figs. 9.13 and 9.14) indicate that different levels of internal plastic strains were introduced in the microstructures in the sheared edges and even shear affected zones (SAZs) for GI and SC annealed specimens. For instance, after hole punching, the  $\epsilon_{eq}$  of 2.92 is introduced at the burnished and fracture transition zone of the HER blanks for steel condition of LLL GI, which causes the nanohardness values of ferrite and fresh martensite to increase from 3.1 GPa to 5.4 (~74% increase) GPa and from 8.0 GPa to 11.2 GPa (~52% increase), respectively. While, concerning the HER specimens of LLL SC, the nanohardness results of the deformed ferrite and tempered martensite are increased by 46% and 32%, respectively, when the maximum  $\epsilon_{eq}$  of 1.48 is achieved by hole punching. So, the lower punching-induced pre-strains for SC annealed microstructures will obtain better shear-ductility in the wake of hole expansion.

### **9.2.3 The Relationship between HER and the Characteristics of Initial Hole Internal Surface**

The SEM micrographs of the initial hole surfaces of the steel conditions LLL, GI and LLL, SC are shown in Fig. 9.17. The area percentages of burnished zone and fracture zone of LLL, GI

are about 15.3% and 78.2%, respectively and the HER value of LLL, GI is 17.0%. On the other hand, in terms of the SC annealed specimen for steel condition of LLL, the area fractions of burnished zone and fracture zone are 21.8% and 70.2%, respectively, with a higher HER value of 27.5%.

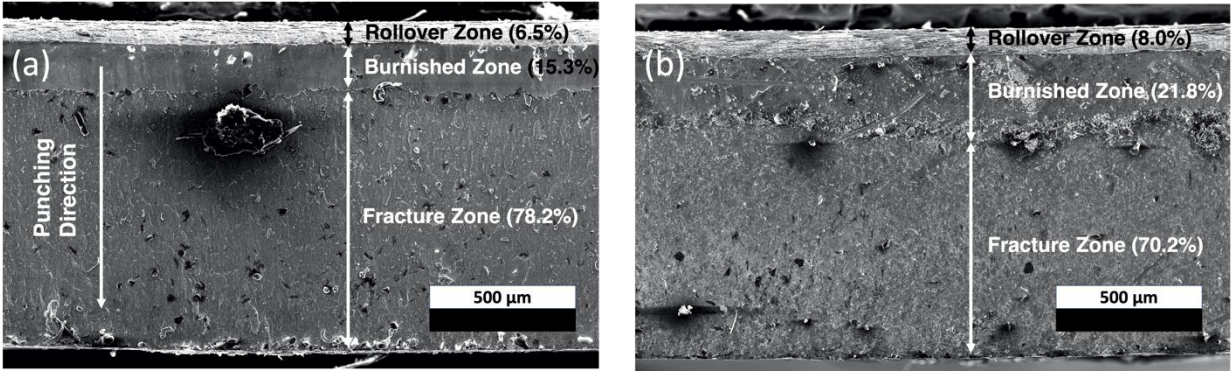


**Figure 9.17** The initial hole surfaces of steel conditions of (a) LLL GI and (b) LLL SC

Table 9.4 lists the area fractions of different zones (i.e., rollover zone ( $f_{V(R)}$ ), burnished zone ( $f_{V(B)}$ ) and fracture zone ( $f_{V(Fx)}$ )) of the initial hole surfaces of the candidate DP steels. Fig. 9.18 plots the relationship between HER and the characteristics of initial hole surface, based on the data in Table 9.4. From Fig. 9.18, HER increases with increasing  $f_{V(B)}$  and the increase in  $f_{V(Fx)}$  leads to the reduction in HER. However, the hole expansion performance is not relevant to  $f_{V(R)}$ . These results indicate  $f_{V(B)}$  or  $f_{V(Fx)}$  can be used to evaluate HER results. So, a parameter called burnished to fracture ratio ( $f_{V(B)}/f_{V(Fx)}$ ), which is used for assessing sheared edge quality by press shop [198], was applied to estimate stretch-flangeability. The correlation of  $f_{V(B)}/f_{V(Fx)}$  vs HER is also shown in Fig. 9.18, and this is given in Eq. 9.2, with a reasonable coefficient of determination ( $R^2$ ) of 0.75.

$$\text{HER} = 81.19 \times f_{v(B)}/f_{v(Fx)} + 0.15 \quad (9.2)$$

As mentioned in Chapter 2, the burnished zone (Figs. 9.5 (c) and 9.6 (c)), a straight and soft wall in the initial hole internal surface, is formed when the punch continues penetrating the tested metal after the formation of the rollover zone. The fracture zone (Figs. 9.5 (d) and 9.6 (d)) is formed by fracturing from the bottom of the burnished zone to the separation of the tested material. Both the burnished and fracture zones are controlled by UTS, since  $f_{v(B)}$  decreases and  $f_{v(Fx)}$  increases with increasing UTS [129,198–200]. From the literature [199],  $f_{v(B)}$  and  $f_{v(Fx)}$  are also influenced by cutting clearance. As cutting clearance increases, more tested material is deformed, resulting in the increase in shear affected zone (SAZ) and the reduction in burnished zone area required for initiating fracture [129]. In addition, In Chintamani et al.'s research [198],  $f_{v(Fx)}$  increases with increasing cutting clearance. So, according to Eq. 9.2, decreasing cutting clearance leads to the increase in  $f_{v(B)}/f_{v(Fx)}$ , hence improving hole expansion performance. This indicates that stretch-flangeability is not only influenced by chemical, heat treatments, microstructures and mechanical performances, but also by punching operation parameters (i.e., cutting clearance).

**Table 9.4 The area fractions of rollover ( $f_{V(R)}$ ), burnished ( $f_{V(B)}$ ) and fracture ( $f_{V(Fx)}$ ) zones in the initial hole surfaces of fully annealed DP steels.**

IDs	$f_{V(R)}$ (%)	$f_{V(B)}$ (%)	$f_{V(Fx)}$ (%)	IDs	$f_{V(R)}$ (%)	$f_{V(B)}$ (%)	$f_{V(Fx)}$ (%)
LLL, GI	6.5	15.3	78.2	LLL, SC	8.0	21.8	70.2
LLH, GI	5.9	14.4	79.7	LLH, SC	4.5	20.9	74.6
LHL, GI	8.5	16.8	74.7	LHL, SC	7.8	21.9	70.3
LHH, GI	5.1	15.8	79.1	LHH, SC	9.2	18.7	72.1
MLL, GI	5.8	14.3	79.9	MLL, SC	6.7	22.2	71.1
MLH, GI	7.3	12.7	80.0	MLH, SC	7.4	19.9	72.7
MHL, GI	8.3	16.2	75.5	MHL, SC	6.2	19.7	74.0
MHH, GI	8.4	15.0	76.6	MHH, SC	9.2	20.1	70.7

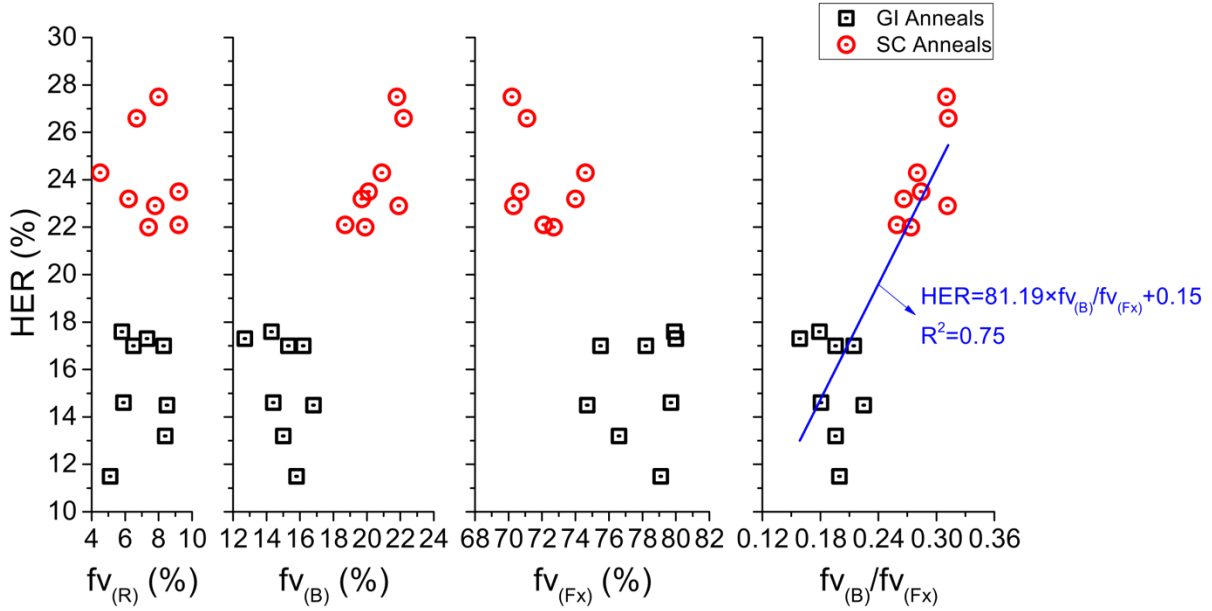


**Figure 9.18** The relationship between HER and the characteristics of initial hole surface

#### 9.2.4 Crack Initiation Caused by Hole Punching and Micro-Mechanism for Hole Expansion

The hole punching process generates two regions, initial punched hole internal surface (Figs. 9.5 and 9.6) and initial punched hole sheared edge (Figs. 9.7 and 9.8). Micro-voids and shearing dimples in the fracture zone of the initial punched hole surface are introduced by punching. Regarding the microstructures near the initial punched hole sheared edge, punching leads to micro-voids or cracks that nucleate at the ferrite/hard constituent (i.e., bainite, fresh martensite and tempered martensite) interfaces, ferrite/ferrite grain boundaries and associated with MnS inclusions. These defects caused by punching act as the crack initiation sites [39,125,128,131–133], Fig. 9.19 (a). Fig. 9.19 schematically introduces the micro-fracture mechanism of hole expansion for ultra-high strength and vanadium bearing DP steels. In the early stage of hole expansion, cracks start to propagate, or voids start to grow by void enlargement, coexisting with continuing void nucleation, as plastic strain increases, Fig. 9.19 (b). With further deformation,

cracks continue propagating from the fracture zone towards the burnished and rollover zones. Once the major crack crosses the thickness of the tested sample, the test is by definition completed, and at which point the HET is stopped, Fig. 9.19 (c).

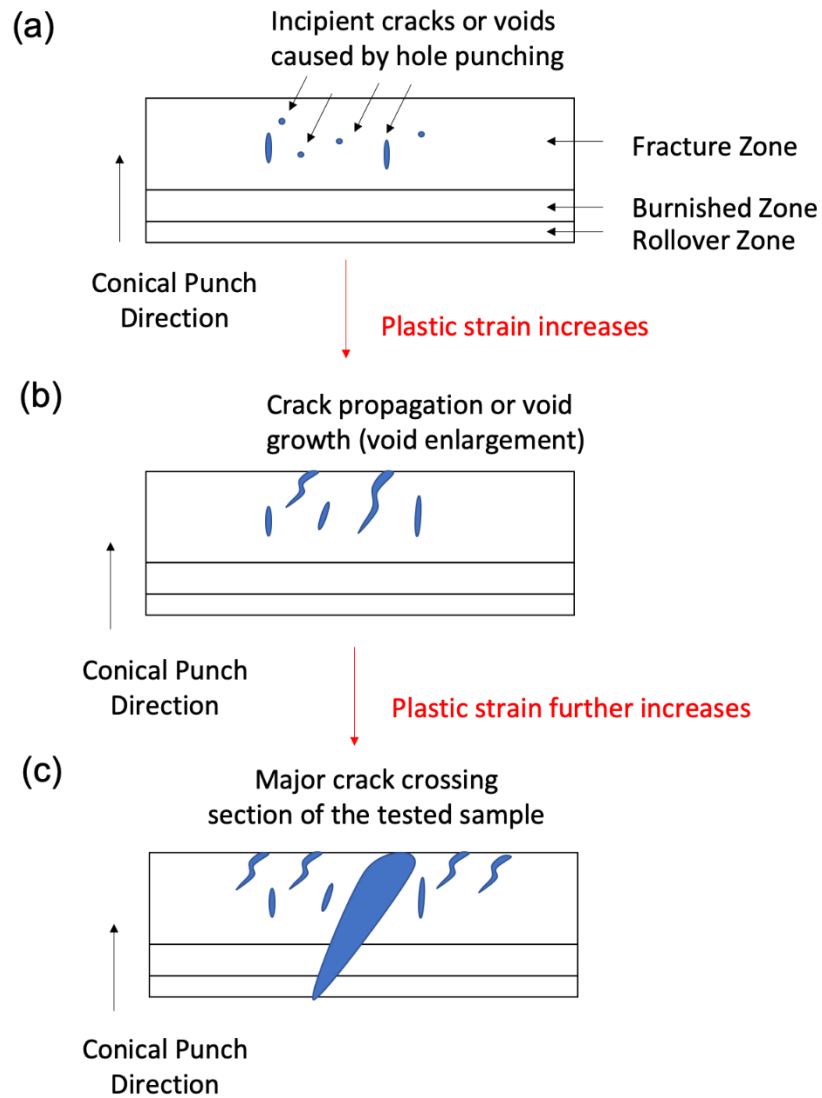


**Figure 9.19** The schematic illustration of the micro-fracture mechanism in terms of hole expansion for fully annealed DP steels. (a) Incipient cracks or voids caused by hole punching, (b) crack propagation or void growth by void enlargement and (c) the major crack crossing section of the tested sample.

### 9.3 Conclusions

This chapter had the purposes of better understanding the improvements found in the hole expansion performance of ultra-high strength DP steels, and to investigate the key factors controlling stretch-flangeability. The findings can be generalized as the following conclusions.

(1) The coiling temperatures and annealing paths play significant roles in dominating HER values. The low coiling temperature results in refined microstructures, which provide more capacity of resisting micro-void growth and covalence, thus improving stretch-flangeability. The changes in CGL simulations from GI anneals to SC anneals lead to the replacement of a large amount of fresh martensite with tempered martensite, reducing the nanohardness difference between ferrite and hard constituent and meanwhile increasing HER results.

(2) Elongations from a uniaxial tensile test cannot be proper indicators for hole expansion performance. However, reduction in area has a reasonable correlation with HER, since both of them are indices indicating local deformation measurements.

(3) Numerous micro-voids and shearing dimples existing in the fracture zone act as the crack initiation sites and later severely influence HER values. Considering the deformed microstructures in the sheared edges in the wake of hole punching, voids nucleate associated with (i) the decohesion of interfaces between ferrite and hard constituents, (ii) martensite cracking, (iii) the presence of inclusions (i.e., MnS) and (iv) recrystallized ferrite/ferrite grain boundaries. With further plastic deformation (i.e., the step of hole expanding), the micro-cracks propagate, or micro-voids grow by void enlargement from the sheared edges towards sheared affected zones (SAZ) in a zigzagging fracture path, indicating that the fracture associated with hole expansion is ductile fracture.

(4) The EBSD-KAM values, evaluated  $\varepsilon_{eq}$  data and nanohardness measurements of the tested positions in the initial hole punched sheared edges for the selected fully annealed DP steels with both GI and SC anneals reveal that a large amount of plastic deformation is introduced by hole punching, and the influences of punching decrease as the distance from the initial punched hole increases. The maximum equivalent strain is at the burnished and fracture transition zone. Both soft ferrite and major hard constituents (fresh martensite (for GI anneals) and tempered martensite (for SC anneals)) can be work hardened by the step of hole punching. The punching damages for GI annealed DP steels are higher than those for the fully annealed DP steels with SC anneals, which helps explain the reason why the HER values of the SC annealed sample are always higher than those of GI annealed samples with the same pre-anneal conditions.

(5) The micro-fracture mechanism, in terms of hole expansion, was studied by performing incomplete HETs for the selected fully annealed DP samples with a variety of HER values. The SEM micrographs of the final hole internal surfaces indicate that the fracture of the ultra-high strength DP steels during HETs is still ductile fracture. The initial micro-voids and even micro-cracks are caused by hole punching in the fracture zones. In the early stage of hole expanding, voids start to grow by void enlargement or cracks begin to propagate in coexistence with continuing void nucleation, as plastic strain increases. As the conical punch continues going up, small cracks continue propagating from the fracture zone towards the burnished and rollover zones. The process continues until the major crack crosses the thickness of the tested sample, at which point the test is by definition stopped and the HET is completed. Further conical movement beyond this point will lead to artificially high and erroneous HER values.

## 10.0 Future Work

This study has investigated the influence of composition (i.e., Al and V contents) and processing (i.e., coiling temperatures and CGL simulations) on austenite formation and final mechanical properties of high-strength DP steels. The effects of coiling temperature and cold work on stored energy related to austenite formation during subsequent intercritical annealing were also discussed. The microstructure and damage evolutions in initial hole inner surface and sheared edges during hole punching and hole expansion were studied. For future directions, there are several suggestions:

1. The microstructure-mechanical property relationships for DP steels obtained in Chapter 8 revealed that the volume percentage of fresh martensite play a vital role in mechanical performances. Thus, in order to retard the transformation of lower bainite from intercritically formed austenite, 0.3 wt.% or more Mo could be added, for steel alloy design, recognizing increasing cost involved. Also, in order to minimize the formation of new ferrite during cooling for high Al microalloyed DP steels, faster cooling rates (i.e.,  $-100^{\circ}\text{C s}^{-1}$ ) should be applied. Additionally, quenching temperatures are reported to be related to both global ductility (i.e., UE and TE) and local ductility (i.e., HER). Three quenching temperatures (i.e.,  $250^{\circ}\text{C}$ ,  $300^{\circ}\text{C}$  and  $350^{\circ}\text{C}$ ) should be chosen as supercooling temperature in SC CGL simulations.

2. Chapter 9 emphasized the punching-induced damages and pre-strains which severely influenced stretch-flangeability of candidate DP steels. Other hole formation methods should be applied. The HER values of the same steel conditions with different hole formation approaches should be compared and the initial hole inner surfaces and hole edges for four methods should be examined via SEM. In addition, 3 dimensional (3D)-digital image correlation (DIC) is a non-

contact optical strain measurement and analysis technology. Compared with 2D-DIC, 3D-DIC has more capability of determining the out-of-plane strain. Thus, the punching-induced pre-strains, especially the one in the punching direction, will be better revealed by 3D-DIC technology. Furthermore, HER is reported to be associated with fracture toughness and Al-Jabr [201] found that Charpy V-notch impact toughness of HSLA steels were controlled by the percentage of {002} lattice planes. So, the correlation between the HER results and the fraction of {002} lattice planes 45 degrees to the punching direction should be studied for different steel grades.

## Bibliology

- [1] O. Bouaziz, H. Zurob, M. Huang, Driving force and logic of development of advanced high strength steels for automotive applications, *Steel Res. Int.* 84 (2013) 937–947. <https://doi.org/10.1002/srin.201200288>.
- [2] B.K. Zuidema, Bridging the design–manufacturing–materials data gap: material properties for optimum design and manufacturing performance in light vehicle steel-intensive body structures, *JOM.* 64 (2012) 1039–1047. <https://doi.org/10.1007/s11837-012-0405-2>.
- [3] C.P. Scott, F. Fazeli, B. Shalchi Amirkhiz, I. Pushkareva, S.Y.P. Allain, Structure-properties relationship of ultra-fine grained V-microalloyed dual phase steels, *Mater. Sci. Eng. A.* 703 (2017) 293–303. <https://doi.org/10.1016/j.msea.2017.07.051>.
- [4] C.C. Tasan, M. Diehl, D. Yan, M. Bechtold, F. Roters, L. Schemmann, C. Zheng, N. Peranio, D. Ponge, M. Koyama, K. Tsuzaki, D. Raabe, An overview of dual-phase steels: advances in microstructure-oriented processing and micromechanically guided design, *Annu. Rev. Mater. Res.* 45 (2015) 391–431. <https://doi.org/10.1146/annurev-matsci-070214-021103>.
- [5] R.G. Davies, The deformation behavior of a vanadium-strengthened dual phase steel, *Metall. Trans. A.* 9 (1978) 41–52. <https://doi.org/10.1007/BF02647169>.
- [6] R.G. Davies, Influence of martensite composition and content on the properties of dual phase steels, *Metall. Trans. A.* 9 (1978) 671–679. <https://doi.org/10.1007/BF02659924>.
- [7] R.G. Davies, Early stages of yielding and strain aging of a vanadium-containing dual-phase steel, *Metall. Trans. A.* 10 (1979) 1549–1555. <https://doi.org/10.1007/BF02812021>.
- [8] R.G. Davies, C.L. Magee, Physical metallurgy of automotive high-strength steels, *JOM.* 31 (1979) 17–23. <https://doi.org/10.1007/BF03354565>.
- [9] G.R. Speich, V.A. Demarest, R.L. Miller, Formation of austenite during intercritical annealing of dual-phase steels, *Metall. Mater. Trans. A.* 12 (1981) 1419–1428. <https://doi.org/10.1007/BF02643686>.
- [10] G.R. Speich, Physical metallurgy of dual-phase steels, in: R.A. Kot, B.L. Bramfitt (Eds.), *Fundam. Dual-Phase Steels Proc. a Symp.*, AIME, Chicago, 1981: pp. 3–45.
- [11] M.S. Rashid, B.V.N. Rao, Tempering characteristics of a vanadium containing dual phase steel, *Metall. Trans. A.* 13 (1982) 1679–1686. <https://doi.org/10.1007/BF02647823>.
- [12] D.P. Steels, M.S. Rashid, Dual phase steels, *Annu. Rev. Mater. Sci.* 11 (1981) 245–266. <https://doi.org/10.1146/annurev.ms.11.080181.001333>.

- [13] M. Calcagnotto, D. Ponge, D. Raabe, On the effect of manganese on grain size stability and hardenability in ultrafine-grained ferrite/martensite dual-phase steels, *Metall. Mater. Trans. A.* 43 (2012) 37–46. <https://doi.org/10.1007/s11661-011-0828-3>.
- [14] E.C. Bain, H.W. Paxton, *Alloying elements in steel*, 2nd ed., American Society of Metals, 1961.
- [15] Y. Toji, T. Yamashita, K. Nakajima, K. Okuda, H. Matsuda, K. Hasegawa, K. Seto, Effect of Mn partitioning during intercritical annealing on following  $\gamma \rightarrow \alpha$  transformation and resultant mechanical properties of cold-rolled dual phase steels, *ISIJ Int.* 51 (2011) 818–825. <https://doi.org/10.2355/isijinternational.51.818>.
- [16] L. Kong, Y. Liu, J. Liu, Y. Song, S. Li, R. Zhang, T. Li, Y. Liang, The influence of chromium on the pearlite-austenite transformation kinetics of the Fe–Cr–C ternary steels, *J. Alloys Compd.* 648 (2015) 494–499. <https://doi.org/10.1016/j.jallcom.2015.06.259>.
- [17] G. Krauss, *Steels-processing, structure, and performance*, ASM International, Materials Park, Ohio, 2005.
- [18] T. Furukawa, M. Tanino, H. Morikawa, M. Endo, Effects of composition and processing factors on the mechanical properties of as-hot-rolled dual-phase steels, *Trans. Iron Steel Inst. Japan.* 24 (1984) 113–121. <https://doi.org/10.2355/isijinternational1966.24.113>.
- [19] K. Sugimoto, N. Usui, M. Kobayashi, S. Hashimoto, Effects of volume fraction and stability of trip-aided of retained austenite on ductility dual-phase steels, *ISIJ Int.* 32 (1992) 1311–1318. <https://doi.org/10.2355/isijinternational.32.1311>.
- [20] O.A. Girina, N.M. Fonstein, Influence of Al additions on austenite decomposition in continuously annealed dual-phase steels, in: *Mater. Sci. Technol.* 2005, 2005: pp. 65–76.
- [21] N. Fonstein, *Advanced high strength sheet steels*, 2015. <https://doi.org/10.1007/978-3-319-19165-2>.
- [22] O. Girina, N. Fonstein, O. Yakubovsky, D. Panahi, D. Bhattacharya, S. Jansto, The influence of Mo, Cr and B alloying on phase transformation and mechanical properties in Nb added high strength dual phase steels, in: *HSLA Steels 2015, Microalloying 2015 Offshore Eng. Steels 2015*, Springer International Publishing, Cham, 2015: pp. 237–245. [https://doi.org/10.1007/978-3-319-48767-0\\_24](https://doi.org/10.1007/978-3-319-48767-0_24).
- [23] M.P. Rao, V.S. Sarma, S. Sankaran, Development of high strength and ductile ultra fine grained dual phase steel with nano sized carbide precipitates in a V–Nb microalloyed steel, *Mater. Sci. Eng. A.* 568 (2013) 171–175. <https://doi.org/10.1016/j.msea.2012.12.084>.
- [24] N. Terao, A. Baugnet, High-manganese dual-phase steels, strengthened by additional elements (Cr, Ti, V, W), *J. Mater. Sci.* 25 (1990) 848–858. <https://doi.org/10.1007/bf03372172>.

- [25] A.N. Bortsov, N.M. Fonstein, Distribution of strain between the phases of ferrite, *Phys. Metall. Metallogr.* 61 (1986) 74–81.
- [26] C.I. Garcia, K. Cho, K. Redkin, A.J. Deardo, S. Tan, M. Somani, L.P. Karjalainen, Influence of critical carbide dissolution temperature during intercritical annealing on hardenability of austenite and mechanical properties of DP-980 steels, *ISIJ Int.* 51 (2011) 969–974. <https://doi.org/10.2355/isijinternational.51.969>.
- [27] Y. Wu, A.J. Deardo, Processing , microstructures and properties of ultra- high strength , low varbon and V-bearing dual-phase steels produced on continuous galvanizing lines, in: *Mater. Sci. Technol.* 2018, MS T 2018, 2018: pp. 454–463. [https://doi.org/10.7449/2018/MST\\_2018\\_454\\_463](https://doi.org/10.7449/2018/MST_2018_454_463).
- [28] Y. Gong, J. Uusitalo, M. Hua, Y. Wu, A.J. DeArdo, Effects of pre-annealing conditions on the microstructure and properties of vanadium-bearing dual-phase steels produced using continuous galvanizing line simulations, *J. Mater. Sci.* 54 (2019) 7211–7230. <https://doi.org/10.1007/s10853-019-03338-6>.
- [29] Y. Gong, Y. Wu, M. Hua, J. Uusitalo, A.J. DeArdo, Influence of processing factors on the sheared-edge formability of vanadium bearing dual-phase steels produced using continuous galvanizing line simulations, *J. Mater. Sci.* 55 (2020) 5639–5654. <https://doi.org/10.1007/s10853-020-04385-0>.
- [30] N.K. Balliger, T. Gladman, Work hardening of dual-phase steels, *Met. Sci.* 15 (1981) 95–108. <https://doi.org/10.1179/030634581790426615>.
- [31] A.R. Marder, The effect of heat treatment on the properties and structure of molybdenum and vanadium dual-phase steels, *Metall. Trans. A.* 12 (1981) 1569–1579. <https://doi.org/10.1007/BF02643562>.
- [32] C.I. Garcia, M. Hua, K. Cho, K. Redkin, A.J. DeArdo, Metallurgy and continuous galvanizing line processing of high-strength dual-phase steels microalloyed with niobium and vanadium, *Metall. Ital.* 104 (2012) 3–8.
- [33] M.D. Taylor, K.S. Choi, X. Sun, D.K. Matlock, C.E. Packard, L. Xu, F. Barlat, Correlations between nanoindentation hardness and macroscopic mechanical properties in DP980 steels, *Mater. Sci. Eng. A.* 597 (2014) 431–439. <https://doi.org/10.1016/j.msea.2013.12.084>.
- [34] Y. Gong, The mechanical properties and microstructures of vanadium bearing high strength dual phase steels processed with continuous galvanizing line simulations, University of Pittsburgh, 2015.
- [35] H. Abe, S. Satoh, Progress of continuous annealing technology for cold rolled sheet steels and associated product development, *Kawasaki Steel Tech. Rep.* (1990) 48–56.
- [36] K. Yamato, T. Ichida, T. Irie, Progress in precoated steel sheets for automotive use, *Kawasaki Steel Tech. Rep.* (1990) 57–66.

- [37] K. Cho, K. V Redkin, M. Hua, C.I. Garcia, A.J. Deardo, Recent development of Nb-containing DP590, DP780 and DP980 steels for production on continuous galvanizing lines, in: *Adv. Steels*, 2011: pp. 177–185. <https://doi.org/10.1007/978-3-642-17665-4>.
- [38] N. Pottore, N. Fonstein, I. Gupta, D. Bhattacharya, A family of 980MPa tensile strength advanced high strength steels with various mechanical property attributes, *AHSSS Proceeding*. (2004) 119–129.
- [39] N. Pathak, C. Butcher, M. Worswick, E. Bellhouse, J. Gao, Damage evolution in complex-phase and dual-phase steels during edge stretching, *Materials (Basel)*. 10 (2017) 346. <https://doi.org/10.3390/ma10040346>.
- [40] A.K. Sachdev, Effect of retained austenite on the yielding and deformation behavior of a dual phase steel, *Acta Metall.* 31 (1983) 2037–2042. [https://doi.org/10.1016/0001-6160\(83\)90021-4](https://doi.org/10.1016/0001-6160(83)90021-4).
- [41] O. Matsumura, Y. Sakuma, H. Takechi, Enhancement intercritical of elongation annealed by retained austenite steel, *Trans. ISIJ*. 27 (1987) 570–579. [https://www.jstage.jst.go.jp/article/isijinternational1966/27/7/27\\_7\\_570/\\_pdf/-char/ja](https://www.jstage.jst.go.jp/article/isijinternational1966/27/7/27_7_570/_pdf/-char/ja).
- [42] Y. Sakuma, O. Matsumura, H. Takechi, Mechanical properties and retained austenite in intercritically heat-treated bainite-transformed steel and their variation with Si and Mn additions, *Metall. Trans. A*. 22 (1991) 489–498. <https://doi.org/10.1007/BF02656816>.
- [43] H. Huang, O. Matsumura, T. Furukawa, Retained austenite in low carbon, manganese steel after intercritical heat treatment, *Mater. Sci. Technol.* 10 (1994) 621–626. <https://doi.org/10.1179/mst.1994.10.7.621>.
- [44] J. Chiang, J.D. Boyd, A.K. Pilkey, Effect of microstructure on retained austenite stability and tensile behaviour in an aluminum-alloyed TRIP steel, *Mater. Sci. Eng. A*. 638 (2015) 132–142. <https://doi.org/10.1016/j.msea.2015.03.069>.
- [45] J. Speer, D.K. Matlock, B.C. De Cooman, J.G. Schroth, Carbon partitioning into austenite after martensite transformation, *Acta Mater.* 51 (2003) 2611–2622. [https://doi.org/10.1016/S1359-6454\(03\)00059-4](https://doi.org/10.1016/S1359-6454(03)00059-4).
- [46] Y. Wu, A.J. DeArdo, Processing , microstructures and properties of ultra- high strength , low carbon and V-bearing dual-phase steels produced on continuous galvanizing lines, in: *Mater. Sci. Technol.* 2018, MS T 2018, 2019. [https://doi.org/10.7449/2018/MST\\_2018\\_454\\_463](https://doi.org/10.7449/2018/MST_2018_454_463).
- [47] C.M. Tamarelli, The evolving use of advanced high-strength steels for automotive applications, 2011.
- [48] S. Hayami, T. Furukawa, A family of high-strength, cold rolled steels, in: *Microalloying* 75, 1975: pp. 311–320.

- [49] S.K. Nath, S. Ray, V.N.S. Mathur, M.L. Kapoor, Non-isothermal austenitisation kinetics and theoretical determination of intercritical annealing time for dual-phase steels., *ISIJ Int.* 34 (1994) 191–197. <https://doi.org/10.2355/isijinternational.34.191>.
- [50] D. Barbier, L. Germain, A. Hazotte, M. Gouné, A. Chbihi, Microstructures resulting from the interaction between ferrite recrystallization and austenite formation in dual-phase steels, *J. Mater. Sci.* 50 (2015) 374–381. <https://doi.org/10.1007/s10853-014-8596-2>.
- [51] C.I. Garcia, A.J. Deardo, Formation of austenite in 1.5 pct Mn steels, *Metall. Trans. A.* 12 (1981) 521–530. <https://doi.org/10.1007/BF02648551>.
- [52] D.Z. Yang, E.L. Brown, D.K. Matlock, G. Krauss, Ferrite recrystallization and austenite formation in cold-rolled intercritically annealed steel, *Metall. Trans. A.* 16 (1985) 1385–1392. <https://doi.org/10.1007/BF02658671>.
- [53] J. Huang, W.J. Poole, M. Militzer, Austenite formation during intercritical annealing, *Metall. Mater. Trans. A.* 35 (2004) 3363–3375. <https://doi.org/10.1007/s11661-004-0173-x>.
- [54] R.A. Grange, Estimating the hardenability of carbon steels, *Metall. Trans.* 4 (1973) 2231–2244. <https://doi.org/10.1007/BF02669363>.
- [55] K. Cho, C.I. Garcia, M. Hua, J. Lee, Y.S. Ahn, A.J. DeArdo, A new method to study the effect of cooling rate on the decomposition of austenite in advanced high strength sheet steels, *J. ASTM Int.* 6 (2009) 1–12. <https://doi.org/10.1520/stp49187s>.
- [56] P.E. RePas, Metallurgy, production, technology, and properties of dual-phase steels, in: *Dual-Phase Cold-Forming Vanadium Steels Automob. Ind.*, 1978: pp. 13–22.
- [57] P.E. RePas, Physical metallurgy of dual-phase steels, in: *Mech. Work. Steel Process. Conf. XVII, AIME, New York*, 1979: pp. 277–305.
- [58] R.R. Mohanty, O.A. Girina, N.M. Fonstein, Effect of heating rate on the austenite formation in low-carbon high-strength steels annealed in the intercritical region, *Metall. Mater. Trans. A Phys. Metall. Mater. Sci.* 42 (2011) 3680–3690. <https://doi.org/10.1007/s11661-011-0753-5>.
- [59] T. Tanaka, M. Nishida, K. Hashiguchi, Structure and properties of dual phase steels, in: *Struct. Prop. Dual-Phase Steels Proc. a Symp.*, 1979: pp. 221–241.
- [60] S.J. Barnard, G.D.W. Smith, M. Sarikaya, G. Thomas, Carbon atom distribution in a dual phase steel: an atom probe study, *Scr. Mater.* 15 (1981) 387–392.
- [61] M.H. Saleh, R. Priestner, Retained austenite in dual-phase silicon steels and its effect on mechanical properties, *J. Mater. Process. Technol.* 113 (2001) 587–593. [https://doi.org/10.1016/S0924-0136\(01\)00638-0](https://doi.org/10.1016/S0924-0136(01)00638-0).

- [62] K. Sugimoto, M. Misu, M. Kobayashi, H. Shirasawa, Effects of second phase morphology on retained austenite morphology and tensile properties in a TRIP-aided dual-phase steel sheet, *ISIJ Int.* 33 (1993) 775–782. <https://doi.org/10.2355/isijinternational.33.775>.
- [63] A. Eggbauer, G. Ressel, M. Gruber, P. Prevedel, S. Marsoner, A. Stark, R. Ebner, Different cooling rates and their effect on morphology and transformation kinetics of martensite, in: A.P. Stebner, G.B. Olson (Eds.), *Proc. Int. Conf. Martensitic Transform.*, Chicago, 2018: pp. 35–40.
- [64] O. Matsumura, Y. Sakuma, H. Takechi, Retained austenite in 0.4C-Si-1.2Mn steel sheet intercritically heated and austempered, *ISIJ Int.* 32 (1992) 1014–1020. <https://doi.org/10.2355/isijinternational.32.1014>.
- [65] K. Sugimoto, A. Nagasaka, M. Kobayashi, S. Hashimoto, Effects of retained austenite parameters on warm stretchflangeability in TRIP-aided dual-phase sheet steels., *ISIJ Int.* 39 (1999) 56–63. <https://doi.org/10.2355/isijinternational.39.56>.
- [66] C. Zheng, D. Raabe, Interaction between recrystallization and phase transformation during intercritical annealing in a cold-rolled dual-phase steel: A cellular automaton model, *Acta Mater.* 61 (2013) 5504–5517. <https://doi.org/10.1016/j.actamat.2013.05.040>.
- [67] J.W. Christian, *The theory of transformations in metals and alloys*, Oxford, UK, 2002.
- [68] I. Loginova, J. Odqvist, G. Amberg, J. Ågren, The phase-field approach and solute drag modeling of the transition to massive  $\gamma \rightarrow \alpha$  transformation in binary Fe-C alloys, *Acta Mater.* 51 (2003) 1327–1339. [https://doi.org/10.1016/S1359-6454\(02\)00527-X](https://doi.org/10.1016/S1359-6454(02)00527-X).
- [69] J. Sietsma, S. Van Der Zwaag, A concise model for mixed-mode phase transformations in the solid state, *Acta Mater.* 52 (2004) 4143–4152. <https://doi.org/10.1016/j.actamat.2004.05.027>.
- [70] M.A. Grossmann, Hardenability calculated from chemical composition, *Met. Technol.* 1437 (1942) 1–29.
- [71] D. V. Doane, Application of hardenability concepts in heat treatment of steel, *J. Heat Treat.* 1 (1979) 5–30. <https://doi.org/10.1007/BF02833206>.
- [72] R. Pradhan, Continuously annealed cold-rolled microalloyed steels with different microstructures, in: *Int. Conf. Technol. Appl. HSLA Steels*, Philadelphia, PA, USA, 1983: pp. 193–201. <http://joi.jlc.jst.go.jp/JST.JSTAGE/isijinternational/51.818?from=CrossRef>.
- [73] C. Philippot, M. Bellavoine, M. Dumont, K. Hoummada, J. Drillet, V. Hebert, P. Maugis, Influence of heating rate on ferrite recrystallization and austenite formation in cold-rolled microalloyed dual-phase steels, *Metall. Mater. Trans. A.* 49 (2018) 66–77. <https://doi.org/10.1007/s11661-017-4407-0>.

- [74] P. Li, J. Li, Q. Meng, W. Hu, D. Xu, Effect of heating rate on ferrite recrystallization and austenite formation of cold-roll dual phase steel, *J. Alloys Compd.* 578 (2013) 320–327. <https://doi.org/10.1016/j.jallcom.2013.05.226>.
- [75] H. Xu, W. Cao, H. Dong, J. Li, Effects of aluminum on the microstructure and mechanical properties in 0.2C–5Mn steels under different heat treatment conditions, *ISIJ Int.* 55 (2015) 662–669. <https://doi.org/10.2355/isijinternational.55.662>.
- [76] D.T. Pierce, J.A. Jiménez, J. Bentley, D. Raabe, J.E. Wittig, The influence of stacking fault energy on the microstructural and strain-hardening evolution of Fe-Mn-Al-Si steels during tensile deformation, *Acta Mater.* 100 (2015) 178–190. <https://doi.org/10.1016/j.actamat.2015.08.030>.
- [77] H. Kang, C.I. Garcia, K. Chin, A.J. Deardo, Effect of aluminum content on the mechanical properties of dual stabilized Ti-Nb interstitial free high strength steel (IF-HSS), *ISIJ Int.* 47 (2007) 486–492. <https://doi.org/10.2355/isijinternational.47.486>.
- [78] N. Kamikawa, M. Hirohashi, Y. Sato, E. Chandiran, G. Miyamoto, T. Furuhashi, Tensile behavior of ferrite-martensite dual phase steels with nano-precipitation of vanadium carbides, *ISIJ Int.* 55 (2015) 1781–1790. <https://doi.org/10.2355/isijinternational.isijint-2015-106>.
- [79] A. Kelly, W.R. Tyson, Tensile properties of fiber-reinforced metals: copper/tungsten and copper/molybdenum, *J. Mech. Phys. Solids.* 13 (1965) 329–350.
- [80] S.T. Mileiko, The tensile strength and ductility of continuous fibre composites, *J. Mater. Sci.* 4 (1969) 974–977. <https://doi.org/10.1007/BF00555312>.
- [81] G. Garmon, R.B. Thompson, A theory for the mechanical properties of metal-matrix composites at ultimate loading loading, *Metall. Trans.* 4 (1973) 863–873. <https://doi.org/10.1007/bf02669398>.
- [82] E.O. Hall, The deformation and ageing of mild steel: III discussion of results, *Proc. Phys. Soc. Sect. B.* 64 (1951) 747–753. <https://doi.org/10.1088/0370-1301/64/9/302>.
- [83] N.J. Petch, The cleavage strength of polycrystals, *J. Iron Steel Inst.* 174 (1953) 25–28. <https://doi.org/10.1007/BF01972547>.
- [84] N. Hansen, Hall-petch relation and boundary strengthening, *Scr. Mater.* 51 (2004) 801–806. <https://doi.org/10.1016/j.scriptamat.2004.06.002>.
- [85] J.C.M.C. Li, Petch relation and grain boundary sources, *Trans. Met. Soc. AIME.* 227 (1963) 239–247.
- [86] A.M. Sherman, R.G. Davies, W.T. Donlon, Electron microscope study of deformed dual-phase steels, in: *Fundam. Dual-Phase Steels Proc. a Symp.*, 1981: pp. 85–94.

- [87] N. Hansen, B. Ralph, The strain and grain size dependence of the flow stress of copper, *Acta Mater.* 30 (1982) 411–417.
- [88] G.E. Dieter, *Mechanical metallurgy*, McGraw-Hill, London, 1988.
- [89] A.J. DeArdo, M.J. Hua, K.G. Cho, C.I. Garcia, On strength of microalloyed steels: an interpretive review, *Mater. Sci. Technol.* 25 (2009) 1074–1082. <https://doi.org/10.1179/174328409x455233>.
- [90] T. Gladman, Precipitation hardening in metals, *Mater. Sci. Technol.* 15 (1999) 30–36. <https://doi.org/10.1179/026708399773002782>.
- [91] E. Orowan, Internal stress in metals and alloys, in: *Symp. Intern. Stress Met. Alloy.*, The Institute of Metals, London, 1948: pp. 451–453.
- [92] M.F. Ashby, Oxide dispersion strengthening, in: G.S. Ansell (Ed.), *Metall. Soc. Conf. Vol. 47*, Gordon and Breach, New York, 1968: pp. 143–205.
- [93] Y. Wu, J. Uusitalo, A.J. DeArdo, Stored energy evaluation for high strength dual-phase steels with different pre-annealing conditions, *Metall. Mater. Trans. A.* 51 (2020) 4727–4741. <https://doi.org/10.1007/s11661-020-05890-2>.
- [94] M.B. Bever, L.B. Ticknor, A method for determining the energy stored during cold-working of metals, *J. Appl. Phys.* 22 (1951) 1297–1298. <https://doi.org/10.1063/1.1699852>.
- [95] J.S.L. Leach, E.G. Loewen, M.B. Bever, Energy relations in cold working an alloy at 78°K and at room temperature, *J. Appl. Phys.* 26 (1955) 728–731. <https://doi.org/10.1063/1.1722080>.
- [96] M.S. Paterson, X-ray line broadening in plastically deformed calcite, *Philos. Mag.* 4 (1959) 451–466. <https://doi.org/10.1080/14786435908233415>.
- [97] J.L. White, K. Koyama, Application of differential thermal calorimetry to measurements of stored-energy release in metals, *Rev. Sci. Instrum.* 34 (1963) 1104–1110. <https://doi.org/10.1063/1.1718143>.
- [98] I.L. Dillamore, C.J.E. Smith, T.W. Watson, Oriented nucleation in the formation of annealing textures in iron, *Met. Sci. J.* 1 (1967) 49–54. <https://doi.org/10.1179/msc.1967.1.1.49>.
- [99] S.H. Choi, Y.S. Jin, Evaluation of stored energy in cold-rolled steels from EBSD data, *Mater. Sci. Eng. A.* 371 (2004) 149–159. <https://doi.org/10.1016/j.msea.2003.11.034>.
- [100] C. Fang, C.I. Garcia, S.-H. Choi, A.J. DeArdo, A Study of the batch annealing of cold-rolled HSLA steels containing niobium or titanium, *Metall. Mater. Trans. A.* 46 (2015) 3635–3645. <https://doi.org/10.1007/s11661-015-2949-6>.

- [101] E.S. Watson, M.J. O'Neill, US Patent 3,263,484 differential microcalorimeter, 1962. <https://patents.google.com/patent/US3263484>.
- [102] J. Lendvai, G. Honyek, A. Juhász, I. Kovács, A differential scanning calorimetry study of the release of stored energy in an Al-Fe alloy, *Scr. Metall.* 19 (1985) 943–946. [https://doi.org/10.1016/0036-9748\(85\)90288-1](https://doi.org/10.1016/0036-9748(85)90288-1).
- [103] T. Knudsen, W.Q. Cao, A. Godfrey, Q. Liu, N. Hansen, Stored energy in nickel cold rolled to large strains, Measured by calorimetry and evaluated from the microstructure, *Metall. Mater. Trans. A.* 39 (2008) 430–440. <https://doi.org/10.1007/s11661-007-9421-1>.
- [104] S.S. Hazra, A.A. Gazder, E. V. Pereloma, Stored energy of a severely deformed interstitial free steel, *Mater. Sci. Eng. A.* 524 (2009) 158–167. <https://doi.org/10.1016/j.msea.2009.06.033>.
- [105] M.S. PATERSON, E. OROWAN, X-ray line broadening in cold-worked metals, *Nature.* 162 (1948) 991–992. <https://doi.org/10.1038/162991a0>.
- [106] J.S. Kallend, Y.C. Huang, Orientation dependence of stored energy of cold work in 50% cold rolled copper, *Met. Sci.* 18 (1984) 381–386. <https://doi.org/10.1179/030634584790419890>.
- [107] N. Rajmohan, Y. Hayakawa, J.A. Szpunar, J.H. Root, Neutron diffraction method for stored energy measurement in interstitial free steel, *Acta Mater.* 45 (1997) 2485–2494. [https://doi.org/10.1016/S1359-6454\(96\)00371-0](https://doi.org/10.1016/S1359-6454(96)00371-0).
- [108] W.. Read, W. Shockley, Dislocation model of crystal grain boundaries, *Phys. Rev.* 78 (1950) 275–289. <https://doi.org/10.1103/PhysRev.78.275>.
- [109] W. Read, *Dislocations in crystals*, McGraw-Hill, 1953.
- [110] S.I. Wright, M.M. Nowell, D.P. Field, S. I. Wright, M. M. Nowell, D. P. Field, A review of strain analysis using electron backscatter diffraction, *Microsc. Microanal.* 17 (2011) 316–329. <https://doi.org/10.1017/S1431927611000055>.
- [111] M.F. Ashby, R. Roscoe, The deformation of plastically non-homogeneous materials, *Philos. Mag.* 21 (1970) 399–424. <https://doi.org/10.1080/14786437008238426>.
- [112] M. Calcagnotto, D. Ponge, E. Demir, D. Raabe, Orientation gradients and geometrically necessary dislocations in ultrafine grained dual-phase steels studied by 2D and 3D EBSD, *Mater. Sci. Eng. A.* 527 (2010) 2738–2746. <https://doi.org/10.1016/j.msea.2010.01.004>.
- [113] Y. Takayama, J.A. Szpunar, Stored energy and taylor factor relation in an Al-Mg-Mn alloy sheet worked by continuous cyclic bending, *Mater. Trans.* 45 (2004) 2316–2325. <https://doi.org/10.2320/matertrans.45.2316>.
- [114] R.D. Adamczyk, G.M. Michal, Sheared edge extension of high-strength cold-rolled steels, *J. Appl. Metalwork.* 4 (1986) 157–163. <https://doi.org/10.1007/BF02834379>.

- [115] J.I. Yoon, J. Jung, H.H. Lee, G.-S. Kim, H.S. Kim, Factors governing hole expansion ratio of steel sheets with smooth sheared edge, *Met. Mater. Int.* 22 (2016) 1009–1014. <https://doi.org/10.1007/s12540-016-6346-5>.
- [116] X. Fang, Z. Fan, B. Ralph, P. Evans, R. Underhill, The relationships between tensile properties and hole expansion property of C-Mn steels, *J. Mater. Sci.* 38 (2003) 3877–3882. <https://doi.org/10.1023/A:1025913123832>.
- [117] J.H. Kim, Y.J. Kwon, T. Lee, K.-A. Lee, H.S. Kim, C.S. Lee, Prediction of hole expansion ratio for various steel sheets based on uniaxial tensile properties, *Met. Mater. Int.* 24 (2018) 187–194. <https://doi.org/10.1007/s12540-017-7288-2>.
- [118] A. Kamp, S. Celotto, D.N. Hanlon, Effects of tempering on the mechanical properties of high strength dual-phase steels, *Mater. Sci. Eng. A.* 538 (2012) 35–41. <https://doi.org/10.1016/j.msea.2012.01.008>.
- [119] S.K. Paul, Non-linear correlation between uniaxial tensile properties and shear-edge hole expansion ratio, *J. Mater. Eng. Perform.* 23 (2014) 3610–3619. <https://doi.org/10.1007/s11665-014-1161-y>.
- [120] O.R. Terrazas, K.O. Findley, C.J. Van Tyne, Influence of martensite morphology on sheared-edge formability of dual-phase steels, *ISIJ Int.* 57 (2017) 937–944. <https://doi.org/10.2355/isijinternational.ISIJINT-2016-602>.
- [121] L. Chen, J.-K. Kim, S.-K. Kim, G.-S. Kim, K.-G. Chin, B.C. De Cooman, Stretch-flangeability of high Mn TWIP steel, *Steel Res. Int.* 81 (2010) 552–568. <https://doi.org/10.1002/srin.201000044>.
- [122] Y. Gong, M. Hua, J. Uusitalo, A.J. Deardo, Processing factors that influence the microstructure and properties of high-strength dual-phase steels produced using CGL simulations, in: *AISTech 2016 Proc.*, 2016: pp. 2779–2790.
- [123] R.J. Comstock, D.K. Scherrer, R.D. Adamczyk, Hole expansion in a variety of sheet steels, *J. Mater. Eng. Perform.* 15 (2006) 675–683. <https://doi.org/10.1361/105994906X150830>.
- [124] S. Sadagopan, D. Urban, C. Wong, M. Huang, B. Yan, Formability characterization of a new generation high strength steels, 2003.
- [125] J.I. Yoon, J. Jung, J.G. Kim, S.S. Sohn, S. Lee, H.S. Kim, Key factors of stretch-flangeability of sheet materials, *J. Mater. Sci.* 52 (2017) 7808–7823. <https://doi.org/10.1007/s10853-017-1012-y>.
- [126] H. Gwon, J.H. Kim, J.-K. Kim, D.-W. Suh, S.-J. Kim, Role of grain size on deformation microstructures and stretch-flangeability of TWIP steel, *Mater. Sci. Eng. A.* 773 (2020) 138861. <https://doi.org/10.1016/j.msea.2019.138861>.

- [127] J.H. Kim, E.J. Seo, M.H. Kwon, S. Kang, B.C. De Cooman, Effect of quenching temperature on stretch flangeability of a medium Mn steel processed by quenching and partitioning, *Mater. Sci. Eng. A.* 729 (2018) 276–284. <https://doi.org/10.1016/j.msea.2018.05.083>.
- [128] K. Hasegawa, K. Kawamura, T. Urabe, Y. Hosoya, Effects of microstructure on stretch-flange-formability of 980 MPa grade cold-rolled ultra high strength steel sheets, *ISIJ Int.* 44 (2004) 603–609. <https://doi.org/10.2355/isijinternational.44.603>.
- [129] B.S. Levy, C.J. Van Tyne, Review of the shearing process for sheet steels and its effect on sheared-edge stretching, *J. Mater. Eng. Perform.* 21 (2012) 1205–1213. <https://doi.org/10.1007/s11665-011-9997-x>.
- [130] Y. Wu, J. Uusitalo, A.J. DeArdo, Investigation of effects of processing on stretch-flangeability of the ultra-high strength, vanadium-bearing dual-phase steels, *Mater. Sci. Eng. A.* 797 (2020) 140094. <https://doi.org/10.1016/j.msea.2020.140094>.
- [131] B.S. Levy, M. Gibbs, C.J. Van Tyne, Failure during sheared edge stretching of dual-phase steels, *Metall. Mater. Trans. A.* 44 (2013) 3635–3648. <https://doi.org/10.1007/s11661-013-1718-7>.
- [132] T. Okano, C. Inoue, S. Suzuki, K. Yamazaki, S. Toyoda, Reduction of cracks during punching process by cementite in high tensile strength steel sheets, *Metall. Mater. Trans. A Phys. Metall. Mater. Sci.* 50 (2019) 884–893. <https://doi.org/10.1007/s11661-018-5043-z>.
- [133] T. Sirinakorn, V. Uthaisangasuk, S. Srimanosaowapark, Effects of the tempering temperature on mechanical properties of dual phase steels, *J. Met. Mater. Miner.* 24 (2014) 13–20. <https://doi.org/10.14456/jmmm.2014.3>.
- [134] D. Chilutti, A. Deardo, Metallographic study of sheared edge cracking of advanced high strength steels in expanded state (Unpublished), 2015.
- [135] M. Skapik, A. Deardo, Metallographic study of sheared edge cracking of advanced high strength steels in a pre-expanded state (Unpublished), 2015.
- [136] S. Cherry, Y. Wei, Y. Zheng, Edge ductility testing of high strength steels for the automobile industry (Unpublished), 2016.
- [137] F.J. Humphreys, Grain and subgrain characterisation by electron backscatter diffraction, *J. Mater. Sci.* 36 (2001) 3833–3854. <https://doi.org/10.1023/A:1017973432592>.
- [138] R.D. Doherty, Primary recrystallization, in: *Encycl. Mater. Sci. Technol.*, Elsevier, 2001: pp. 7847–7850. <https://doi.org/10.1016/B0-08-043152-6/01410-8>.
- [139] I.L. Dillamore, P.L. Morris, C.J.E. Smith, W.B. Hutchinson, Transition bands and recrystallization in metals, in: *Proc. R. Soc. London. A. Math. Phys. Sci.*, 1972: pp. 405–420. <https://doi.org/10.1098/rspa.1972.0120>.

- [140] X. Tao, A. Eades, Alternatives to image quality (IQ) mapping in EBSD, *Microsc. Microanal.* 8 (2019) 2002. <https://doi.org/10.1017/S1431927602106465>.
- [141] J. Wu, P.J. Wray, C.I. Garcia, M. Hua, A.J. DeArdo, Image quality analysis: a new method of characterizing microstructures, *ISIJ Int.* 45 (2006) 254–262. <https://doi.org/10.2355/isijinternational.45.254>.
- [142] S.I. Wright, M.M. Nowell, EBSD image quality mapping, *Microsc. Microanal.* 12 (2006) 72–84. <https://doi.org/10.1017/S1431927606060090>.
- [143] J. Tarasiuk, P. Gerber, B. Bacroix, K. Piekos, Modeling of recrystallization using Monte Carlo method based on EBSD data, *Mater. Sci. Forum.* 408–412 (2002) 395–400. <https://doi.org/10.4028/www.scientific.net/MSF.408-412.395>.
- [144] Y. Ateba Betanda, A.L. Helbert, F. Brisset, M.H. Mathon, T. Waeckerlé, T. Baudin, Measurement of stored energy in Fe-48%Ni alloys strongly cold-rolled using three approaches: Neutron diffraction, Dillamore and KAM approaches, *Mater. Sci. Eng. A.* 614 (2014) 193–198. <https://doi.org/10.1016/j.msea.2014.07.037>.
- [145] D.A. Hughes, N. Hansen, D.J. Bammann, Geometrically necessary boundaries, incidental dislocation boundaries and geometrically necessary dislocations, *Scr. Mater.* 48 (2003) 147–153. [https://doi.org/10.1016/S1359-6462\(02\)00358-5](https://doi.org/10.1016/S1359-6462(02)00358-5).
- [146] H. Gao, Y. Huang, Geometrically necessary dislocation and size-dependent plasticity, *Scr. Mater.* 48 (2003) 113–118. [https://doi.org/10.1016/S1359-6462\(02\)00329-9](https://doi.org/10.1016/S1359-6462(02)00329-9).
- [147] H. Wawra, Die Kröner-Grenzen der Elastizitätsmoduln technisch wichtiger Werkstoffe, *Zeitschrift Für Met.* 69 (1978) 518–523.
- [148] E.E. Underwood, *Quantitative microscopy*, McGraw-Hill, New York, 1968.
- [149] E562-11 Standard test method for determining volume fraction by systematic manual point count, in: ASTM, ASTM International, West Conshohocken, PA, 2019: pp. 1–7. <https://doi.org/10.1520/E0562-19E01>.
- [150] ASTM E8, ASTM E8/E8M standard test methods for tension testing of metallic materials 1, *Annu. B. ASTM Stand.* 4. (2010) 1–27. <https://doi.org/10.1520/E0008>.
- [151] ISO/TS 16630:2003 metallic materials-method of hole expanding test, 2003.
- [152] J. Reesman, J. Bartczak, B. Griman, Hole expansion ratio testing (unpublished), 2014.
- [153] P.A. Soloski, N.J. Thimons, A.A. Marks, J. Hartle, Q. Trest, A. Johnston, W. Perisse, A.J. DeArdo, Sheared-edge ductility/hole-expansion ratio testing of advanced high-strength steels, in: *Contrib. Pap. from Mater. Sci. Technol.* 2015, Columbus, 2015: pp. 917–926.

- [154] N. Nakada, K. Ikeda, H. Shuto, T. Yokoi, T. Tsuchiyama, S. Hata, H. Nakashima, S. Takaki, Quantification of large deformation with punching in dual phase steel and change of its microstructure –Part II: Local strain mapping of dual phase steel by a combination technique of electron backscatter diffraction and digital image correlation methods, *ISIJ Int.* 56 (2016) 2077–2083. <https://doi.org/10.2355/isijinternational.ISIJINT-2016-310>.
- [155] W.C. Oliver, G.M. Pharr, An improved technique for determining hardness and elastic modulus using load and displacement sensing indentation experiments, *J. Mater. Res.* 7 (1992) 1564–1583. <https://doi.org/10.1557/JMR.1992.1564>.
- [156] A.J. Wilkinson, T. Ben Britton, Strains, planes, and EBSD in materials science, *Mater. Today.* 15 (2012) 366–376. [https://doi.org/10.1016/S1369-7021\(12\)70163-3](https://doi.org/10.1016/S1369-7021(12)70163-3).
- [157] B. Jeong, EBSD study of martensite in a dual phase steel, *Met. Mater.* 8 (2002) 700–701.
- [158] C. Moussa, M. Bernacki, R. Besnard, N. Bozzolo, About quantitative EBSD analysis of deformation and recovery substructures in pure Tantalum, *IOP Conf. Ser. Mater. Sci. Eng.* 89 (2015). <https://doi.org/10.1088/1757-899X/89/1/012038>.
- [159] G. Krauss, S.W. Thompson, Ferritic microstructures in continuously cooled low- and ultralow-carbon steels., *ISIJ Int.* 35 (1995) 937–945. <https://doi.org/10.2355/isijinternational.35.937>.
- [160] D. Kuhlmann-Wilsdorf, Theory of plastic deformation: - properties of low energy dislocation structures, *Mater. Sci. Eng. A.* 113 (1989) 1–41. [https://doi.org/10.1016/0921-5093\(89\)90290-6](https://doi.org/10.1016/0921-5093(89)90290-6).
- [161] D. Kuhlmann-Wilsdorf, N. Hansen, Geometrically necessary, incidental and subgrain boundaries, *Scr. Metall. Mater.* 25 (1991) 1557–1562. [https://doi.org/10.1016/0956-716X\(91\)90451-6](https://doi.org/10.1016/0956-716X(91)90451-6).
- [162] H. Mughrabi, Dislocation wall and cell structures and long-range internal stresses in deformed metal crystals, *Acta Metall.* 31 (1983) 1367–1379. [https://doi.org/10.1016/0001-6160\(83\)90007-X](https://doi.org/10.1016/0001-6160(83)90007-X).
- [163] J.J. Yi, I.S. Kim, H.S. Choi, Austenitization during intercritical annealing of an Fe-C-Si-Mn dual-phase steel, *Metall. Trans. A.* 16 (1985) 1237–1245. <https://doi.org/10.1007/BF02670328>.
- [164] Z.D. Li, G. Miyamoto, Z.G. Yang, T. Furuhashi, Kinetics of reverse transformation from pearlite to austenite in an Fe-0.6 mass pct C alloy and the effects of alloying elements, *Metall. Mater. Trans. A Phys. Metall. Mater. Sci.* 42 (2011) 1586–1596. <https://doi.org/10.1007/s11661-010-0560-4>.
- [165] M. Asadi Asadabad, M. Goodarzi, S. Kheirandish, Kinetics of austenite formation in dual phase steels, *ISIJ Int.* 48 (2008) 1251–1255. <https://doi.org/10.2355/isijinternational.48.1251>.

- [166] J. Mahieu, D. Van Dooren, L. Barbé, B.C. De Cooman, Influence of Al, Si and P on the kinetics of intercritical annealing of TRIP-aided steels: thermodynamical prediction and experimental verification, *Steel Res.* 73 (2002) 267–273. <https://doi.org/10.1002/srin.200200207>.
- [167] S.A. Etesami, M.H. Enayati, A.G. Kalashami, Austenite formation and mechanical properties of a cold rolled ferrite-martensite structure during intercritical annealing, *Mater. Sci. Eng. A.* 682 (2017) 296–303. <https://doi.org/10.1016/j.msea.2016.09.112>.
- [168] K. Barmak, A commentary on: “Reaction kinetics in processes of nucleation and growth,” *Metall. Mater. Trans. B.* 49 (2018) 3616–3680. <https://doi.org/10.1007/s11663-010-9421-1>.
- [169] J. Kohout, An alternative to the JMAK equation for a better description of phase transformation kinetics, *J. Mater. Sci.* 43 (2008) 1334–1339. <https://doi.org/10.1007/s10853-007-2255-9>.
- [170] N.X. Sun, X.D. Liu, K. Lu, An explanation to the anomalous avrami exponent, *Scr. Mater.* 34 (1996) 1201–1207. [https://doi.org/10.1016/1359-6462\(95\)00657-5](https://doi.org/10.1016/1359-6462(95)00657-5).
- [171] F.G. Caballero, C. Capdevila, C.G. De Andrés, Modelling of kinetics of austenite formation in steels with different initial microstructures, *ISIJ Int.* 41 (2001) 1093–1102. <https://doi.org/10.2355/isijinternational.41.1093>.
- [172] F.G. Caballero, C. Capdevila, C.G. de Andrés, Influence of pearlite morphology and heating rate on the kinetics of continuously heated austenite formation in a eutectoid steel, *Metall. Mater. Trans. A.* 32 (2001) 1283–1291. <https://doi.org/10.1007/s11661-001-0218-3>.
- [173] Y. Mazaheri, A. Kermanpur, A. Najafizadeh, A.G. Kalashami, Kinetics of ferrite recrystallization and austenite formation during intercritical annealing of the cold-rolled ferrite/martensite duplex structures, *Metall. Mater. Trans. A.* 47 (2016) 1040–1051. <https://doi.org/10.1007/s11661-015-3288-3>.
- [174] E.S. Machlin, An introduction to aspects of thermodynamics and kinetics relevant to materials science, Elsevier, 2007. <https://doi.org/10.1016/B978-0-08-046615-6.X5016-4>.
- [175] S. Van der Zwaag, Kinetics of phase transformations in steels, in: *Phase Transform. Steels*, 2012: pp. 126–156. <https://doi.org/10.1533/9780857096104.1.126>.
- [176] Z. Guo, W. Sha, D. Li, Quantification of phase transformation kinetics of 18 wt.% Ni C250 maraging steel, *Mater. Sci. Eng. A.* 373 (2004) 10–20. <https://doi.org/10.1016/j.msea.2004.01.040>.
- [177] C.A. Wert, Diffusion coefficient of C in  $\alpha$ -iron, *Phys. Rev.* 79 (1950) 601–605. <https://doi.org/10.1103/PhysRev.79.601>.

- [178] H. Sueyoshi, K. Suenaga, R. Tanaka, Effect of austenitizing treatment followed by slow cooling on graphitization in hypo-eutectoid alloy steels, *J. Japan Inst. Met.* 51 (1987) 518–524. [https://doi.org/10.2320/jinstmet1952.51.6\\_518](https://doi.org/10.2320/jinstmet1952.51.6_518).
- [179] S.S. Babu, H.K.D.H. Bhadeshia, Diffusion of carbon in substitutionally alloyed austenite, *J. Mater. Sci. Lett.* 14 (1995) 314–316. <https://doi.org/10.1007/BF00592135>.
- [180] P.A. Wycliffe, G.R. Purdy, J.D. Embury, Growth of austenite in the intercritical annealing of Fe-C-Mn dual phase steels, *Can. Metall. Q.* 20 (1981) 339–350. <https://doi.org/10.1179/cm.1981.20.3.339>.
- [181] T. Nakayama, N. Honjou, Effect of aluminum and nitrogen on the magnetic properties of non-oriented semi-processed electrical steel sheet, *J. Magn. Magn. Mater.* 213 (2000) 87–94. [https://doi.org/10.1016/S0304-8853\(00\)00005-6](https://doi.org/10.1016/S0304-8853(00)00005-6).
- [182] W.C. Jeong, Role of aluminum in hot-rolled ultra-low-carbon Nb-interstitial-free steels, *Metall. Mater. Trans. A Phys. Metall. Mater. Sci.* 37 (2006) 3737–3739. <https://doi.org/10.1007/s11661-006-1067-x>.
- [183] Y. Palizdar, A.J. Scott, R.C. Cochrane, R. Brydson, Understanding the effect of aluminium on microstructure in low level nitrogen steels, *Mater. Sci. Technol.* 25 (2009) 1243–1248. <https://doi.org/10.1179/174328409X401133>.
- [184] W.G. Johnston, J.J. Gilman, Dislocation velocities, dislocation densities, and plastic flow in lithium fluoride crystals, *J. Appl. Phys.* 30 (1959) 129–144. <https://doi.org/10.1063/1.1735121>.
- [185] N. Fonstein, H.J. Jun, G. Huang, S. Sriram, B. Yan, Effect of bainite on mechanical properties of multiphase ferrite-bainite-martensite steels, *Mater. Sci. Technol. Conf. Exhib. 2011, MS T'11. 1* (2011) 634–641.
- [186] J.H. Hollomon, *Tensile Deformation*, 1945.
- [187] M.R. Akbarpour, A. Ekrami, Effect of ferrite volume fraction on work hardening behavior of high bainite dual phase (DP) steels, *Mater. Sci. Eng. A.* 477 (2008) 306–310. <https://doi.org/10.1016/j.msea.2007.05.051>.
- [188] A. Zare, A. Ekrami, Effect of martensite volume fraction on work hardening behavior of triple phase (TP) steels, *Mater. Sci. Eng. A.* 528 (2011) 4422–4426. <https://doi.org/10.1016/j.msea.2011.02.021>.
- [189] D. Das, P.P. Chattopadhyay, Influence of martensite morphology on the work-hardening behavior of high strength ferrite–martensite dual-phase steel, *J. Mater. Sci.* 44 (2009) 2957–2965. <https://doi.org/10.1007/s10853-009-3392-0>.

- [190] P. Movahed, S. Kolahgar, S.P.H. Marashi, M. Pouranvari, N. Parvin, The effect of intercritical heat treatment temperature on the tensile properties and work hardening behavior of ferrite–martensite dual phase steel sheets, *Mater. Sci. Eng. A.* 518 (2009) 1–6. <https://doi.org/10.1016/j.msea.2009.05.046>.
- [191] D.H. Kang, D.-W. Kim, S. Kim, G.T. Bae, K.H. Kim, N.J. Kim, Relationship between stretch formability and work-hardening capacity of twin-roll cast Mg alloys at room temperature, *Scr. Mater.* 61 (2009) 768–771. <https://doi.org/10.1016/j.scriptamat.2009.06.026>.
- [192] R. Narayanasamy, R. Ponalagusamy, S. Raghuraman, The effect of strain rate sensitivity on theoretical prediction of limiting draw ratio for cylindrical cup drawing process, *Mater. Des.* 29 (2008) 884–890. <https://doi.org/10.1016/j.matdes.2006.05.014>.
- [193] C. Zhang, L. Leotoing, D. Guines, E. Ragneau, Theoretical and numerical study of strain rate influence on AA5083 formability, *J. Mater. Process. Technol.* 209 (2009) 3849–3858. <https://doi.org/10.1016/j.jmatprotec.2008.09.003>.
- [194] S. Yi, J. Bohlen, F. Heinemann, D. Letzig, Mechanical anisotropy and deep drawing behaviour of AZ31 and ZE10 magnesium alloy sheets, *Acta Mater.* 58 (2010) 592–605. <https://doi.org/10.1016/j.actamat.2009.09.038>.
- [195] P.K. Pradhan, P.S. Robi, S.K. Roy, Micro void coalescence of ductile fracture in mild steel during tensile straining, *Frat. Ed Integrità Strutt.* 6 (2011) 51–60. <https://doi.org/10.3221/IGF-ESIS.19.05>.
- [196] J.I. Yoon, H.H. Lee, J. Jung, H.S. Kim, Effect of grain size on stretch-flangeability of twinning-induced plasticity steels, *Mater. Sci. Eng. A.* 735 (2018) 295–301. <https://doi.org/10.1016/j.msea.2018.08.052>.
- [197] J.I. Yoon, J. Jung, H.H. Lee, J.Y. Kim, H.S. Kim, Relationships between stretch-flangeability and microstructure-mechanical properties in ultra-high-strength dual-phase steels, *Met. Mater. Int.* 25 (2019) 1161–1169. <https://doi.org/10.1007/s12540-019-00270-x>.
- [198] J. Chintamani, S. Sriram, Sheared edge characterization of steel products used for closure panel applications, *SAE Tech. Pap.* (2006). <https://doi.org/10.4271/2006-01-1589>.
- [199] R. Hambli, S. Richir, Damage mechanics approach in crack growth simulation during the fine blanking process, *Int. J. Mater. Prod. Technol.* 19 (2003) 466. <https://doi.org/10.1504/IJMPT.2003.003465>.
- [200] S.K. Paul, A critical review on hole expansion ratio, *Materialia.* 9 (2020) 100566. <https://doi.org/10.1016/j.mtla.2019.100566>.
- [201] H.M. Al-Jabr, Influence of crystallographic texture in X70 pipeline steels on toughness anisotropy and delamination, Colorado School of Mines, 2016.

